Towards well-balancing the regional hydrostatic climate model REMO

Dissertation with the aim of achieving a doctoral degree at the
Faculty of Mathematics, Informatics and Natural Sciences
Department of Earth Sciences of Universität Hamburg

submitted by Lennart Christopher Marien
2019 in Hamburg

Als Dissertation angenommen am Fachbereich Geowissenschaften	
Tag des Vollzugs der Promotion:	03.07.2020
Gutachter/Gutachterinnen:	Prof. Dr. Jörn Behrens
	Prof. Dr. Daniela Jacob
Vorsitzender des Fachpromotionsausschusses Geowissenschaften:	Prof. Dr. Dirk Gajewski
Dekan der Fakultät MIN:	Prof. Dr. Heinrich Graener

“Experience is the name we give to our mistakes.”

OSCAR WILDE
⋆1854 †1900

Abstract

The representation of complex orography in weather prediction and climate models has been an active field of research for several decades, yet many questions remain unanswered. The canonical method of formulating the equations of motion in terrain-following coordinate systems is known to produce large errors in the computation of the pressure gradient force due to unbalanced truncation errors particularly in the vicinity of steep orographic gradients. In the present work an approach to well-balance these truncation errors is developed. The resulting discretization of the pressure gradient force is based on the estimation of hydrostatic background states via the solution of suitable initial value problems for the hydrostatic equation. The proposed method is shown to be well-balanced for isothermal equilibrium states with arbitrarily complex (smooth) orography. The developments are implemented and tested with the regional hydrostatic climate model REMO in several idealized test cases.

Zusammenfassung

Die Darstellung von komplexer Orographie in Wettervorhersage- und Klimamodellen ist seit Jahrzehnten ein aktives Forschungsfeld, aber viele Fragen sind noch offen. Seit langem ist bekannt, dass die gängige Formulierung der primitiven Gleichungen in geländefolgenden Koordinatensystemen große Fehler in der Druckgradientkraft produziert. Ursächlich sind unbalancierte Abschneidefehler, die inbesondere in der Umgebung von starken orographischen Gradienten auftreten. In der vorliegenden Arbeit wird eine wohl-balancierte Diskretisierung der Druckgradientkraft entwickelt, die auf der Schätzung von hydrostatischen Hintergrundzuständen durch die Lösung geeigneter Anfangswertprobleme für die hydrostatische Gleichung beruht. Es wird gezeigt, dass die entwickelte Diskretisierung wohl-balancierte Ergebnisse für isotherme Gleichgewichtszustände mit beliebig komplexer aber glatter Orographie produziert. Die Entwicklungen werden in dem regionalen hydrostatischen Klimamodell REMO implementiert und in idealisierten Testfällen validiert.

Contents

List of Tables 1

List of Figures 3

List of Abbreviations and Acronyms 7

1 Introduction 9
- 1.1 Motivation . . . 9
- 1.2 Terrain-Following Coordinate Systems and the Pressure Gradient Error . 10
- 1.3 Aims and Structure of the Thesis . . . 15

2 The REMO Model 17
- 2.1 Overview . . . 17
  - 2.1.1 Physics . . . 17
  - 2.1.2 Dynamics . . . 18
- 2.2 Coordinate Systems . . . 19
  - 2.2.1 Horizontal Coordinate System . . . 19
  - 2.2.2 Vertical Coordinate System . . . 19
- 2.3 Continuous Model Equations . . . 22
  - 2.3.1 Prognostic Equations . . . 22
  - 2.3.2 Diagnostic Equations . . . 24
- 2.4 Discretization . . . 28
  - 2.4.1 Grid Structure and Discrete Operators . . . 28
  - 2.4.2 Prognostic Equations . . . 33
  - 2.4.3 Diagnostic Equations . . . 35
  - 2.4.4 Solution of the Discrete Equations . . . 38
  - 2.4.5 Semi-Implicit Correction . . . 38
  - 2.4.6 Asselin Filter . . . 39

3 The Pressure Gradient Error 41
- 3.1 The Pressure Gradient Force . . . 41
  - 3.1.1 The Cartesian System . . . 44
  - 3.1.2 The Hybrid η-System . . . 46
- 3.2 Well-Balanced Numerical Methods . . . 48
- 3.3 Stationary and Steady States . . . 50
- 3.4 A Novel Characterization of Equilibrium . . . 54

4 Well-Balancing Strategy 59
4.1 Introductory Example 59
4.2 Balancing in η-Coordinates 61
4.2.1 Reconstructing the Local Background State 65
4.2.2 Vertical and Horizontal Staggering 67
4.2.3 The Isothermal Equilibrium 70

5 Validation in Idealized Test Cases 73
5.1 The Isothermal Atmosphere 73
5.1.1 Computational Domain and Orography 73
5.1.2 Initial and Boundary Values 75
5.1.3 Results 76
5.2 The Standard Atmosphere 93
5.2.1 Results 93

6 Conclusions and Future Perspectives 109
6.1 Summary 109
6.2 Critical Discussion and Conclusions 110
6.3 Outlook 112

Appendices 115

Vertical Coordinate Parameters for Test Cases 117

References 121

Acknowledgement 129

Eidesstattliche Erklärung 131

List of Tables

3.1 Standard Atmosphere in REMO 52

A1 Vertical Coordinate Parameters for 27 Full Layers 118
A2 Vertical Coordinate Parameters for 40 Full Layers 119

List of Figures

1.1 *Illustration of a meteorological field expressed in Cartesian coordinates (left) and in a terrain-following coordinate (right).* . . . 11
1.2 *Illustration of orography (solid black) intersecting a regular grid. The resulting cut-cells are shown in red.* . . . 12

2.1 *Illustration of a domain before and after rotation.* . . . 20
2.2 *Illustration of discrete representations of a domain with different resolutions.* . . . 29
2.3 *Illustration of the Arakawa-C grid structure in REMO.* . . . 30
2.4 *Illustration of the Lorenz grid structure in physical space.* . . . 31

3.1 *Example of an atmosphere-at-rest with tracer bubble at time* $t = 0$ . . . 42
3.2 *Disturbances of atmosphere-at-rest at time* $t = 4h$ *in the REMO model.* . . . 43
3.3 *Illustration of the hydrostatic balance.* . . . 45
3.4 *Plot of pressure and temperature distribution for the standard atmosphere.* . . . 53
3.5 *Temperature (left) and Geopotential (right) in the* η*-system.* . . . 55

5.1 *Test case orography: bell shaped mountain (solid) and Schär-type mountain (dotted).* . . . 74
5.2 *Vertical level distributions for the isothermal test case with* 40 *levels and* 1 km *horizontal resolution.* . . . 76
5.3 u*-error at final time* $t = 3600\,\mathrm{s}$ *for the classic scheme and the bell-shaped mountain. Shown are the results for* 27 *and* 40 *levels (top to bottom) and* 10 km *as well as* 1 km *(left to right) respectively. Orography is shown in brown.* . . . 78
5.4 u*-error at final time* $t = 3600\,\mathrm{s}$ *for the PGFCONST scheme and the bell-shaped mountain. Shown are the results for* 27 *and* 40 *levels (top to bottom) and* 10 km *as well as* 1 km *(left to right) respectively. Orography is shown in brown.* . . . 79
5.5 u*-error at final time* $t = 3600\,\mathrm{s}$ *for the PGFLIN scheme and the bell-shaped mountain. Shown are the results for* 27 *and* 40 *levels (top to bottom) and* 10 km *as well as* 1 km *(left to right) respectively. Orography is shown in brown.* . . . 81
5.6 u*-error at final time* $t = 3600\,\mathrm{s}$ *for the Schär-type mountain. Shown are the results for* 27 *and* 40 *levels (left to right) and for the classic, the PGFCONST and PGFLIN schemes (top to bottom).* . . . 82
5.7 *Pressure gradient error at initial time* $t = 0\,\mathrm{s}$ *for the classic scheme and the bell-shaped mountain. Shown are the results for* 27 *and* 40 *levels (top to bottom) and* 10 km *as well as* 1 km *(left to right) respectively. Orography is shown in brown.* . . . 83

5.8 *Pressure gradient error at final time* $t = 3600\,\mathrm{s}$ *for the classic scheme and the bell-shaped mountain. Shown are the results for* 27 *and* 40 *levels (top to bottom) and* 10 km *as well as* 1 km *(left to right) respectively. Orography is shown in brown.* 84
5.9 *Pressure gradient error at initial time* $t = 0\,\mathrm{s}$ *for the PGFCONST scheme and the bell-shaped mountain. Shown are the results for* 27 *and* 40 *levels (top to bottom) and* 10 km *as well as* 1 km *(left to right) respectively. Orography is shown in brown.* 86
5.10 *Pressure gradient error at final time* $t = 3600\,\mathrm{s}$ *for the PGFCONST scheme and the bell-shaped mountain. Shown are the results for* 27 *and* 40 *levels (top to bottom) and* 10 km *as well as* 1 km *(left to right) respectively. Orography is shown in brown.* 87
5.11 *Maximum (top) and mean (bottom) absolute u-error for the isothermal case and the bell-shaped mountain. Values are shown for the classic scheme (solid) and the PGFCONST scheme (dashed). Colors indicate different resolutions.* 88
5.12 *Maximum (top) and mean (bottom) absolute u-error for the isothermal case and the Schär-type mountain. Values are shown for the classic scheme (solid) and the PGFCONST scheme (dashed). Colors indicate different resolutions.* 89
5.13 *Pressure gradient error for a single point centered above the bell-shaped mountain. Values are shown for the PGFCONST scheme (top) and the PGFCONST scheme with exact geopotential (bottom). Colors indicate different resolutions.* . 91
5.14 *Pressure gradient error for a single point centered above the Schär-type mountain. Values are shown for the PGFCONST scheme (top) and the PGFCONST scheme with exact geopotential (bottom). Colors indicate different resolutions.* . 92
5.15 *u-error at final time* $t = 3600\,\mathrm{s}$ *for the classic scheme and the bell-shaped mountain (standard atmosphere case). Shown are the results for* 27 *and* 40 *levels (top to bottom) and* 10 km *as well as* 1 km *(left to right) respectively. Orography is shown in brown.* 94
5.16 *u-error at final time* $t = 3600\,\mathrm{s}$ *for the PGFCONST scheme and the bell-shaped mountain (standard atmosphere case). Shown are the results for* 27 *and* 40 *levels (top to bottom) and* 10 km *as well as* 1 km *(left to right) respectively. Orography is shown in brown.* 96
5.17 *u-error at final time* $t = 3600\,\mathrm{s}$ *for the PGFLIN scheme and the bell-shaped mountain (standard atmosphere case). Shown are the results for* 27 *and* 40 *levels (top to bottom) and* 10 km *as well as* 1 km *(left to right) respectively. Orography is shown in brown.* 97
5.18 *u-error at final time* $t = 3600\,\mathrm{s}$ *for the Schär-type mountain (standard atmosphere case). Shown are the results for* 27 *and* 40 *levels (left to right) and for the classic, the PGFCONST and PGFLIN schemes (top to bottom).* 98
5.19 *Pressure gradient error at initial time* $t = 0\,\mathrm{s}$ *for the classic scheme and the bell-shaped mountain (standard atmosphere case). Shown are the results for* 27 *and* 40 *levels (top to bottom) and* 10 km *as well as* 1 km *(left to right) respectively. Orography is shown in brown.* 99

5.20 *Pressure gradient error at final time* $t = 3600\,\mathrm{s}$ *for the classic scheme and the bell-shaped mountain (standard atmosphere case). Shown are the results for* 27 *and* 40 *levels (top to bottom) and* 10 km *as well as* 1 km *(left to right) respectively. Orography is shown in brown.* 100
5.21 *Pressure gradient error at initial time* $t = 0\,\mathrm{s}$ *for the PGFCONST scheme and the bell-shaped mountain (standard atmosphere case). Shown are the results for* 27 *and* 40 *levels (top to bottom) and* 10 km *as well as* 1 km *(left to right) respectively. Orography is shown in brown.* 102
5.22 *Pressure gradient error at final time* $t = 3600\,\mathrm{s}$ *for the PGFCONST scheme and the bell-shaped mountain (standard atmosphere case). Shown are the results for* 27 *and* 40 *levels (top to bottom) and* 10 km *as well as* 1 km *(left to right) respectively. Orography is shown in brown.* 103
5.23 *Pressure gradient error at initial time* $t = 0\,\mathrm{s}$ *for the PGFLIN scheme and the bell-shaped mountain (standard atmosphere case). Shown are the results for* 27 *and* 40 *levels (top to bottom) and* 10 km *as well as* 1 km *(left to right) respectively. Orography is shown in brown.* 104
5.24 *Pressure gradient error at final time* $t = 3600\,\mathrm{s}$ *for the PGFLIN scheme and the bell-shaped mountain (standard atmosphere case). Shown are the results for* 27 *and* 40 *levels (top to bottom) and* 10 km *as well as* 1 km *(left to right) respectively. Orography is shown in brown.* 105
5.25 *Maximum (top) and mean (bottom) absolute u-error for the standard atmosphere case and the bell-shaped mountain. Values are shown for the classic scheme (solid) and the PGFCONST scheme (dashed). Colors indicate different resolutions.* 106
5.26 *Maximum (top) and mean (bottom) absolute u-error for the standard atmosphere case and the Schär-type mountain. Values are shown for the classic scheme (solid) and the PGFCONST scheme (dashed). Colors indicate different resolutions.* . . 107

List of Abbreviations and Acronyms

CFL	Courant-Friedrichs-Lewy
FD	finite difference
FDM	finite difference method
FE	finite element
FEM	finite element method
FV	finite volume
FVM	finite volume method
GCM	general circulation model
LHS	left hand side
LM	Lokalmodell
LTE	local truncation error
NWP	numerical weather prediction
PGE	pressure gradient error
PGF	pressure gradient force
RCM	regional climate model
REMO	Regional Model
RHS	right hand side
RMSE	root-mean-square error

SWE	shallow water equations
TFCS	terrain-following coordinate system
WBM	well-balanced method

1 Introduction

In this chapter a brief overview of available literature pertaining to the representation of orography in climate and numerical weather prediction (NWP) models in general and to the accurate computation of the pressure gradient force (PGF) in particular is given. Furthermore, an outline of the present thesis is presented and its guiding research questions are posed.

1.1 Motivation

In recent years, climate change due to anthropogenic influence has become a widely accepted fact in the scientific community and beyond (IPCC 2014). Consequently, numerous research efforts are being directed towards the estimation of the impacts of climate change on society and its people. This includes the development of strategies to mitigate future changes or to adapt to changes thought of as unavoidable.

All such endeavors heavily rely on projections of future climate change obtained from global general circulation models (GCMs). However, due to limitations on computing power GCMs can only provide data with relatively coarse spatial resolutions, currently ranging from about 4° to 0.5° in production environments (e.g., Taylor, Stouffer, and Meehl 2012). These resolutions are well suited to assess changes on the planetary or continental scale such as global mean temperature increases. However, such resolutions are not sufficient to resolve the strong spatial heterogeneity in climate change expected on the regional and local scale, e.g., in the analysis of metropolitan areas, municipalities, mountains, river deltas or small islands. Therefore, GCM results are often refined locally with regional climate models (RCMs). In this way, regions of interest can be resolved much more accurately (e.g., Jacob, Petersen, et al. 2014) while retaining consistency with the global changes at the boundaries of the computational domain.

Increasing the resolution is however not only a problem of available computational resources. Instead, RCMs have to be adapted to the local scales in order to produce sound physical information, e.g., by introducing scale dependent physical parameterizations. Another substantial challenge associated with high resolution RCMs is the representation of complex orography in the models. Steep gradients and naturally occurring discontinuities in terrain are more accurately resolved when resolution is increased. Albeit being a desired effect, this can also bring about some adverse consequences. The lack of smoothness in terrain data often proves difficult to handle for the numerical schemes of climate models potentially leading to a lack of computational stability. For this reason, many state-of-the-art models apply mollifying filters to the data at the expense of a more realistic representation of orographic structure. Another important example of detrimental effects related to terrain representation is connected to the widespread use of terrain-following coordinate systems (TFCSs). It is well known that such coordinate systems exhibit accuracy deficits in the computation of the pressure gradient force especially in the vicinity of steep terrain. With increased resolution steep gradients are more likely to be encountered exacerbating the issue.

These issues present substantial challenges in accurately capturing the local climatic features in regions such as the Alps, the Rocky Mountains or the Himalayas. The orographic structure has great influence on parameters such as wind speed, runoff and precipitation. At the same time, future changes in these regions are especially important to understand as they may have grave consequences for the livelihood and health of local residents in neighboring communities. For instance, the fresh water supply of several hundred millions of people depends on the rivers and the water cycle of the Himalayas (You et al. 2017). Another example is the dependency of many alpine communities on winter tourism threatened by changes in snowfall frequency and intensity (e.g., Elsasser and Bürki 2002; Beniston 2012).

1.2 Terrain-Following Coordinate Systems and the Pressure Gradient Error

As pointed out in the preceding section accurate resolution of orographic features and their influence on local climate is a difficult endeavor. The arising challenges range from constructing suitable parameterizations to adapting the numerical schemes used to solve the basic equations of motion. The present work will exclusively be concerned with the latter issue and more specifically with the pressure gradient error (PGE). This error is associated with the use of TFCSs, i.e., coordinate systems that map the irregular orographic features in physical space to a flat computational space.

The first example of such a coordinate was introduced by Phillips (1957) and due to its many advantages soon became the dominating technique to incorporate orography into circulation models of all kinds. The basic idea is to choose the ratio of pressure and surface pressure as a vertical coordinate rather than, e.g., geometrical height above mean sea level. Clearly, such a coordinate always has the value one at the ground where pressure and surface pressure conform. Likewise, at the top of the model atmosphere where the atmospheric pressure vanishes this coordinate always has the value zero. Consequently, the distance between ground and top of the atmosphere is always mapped to the regular unit interval irrespective of the local orographic features. Figure 1.1 shows an illustration of physical and computational space in a terrain-following coordinate. Today virtually all weather and climate models use or support at least one coordinate built upon the same principles.

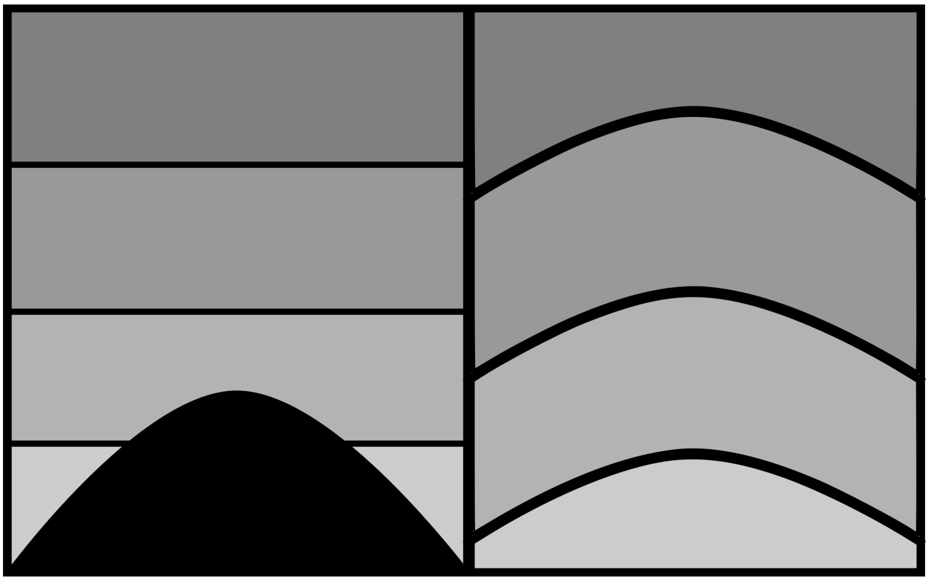

Figure 1.1: *Illustration of a meteorological field expressed in Cartesian coordinates (left) and in a terrain-following coordinate (right).*

To understand the widespread and even quasi-monopolistic use of these coordinates one must look at the technical challenges faced when introducing orography into models of the atmosphere. Generally speaking, such models are comprised of two parts often referred to as the physics package and the dynamical core. The latter term refers to the part of the model that solves the primitive equations of motion based on suitable initial (and in case of a regional model also boundary) conditions. The physics package of a model describes all processes that are not accounted for by the primitive equations such as turbulence, precipitation, radiation, soil processes, freezing and melting to name just a few. The physics routines (typically referred to as parameterizations) use the quantities computed in the dynamical core (often called prognostic variables) such as temperature, wind speed and pressure as their input. Based on these values the parameterization schemes both diagnose all additional variables of interest (e.g., precipitation rate or net shortwave radiation) and estimate changes to the prognostic variables due to the parameterized processes. These changes (tendencies in common parlance) are then passed back to the dynamical core to be incorporated into the prediction of the next time step. The influence of orography on the prognostic variables is in principle already described by the equations of motions. Therefore, the natural place for orography to be included into a model is the dynamical core. Parameterizations may take orography values into account for their own purposes (e.g., in runoff computations) but the effects of terrain features on, e.g., flow patterns, moisture transport and temperature are best left to the equations of motion. The most prevalent technique to solve these equations in dynamical cores is the finite difference method (FDM). In fact, when orography was first introduced into the models it was the only production-ready method available. The last two decades have seen the advent of dynamical cores based on more advanced techniques such as finite volume (FV) and finite element (FE) methods, but most models still depend on the canonical methods. The former methods often allow to incorporate orography by simply fitting an unstructured grid to the terrain, e.g., by using a tessellation of the domain with triangular cells. For all practical purposes, FDMs on the other hand are limited to the use of structured or even regular grids, i.e., grids constructed of congruent cuboids with regular connectivity between the cells. Figure 1.2 demonstrates the problem of covering a domain with orography by a regular grid. The orography tends to intersect the near surface cells, i.e., parts of those cells are located within the soil, mountains or water bodies. Consequently, the assumptions preceding the equations of motion no longer hold. The introduction of a TFCS offers a solution to this problem by transferring the equations to a computational space that can be covered by a regular grid. Additionally, the formulation of lower boundary conditions is greatly simplified in this situation. It suffices to require that no transport across the surface takes place. These features and the lack of alternatives at the time motivated the rapid dissemination of TFCSs among the NWP and climate research communities.

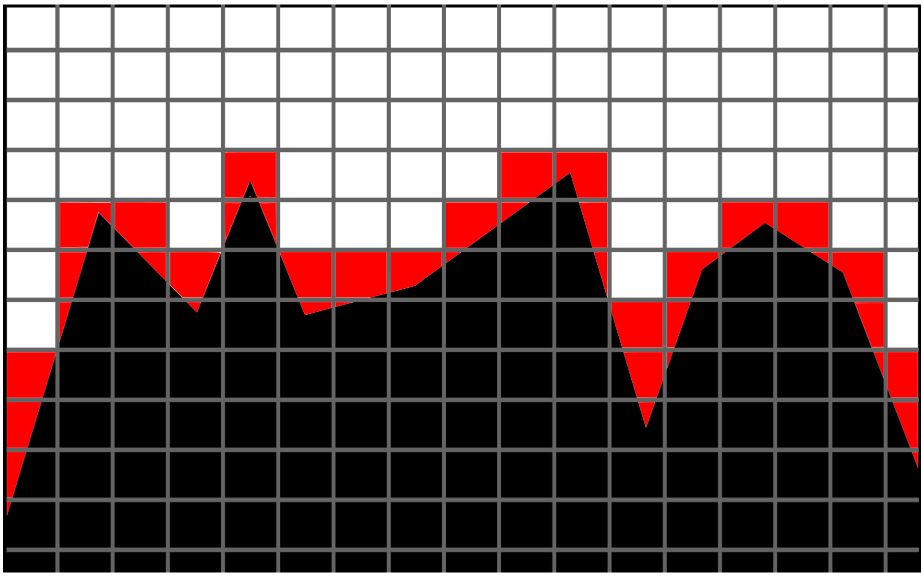

Figure 1.2: *Illustration of orography (solid black) intersecting a regular grid. The resulting cut-cells are shown in red.*

However elegant, this solution also comes at a price. Smagorinsky et al. (1967) reported large truncation errors in the computation of the PGF when using the σ-coordinate introduced by Phillips (1957). These errors were most prominent in regions characterized by strong orographic gradients and large enough to produce spurious eddies in the vicinity. The authors suggested to compute the PGF in the classical p-system to reduce the error, albeit being a remedy that requires interpolation back and forth between the two systems (see Kurihara 1968). Based on an investigation of idealized numerical examples Gary (1973) instead proposed to express the equations of motion in terms of the deviation from a hydrostatic background state. This approach proved rather successful and today is still considered a standard measure to reduce orography related truncation errors especially in the NWP community. For climate applications the latter method is less appealing as suitable background states may change over the long integration times and cannot simply be inferred from initial conditions (Botta et al. 2004). Sundqvist (1975) and Sundqvist (1976) elaborated on the nature and cause of the observed truncation errors. In the σ-system the horizontal PGF is expressed as the sum of two terms opposite in sign but similar in magnitude, i.e.,

$$\mathbf{F}^{\sigma}_{\nabla p} = \nabla\Phi + RT\nabla \ln p_s \tag{1.1}$$

with $\mathbf{F}^{\sigma}_{\nabla p}$ the PGF, p and p_s the (surface) pressure, Φ the geopotential, R the gas constant of dry air and T the absolute temperature. This form of the PGF is a consequence of having to compute derivatives along the curved coordinate lines in the computational space (see Figure 1.1). The PGF is in general much smaller than either of the two components on the right hand side (RHS) of equation (1.1). Small errors in these components can therefore produce disproportionally large errors in the resultant PGF. For instance, Sundqvist (1975) reported that an error of 1 % in the temperature term can result in PGF errors of up to 20 %. In this way, truncation errors that are relatively small compared to the magnitude of the approximated quantities can introduce large errors into the PGF resulting in spurious or distorted motion. This becomes especially evident in situations in which (1.1) equates to zero, i.e., in states of hydrostatic equilibrium. Both NWP and climate models with terrain-following coordinates often fail to retain such states. Instead, the erroneously generated momentum provokes unphysical horizontal and vertical flow. It should be stressed that mathematically speaking equation (1.1) always equates to zero in a state of equilibrium. It is only when (1.1) is discretised, i.e., converted into a form suitable for processing on computer systems that truncation errors are introduced into the system. Hence, the PGE is not a modeling error but a numerical one and needs to be addressed as such.

Since the introduction of the original σ-coordinate many research efforts have aimed to construct alternative terrain-following coordinates. Kasahara (1974) introduced a terrain-following coordinate based on geometric height rather than pressure. Gal-Chen and Somerville (1975a) and Gal-Chen and Somerville (1975b) followed a similar approach with emphasis on the non-hydrostatic equation set. In that context pressure is non-monotonic and therefore not suitable to build coordinate transformations. It was not until two decades later that Laprise (1992) and Janjić, Gerrity, and Ničković (2001) enabled the use of pressure based TFCSs in a non-hydrostatic context by splitting the pressure variable into a hydrostatic and a non-hydrostatic component. Sangster (1960) suggested a hybrid coordinate that behaves like a σ-coordinate near the ground but becomes isobaric above a fixed pressure threshold. Arakawa and Lamb (1977) refined this concept for use in the University of California GCM. Simmons and Burridge (1981) also presented a hybrid coordinate with emphasis on a smooth transition between the terrain-following and isobaric regimes. Zhu et al. (1992) presented a hybrid coordinate transitioning from σ-levels to isentropic levels in the upper atmosphere. Schär et al. (2002) conceived a coordinate with adaptive decay for small-scale and typically under-resolved orographic features improving on the smoothness of higher-altitude levels and thereby reducing numerical noise. However, all of these coordinates still result in representations of the PGF similar to (1.1) and can suffer from significant truncation errors.

Song (1998) identified four major directions of research in the literature with the goal of reducing the PGE in both atmosphere and ocean models. Namely, the interpolation of data to the z- or p-system (e.g., Smagorinsky et al. 1967; Fortunato and Baptista 1996), the subtraction of hydrostatic reference states (e.g., Gary 1973), the use of higher-order schemes to improve accuracy (e.g., McCalpin 1994; Beckmann and Haidvogel 1993) and the development of schemes that retain discrete analogues of integral properties (e.g., Arakawa and Suarez 1983; Arakawa and Konor 1996; Lin 1997).

Problems with retaining equilibrium states due to truncation errors similar to those exhibited by discrete renditions of (1.1) have also been subject to research outside of the climate and NWP community. More specifically, a number of mathematical publications are concerned with finding systematic approaches to balancing the truncation errors of two or more terms in systems of differential equations such that equilibrium states are exactly retained. Such methods are often referred to as well-balanced methods (WBMs) in the literature (e.g., Greenberg and Leroux 1996; LeVeque 1998). Many WBMs also address geophysical models with terrain such as the shallow water equations (SWE) (e.g., Audusse et al. 2004) with applications in diverse areas such as tsunami and inundation modeling (e.g., Vater, Beisiegel, and Behrens 2015), arterial blood flow (Müller, Parés, and Toro 2013; Delestre and Lagrée 2013) or sediment transport (Qian et al. 2015). As of now, comparatively few publications investigated whether numerical schemes developed under the umbrella of well-balancing could be applied to atmospheric models such as RCMs. To some extent this can likely be explained by the fact that most publications on WBMs focus on finite volume methods (FVMs). While these methods have gained popularity in atmospheric models in recent years most models still work with low-order FDMs. Of the existing well-balancing literature on FDMs most is geared towards higher-order schemes with non-oscillatory and total-variation-diminishing properties specifically engineered to accurately resolve shocks in hyperbolic systems (e.g., Xing and Shu 2006; Wang et al. 2009). Still, Botta et al. (2004) and Klein, Bates, and Nikiforakis (2009) demonstrated that the application of well-balancing to models of the atmosphere may be promising.

Moreover, part of the research has been geared towards alternative representations of terrain in atmospheric models. The two most notable examples are the cut-cell and the step-mountain approach. The former one uses the Cartesian coordinate system and thereby avoids most of the problems associated with (1.1). However, the intersection of a regular grid by orography (see Figure 1.2) produces degenerate cells that need specialized numerical treatment (e.g., Bonaventura 2000; Steppeler, Bitzer, Minotte, et al. 2002; Klein, Bates, and Nikiforakis 2009; Good et al. 2014; Shaw and Weller 2016; Yamazaki, Satomura, and Nikiforakis 2016). Such cells typically have small size with negative impact on performance due to the Courant-Friedrichs-Lewy (CFL) criterion. Additionally, the application of physically consistent lower boundary conditions becomes rather complex and usually requires the use of uncentered differences. On the other hand, the step-mountain approach removes complete cells from the computational grid to approximate the given terrain. This avoids most of the complications with cut-cells at the cost of a less accurate representation of orography (see Mesinger et al. 1988). However, Gallus and Klemp (2000) reported difficulties to produce physically correct solutions of flow over a steep hill with this method.

While the difficulties in calculating the PGF have been long acknowledged its detrimental influence on real-data predictions is difficult to assess. On the one hand, outside of strongly simplified test cases no analytical solutions to the equations of motions are known which makes production of suitable reference solutions a difficult endeavor. Moreover, physical parameterizations likely are even more critical to the accuracy of predictions and so the attribution of observed errors to the PGF would be challenging. Still, there is some indication that the PGE has substantial negative effects on the quality of predictions. Steppeler, Bitzer, Janjić, et al. (2006) pointed out that artificial mountain-generated forcing can negatively impact cloud structure in the vicinity. They also reported structural improvements in precipitation forecast and threat scores as well as root-mean-square error (RMSE) of temperature and wind vectors when using a cut-cell version of the German Weather Service Lokalmodell (LM).

1.3 Aims and Structure of the Thesis

Representing orography in circulation models is both a long-standing and current research problem as evidenced by the vast body of classic and recent literature on the topic. As mentioned relatively little work has been dedicated to apply the concept of well-balancing to models of the atmosphere. Most notably Botta et al. (2004) presented a framework to effectively balance truncation errors in the context of FVMs for non-hydrostatic models. Such methods canonically utilize the Cartesian frame of reference and represent orography by unstructured grids. While the authors indicate that their method can readily be applied to FDMs as well it remains unclear whether this also holds when a TFCS is used or a hydrostatic model is concerned. The present work aims at filling this research gap by attempting to answer the following research questions:

- *Can existing well-balancing approaches be transferred to hydrostatic FDM climate models?*
- *Is this effective and efficient in reducing the pressure gradient error encountered in the presence of steep and complex orography?*
- *How does this relate to the different types of TFCSs employed, e.g., pressure-based vs. height-based systems?*

The thesis is structured as follows: In chapter two the regional hydrostatic climate model REMO which will be used as a test bed to develop and apply a well-balancing strategy is introduced. In chapter three the pressure gradient error is defined, the basic ideas of well-balancing and the standard discretisation of the PGF are introduced and the equilibrium states of the model are investigated. In the fourth chapter an alternative discretisation of the PGF that can be readily applied within the REMO framework is developed. In chapter five the newly developed method is applied to several idealized test-cases to assess strengths and weaknesses of the discretisation. Finally, in chapter six a summary of the present work is given, the results are critically discussed and an outlook of possible further research is given.

2 The REMO Model

Throughout this study new methodical developments will be implemented and validated with the regional hydrostatic climate model REMO Regional Model (REMO). In this chapter a brief overview of the REMO model in general and its dynamical core in particular is given.

2.1 Overview

REMO (Jacob 2001; Jacob, Van den Hurk, et al. 2001) is a three-dimensional hydrostatic primitive equation regional climate model originally based on the German Weather Service “Europa-Modell” (Majewski 1991). To allow application to climate projections the physics package of the Max Planck Institute for Meteorology global climate model ECHAM4 (Roeckner et al. 1996) was implemented into REMO and has since been continuously developed and expanded. More recently the model has also been updated with a non-hydrostatic extension (Göttel 2009).

2.1.1 Physics

The present work will exclusively deal with the dynamical component of the model, i.e., the solution of the primitive equations in Euler-form and more specifically the computation of the pressure gradient force. Giving even a cursory overview of the numerous physical parameterizations in REMO, i.e., those parts of the model that describe diabatic processes such as, e.g., freezing and melting, microphysical interactions, radiative transfer and other components of the climate not covered by the primitive equations, is hence beyond the scope of this work. Instead some of the main parameterization schemes are listed and appropriate references are pointed out for detailed descriptions. The main characteristics of the physical parameterizations are given by a radiation scheme based on Morcrette, Smith, and Fouquart (1986) and Giorgetta and Wild (1995). The treatment of stratiform clouds is governed by schemes based on Sundqvist (1978) with modifications based on Roeckner et al. (1996), where also a lot of in-depth information on several other parameterizations in REMO can be found. Cumulus convection is represented through a mass flux scheme after Tiedtke (1989) and Nordeng (1994). The turbulent surface fluxes are computed according to Monin-Obukhov similarity theory (Louis 1979) with vertical diffusion based on the turbulent kinetic energy. Soil processes are modeled with a 5-layer diffusion scheme for heat transfer and a bucket approach for soil moisture, interception by vegetation and snow with modifications that allow the freezing and thawing of soil water (Semmler 2002). The runoff scheme is based on Dümenil and Todini (1992).

2.1.2 Dynamics

The most important aspects of REMO's dynamical core will be covered in the following sections in some detail, but here the main features as relevant for the developments in later chapters are summarized. The basic model formulation is based on the hydrostatic primitive equation system (e.g., White et al. 2005)), i.e., a rendition of the Euler-equations of motion under the assumption of a hydrostatically balanced atmosphere. In such cases the third equation of motion reduces to a diagnostic relationship for the geopotential height, significantly reducing computational costs in the process, but also limiting the model to coarser resolutions beyond about ten kilometers.

The basic equations are discretized using a centered finite-difference approach on a regular longitude-latitude grid in the horizontal and a hybrid terrain-following grid in the vertical. For the time discretization the leapfrog scheme is employed, necessitating the use of a filter to maintain stability of the computation. In REMO the Asselin-filter is used for this purpose. While centered differences in general would allow for second order approximations, in practice the use of the Asselin-filter limits the order of approximation somewhat below this mark (see e.g., Duran 2010).

Stability requirements also motivate the addition of diffusion terms to the equations in order to prevent the accumulation of numerical noise at the shortest wavelengths resolved by the model. To lessen the constraints given by the CFL number (e.g., Duran 2010), some of the model also features implicit formulations. On the one hand the vertical advection is handled by the classical Crank-Nicolson scheme. On the other hand processes prone to generating gravity waves are dealt with applying the scheme of Simmons and Burridge (1981) but can also be approached explicitly instead, depending on model configuration. Implicit formulations enable the use of larger timesteps, generally outweighing the drawbacks of having to solve additional equations in each of them.

Furthermore, since REMO is a regional model boundary conditions need to be provided in addition to an initial state, generally created from global model output or reanalysis products. To smoothly impose the boundary values on the solution a lateral relaxation scheme after Davies (1976) is applied.

2.2 Coordinate Systems

In this section the coordinate systems used in REMO are described as a prerequisite to formulating the equations of motions later on.

2.2.1 Horizontal Coordinate System

REMO employs a spherical coordinate system in the horizontal directions. It is derived by intricate rotation of the standard geographical coordinate system. The rotation is constructed such that the rotated equator passes through the center of the domain. Near the poles meridional convergence can result in very small computational cells, effectively dominating the choice of timestep for the whole domain due to the CFL-condition (e.g., Duran 2010). Because REMO is a regional model the rotation in general guarantees that the rotated domain is far away from the poles, as illustrated by Figure 2.1. Consequently, the influence of meridional convergence on the choice of viable timesteps is strongly limited. A detailed account of the coordinate transformation, its inverse and the conversion of wind components between the rotated and the geographical system can be found in the literature (Majewski and Schrodin 1995). Note however that the resulting equation systems – before and after transformation – are exactly the same with only one exception: the Coriolis factor $f = 2\Omega \sin\varphi$. In the rotated system one instead has:

$$f = 2\Omega \left(\sin\varphi \sin\varphi^N + \cos\varphi \cos\varphi^N \cos\left(\lambda - \lambda^N\right) \right) \tag{2.1}$$

where (λ, φ) are the rotated longitude and latitude respectively and $\left(\lambda^N, \varphi^N\right)$ are the coordinates of the geographical north pole in the rotated system.

2.2.2 Vertical Coordinate System

In the vertical direction the REMO model uses a terrain-following coordinate system. The classical example of such a coordinate for meteorological use is the σ-coordinate developed by Phillips (1957). The idea is to express the model height not in terms of, e.g., geometric or geopotential height, or in terms of the atmospheric pressure but as the ratio of hydrostatic pressure to hydrostatic surface pressure:

$$\sigma = \frac{p}{p_s} \tag{2.2}$$

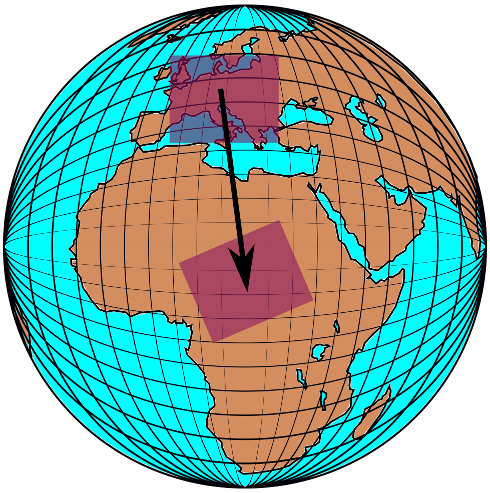

Figure 2.1: *Illustration of a domain before and after rotation.*

Clearly at surface level one has $p = p_s$ and hence $\sigma = 1$. The lowest coordinate surface in the σ-system coincides with the bottom topography. On the other hand at the top of the atmosphere one has $p = 0$ and hence also $\sigma = 0$. Since the coordinate is built from the hydrostatic pressure – which of course is a monotone function of height – the result is also a monotone function, allowing its use as a vertical coordinate in the equations of motion. The main advantage is that the lower vertical boundary condition simplifies substantially, avoiding the use of, e.g., uncentred differences in the presence of sloping topography.

There are however also a number of tradeoffs: meteorological observations often are given on surfaces of constant pressure. Such data has to be interpolated to σ-surfaces to be used as driving data in terrain-following models (e.g., Sundqvist 1976). Additionally while the sloping of coordinate surfaces is useful at the lower boundary, it serves no purpose in the upper atmosphere. Here typical flow regimes tend to follow isobaric surfaces that would be most naturally expressed in a pressure coordinate. Consequently, the representation along σ-surfaces is often numerically more difficult and can produce noise around steeply sloped coordinate surfaces even in the upper atmosphere.

Moreover, the representation of the horizontal pressure gradient force is also more complicated in this and related coordinates (e.g., Sundqvist 1978). To reduce these disadvantages REMO instead uses a hybrid coordinate after Simmons and Burridge (1981), which will be referred to as the η-coordinate during this work. The idea is to use a pressure coordinate in a large part of the upper atmosphere thereby facilitating a natural representation of the flow. At the lower boundary a σ-system is used instead to retain the advantages of terrain following coordinates in regards to the lower boundary condition. Between the two regimes the coordinate is linearly interpolated to allow a suitable transition.

This can be written

$$\eta = \begin{cases} \frac{p}{p_r} & \text{for } 0 \leq p \leq p_t \\ \frac{p-p_t}{p_s-p_t} + \frac{p_t}{p_r} \cdot \frac{p_s-p}{p_s-p_t} & \text{for } p_t \leq p \leq p_s \end{cases} \tag{2.3}$$

with p_r a constant reference pressure and p_t a pressure threshold above which η is identical to a pressure coordinate. In REMO $p_r = 1013.25\,\text{hPa}$ is used for the reference pressure. The pressure threshold varies between simulations but is generally chosen roughly around 220 hPa. From (2.3) it can be readily seen that one has $\eta = 1$ for $p = p_s$, i.e., the lowest coordinate surface exactly follows the given orography. As will be seen later this is enough to ensure the benefits of a simplified lower boundary condition. At $p = p_t$ the two terms in (2.3) are exactly identical and the transition between the terrain-following and the pressure regime is continuous. Clearly, the influence of orographic variation on the coordinate surfaces is decaying linearly towards the threshold p_t. For any pressure $p \leq p_t$ the coordinate surfaces are indeed completely independent of the given surface elevation. In this way detrimental numerical effects of the sloping η-surfaces as discussed above are effectively limited. Furthermore, the pressure surfaces in the upper atmosphere are well suited to describe flow in the free atmosphere. Figure 2.4 illustrates these typical features of the coordinate surfaces in the η-system.

According to (2.3) η is a function of p and p_s, but likewise one can express p as a function of η and p_s. With the definitions

$$A(\eta) = \begin{cases} p_r\eta & \text{for } 0 \leq \eta \leq \eta_t \\ \frac{p_r p_t}{p_r-p_t}\,(1-\eta) & \text{for } \eta_t \leq \eta \leq 1 \end{cases} \tag{2.4}$$

$$B(\eta) = \begin{cases} 0 & \text{for } 0 \leq \eta \leq \eta_t \\ \frac{p_r\eta-p_t}{p_r-p_t} & \text{for } \eta_t \leq \eta \leq 1 \end{cases} \tag{2.5}$$

where η_t is the η-value corresponding to the pressure threshold p_t, i.e., $\eta_t = \frac{p_t}{p_r}$, we can write:

$$p = A(\eta) + B(\eta) \cdot p_s \tag{2.6}$$

This means that in the η-system the atmospheric pressure takes the form of a linear function. As will be seen later equation (2.6) can be used as a diagnostic equation to recover the pressure from the given atmospheric parameters $A(\eta), B(\eta)$ and the hydrostatic surface pressure p_s.

2.3 Continuous Model Equations

In this section the basic continuous equations of motion, used to advance the meteorological variables of interest in time, are given. This exposition closely follows Majewski and Schrodin (1995) where more in-depth information about the dynamical core can be found.

2.3.1 Prognostic Equations

Here the main equations for each of the prognostic variables are formulated: hydrostatic surface pressure, horizontal wind components, temperature as well as specific humidity, cloud water and cloud ice.

Equation of Continuity

Technically the equation of continuity is not used as a prognostic equation for the REMO model, but the equations for the surface pressure and the vertical velocity in the η-system both are derived from it. For completeness it is hence given here as

$$\frac{\partial}{\partial t}\left(\frac{\partial p}{\partial \eta}\right) + \frac{1}{a\cos\varphi}\left[\frac{\partial}{\partial \lambda}\left(u\frac{\partial p}{\partial \eta}\right) + \frac{\partial}{\partial \varphi}\left(v\cos\varphi\frac{\partial p}{\partial \eta}\right)\right] + \frac{\partial}{\partial \eta}\left(\dot{\eta}\frac{\partial p}{\partial \eta}\right) = 0 \tag{2.7}$$

where p is the hydrostatic pressure, $a = 6\,371\,229\,\mathrm{m}$ the radius of earth, φ and λ the rotated latitude and longitude respectively, u, v the zonal and meridional wind components, and $\dot{\eta} = \frac{D\eta}{Dt}$ the vertical velocity in the η-system. As pointed out earlier one of the main advantages of a terrain-following coordinate system is the simple formulation of vertical and in particular the lower boundary condition. Assuming that no mass transport happens through the upper or lower boundary, i.e., the interfaces to outer space and inner earth, the boundary conditions can simply be given as:

$$\begin{aligned} \dot{\eta} &= 0 \text{ at the upper boundary with } \eta = 0 \\ \dot{\eta} &= 0 \text{ at the lower boundary with } \eta = 1 \end{aligned} \tag{2.8}$$

Surface Pressure

Integrating (2.7) from top to bottom of the atmosphere and employing the vertical boundary conditions (2.8) yields a prognostic equation for the hydrostatic surface pressure p_s. The rate of change of p_s is then given by:

$$\frac{\partial p_s}{\partial t} + \frac{1}{a\cos\varphi}\int_0^1 \frac{\partial}{\partial\lambda}\left(u\frac{\partial p}{\partial\eta}\right) + \frac{\partial}{\partial\varphi}\left(v\cos\varphi\frac{\partial p}{\partial\eta}\right)\,\mathrm{d}\eta' = 0 \tag{2.9}$$

Wind Components

The evolution of the wind component in zonal direction u is described by the following equation:

$$\frac{\partial u}{\partial t} - \frac{1}{\cos\varphi}Q\frac{\partial p}{\partial\eta}v\cos\varphi + \frac{1}{a\cos\varphi}\frac{\partial}{\partial\lambda}(\Phi + K) + \frac{RT_v}{a\cos\varphi}\frac{\partial\ln p}{\partial\lambda} + \dot{\eta}\frac{\partial u}{\partial\eta} - D_u = F_u \tag{2.10}$$

Here Q denotes the absolute potential vorticity, p the hydrostatic pressure, Φ the geopotential, T_v the virtual temperature, $R = 287.05\,\mathrm{J/(kg\,K)}$ the gas constant for an ideal gas, $\dot{\eta}$ the vertical velocity and D_u the horizontal diffusion of u. Likewise for the the wind component in meridional direction v one has

$$\frac{\partial v}{\partial t} - Q\frac{\partial p}{\partial\eta}u + \frac{1}{a}\frac{\partial}{\partial\varphi}(\Phi + K) + \frac{RT_v}{a}\frac{\partial\ln p}{\partial\varphi} + \dot{\eta}\frac{\partial v}{\partial\eta} - D_v = F_v \tag{2.11}$$

where D_v is the horizontal diffusion of v. The terms F_u and F_v represent diabatic and subscale, i.e., parameterized processes such as convection or turbulent boundary layer interactions. Since physical parameterizations are not the topic of this work and for reasons of brevity the reader is referred to the various sources cited in subsection 2.1.1 for detailed treatments. This also applies to related terms appearing in the remaining equations.

Temperature

The thermodynamic equation is given by

$$\frac{\partial T}{\partial t} + \frac{1}{a\cos\varphi}\left(u\frac{\partial T}{\partial\lambda} + v\cos\varphi\frac{\partial T}{\partial\varphi}\right) + \dot{\eta}\frac{\partial T}{\partial\eta} - D_T = \frac{\alpha\omega}{c_p} + F_T \tag{2.12}$$

where T is the absolute temperature, α the specific volume, $\omega = \frac{dp}{dt}$ the vertical velocity in terms of the hydrostatic pressure p, D_T the horizontal diffusion of temperature and F_T changes in temperature due to subscale processes.

Specific Humidity, Cloud Water and Cloud Ice

The moist components of air are realized as passive tracers

$$\frac{\partial q_d}{\partial t} + \frac{1}{a\cos\varphi}\left(u\frac{\partial q_d}{\partial \lambda} + v\cos\varphi\frac{\partial q_d}{\partial \varphi}\right) + \dot{\eta}\frac{\partial q_d}{\partial \eta} - D_{q_d} = F_{q_d} \tag{2.13}$$

$$\frac{\partial q_w}{\partial t} + \frac{1}{a\cos\varphi}\left(u\frac{\partial q_w}{\partial \lambda} + v\cos\varphi\frac{\partial q_w}{\partial \varphi}\right) + \dot{\eta}\frac{\partial q_w}{\partial \eta} - D_{q_w} = F_{q_w} \tag{2.14}$$

$$\frac{\partial q_i}{\partial t} + \frac{1}{a\cos\varphi}\left(u\frac{\partial q_i}{\partial \lambda} + v\cos\varphi\frac{\partial q_i}{\partial \varphi}\right) + \dot{\eta}\frac{\partial q_i}{\partial \eta} - D_{q_i} = F_{q_i} \tag{2.15}$$

with specific humidity q_d, cloud water q_w and cloud ice q_i and their horizontal diffusion terms $D_{q_d}, D_{q_w}, D_{q_i}$ respectively. Feedback mechanisms are included by using the virtual temperature T_v in (2.10) and (2.11) instead of the absolute temperature T. As before F_{q_d}, F_{q_w} and F_{q_i} represent subscale interactions including for example phase conversions.

2.3.2 Diagnostic Equations

Equations (2.9) to (2.15) constitute a closed system that can in principle be solved for the prognostic variables p_s, u, v, T, q_d, q_w and q_i. First however, the auxiliary quantities – such as for instance the geopotential Φ or the absolute potential vorticity Q – appearing in these equations have to be expressed in terms of the prognostic variables. Therefore, in this section the definitions of these diagnostic quantities will be introduced.

Pressure

Equation (2.9) references the pressure p at arbitrary levels. In hybrid pressure based coordinates the pressure at a given level is a linear function of the surface pressure p_s and the vertical coordinate η. With the definitions of subsection 2.2.2 one can write:

$$p = A(\eta) + B(\eta) \cdot p_s \tag{2.16}$$

Potential Absolute Vorticity

The potential absolute vorticity Q is needed to evaluate the momentum equations (2.10) and (2.11). It is given by

$$Q = \left(\frac{\partial p}{\partial \eta}\right)^{-1} \left(f + \frac{1}{a\cos\varphi}\left(\frac{\partial v}{\partial \lambda} - \frac{\partial u \cos\varphi}{\partial \varphi}\right)\right) \tag{2.17}$$

where f is the Coriolis force. According to (2.1) this term can be written

$$f = 2\Omega\left(\sin\varphi \sin\varphi^N + \cos\varphi\cos\varphi^N \cos\left(\lambda - \lambda^N\right)\right)$$

with

$$\Omega = 7.292\,11 \times 10^{-5}\,\mathrm{s}^{-1}$$

the angular velocity.

Geopotential

In a hydrostatic model such as REMO the geopotential is characterized by the balance of a gravity and a buoyancy term. Essentially this balance is the residual of the third equation of motion under hydrostatic conditions and given by

$$-RT_v \frac{\partial \ln p}{\partial \eta} = \frac{\partial \Phi}{\partial \eta} \tag{2.18}$$

and consequently the geopotential can be recovered by vertical integration from the bottom of the atmosphere to a given height η:

$$\Phi = \Phi_s - R\int_1^{\eta} T_v \frac{\partial \ln p}{\partial \eta}\ \mathrm{d}\eta' \tag{2.19}$$

The term $\Phi_s = g \cdot z_s$ denotes the surface geopotential with the height above mean sea level z_s.

Kinetic Energy

Term K in the momentum equations (2.10) and (2.11) represents the kinetic energy per unit mass. It is given by

$$K = \frac{1}{2}\left(u^2 + v^2\right) \tag{2.20}$$

Virtual Temperature

The virtual temperature T_v can be expressed as a function of the absolute temperature T and the moist components of air q_d, q_w and q_i as

$$T_v = T\left(1 + \left(\frac{R_D}{R} - 1\right) q_d - (q_w + q_i)\right) \tag{2.21}$$

where $R_d = 461.51\,\mathrm{J/(kg\,K)}$ is the gas constant for water vapor.

Vertical Velocity in the η-System

A diagnostic equation for the vertical velocity $\dot{\eta}$, i.e., the change of the vertical coordinate η following an air parcel along its trajectory, can be derived from (2.7). Integrating from top of the atmosphere to a given height η yields

$$\overset{\star}{\eta} = -\left(\frac{\partial p}{\partial p_s}\right)\frac{\partial p_s}{\partial t} - \frac{1}{a\cos\varphi}\int_0^{\eta}\frac{\partial}{\partial\lambda}\left(u\frac{\partial p}{\partial\eta}\right) + \frac{\partial}{\partial\varphi}\left(v\cos\varphi\frac{\partial p}{\partial\eta}\right)\,\mathrm{d}\eta' \tag{2.22}$$

with the auxiliary quantity $\overset{\star}{\eta} = \dot{\eta}\frac{\partial p}{\partial\eta}$.

Specific Volume

The specific volume α can be derived from the equation of state which can be written as:

$$\alpha = \frac{RT_v}{p} \tag{2.23}$$

Note that for a dry atmosphere (2.23) simply reduces to the ideal gas equation.

Vertical Velocity in the p-System

The $\frac{\alpha\omega}{c_p}$ term appearing in the thermodynamic equation (2.12) is related to the conversion of potential and kinetic energy. A diagnostic expression for ω can be found by direct differentiation of $\omega = \frac{Dp}{Dt}$ and substituting equation (2.22). This yields:

$$\begin{aligned} \frac{\omega}{p} = -\frac{1}{p}\left[\frac{1}{a\cos\varphi}\int_0^{\eta}\frac{\partial}{\partial\lambda}\left(u\frac{\partial p}{\partial\eta}\right)+\frac{\partial}{\partial\varphi}\left(v\cos\varphi\frac{\partial p}{\partial\eta}\right)\mathrm{d}\eta'\right]+ \\ \frac{1}{a\cos\varphi}\left(u\frac{\partial\ln p}{\partial\lambda}+v\cos\varphi\frac{\partial\ln p}{\partial\varphi}\right) \end{aligned} \tag{2.24}$$

Initial- and Boundary Conditions

With the definitions of this section equations (2.9)–(2.15) constitute a closed system that can in principle be solved for the prognostic variables $p_s, u, v, T, q_i, q_d, q_w$. This depends of course on the provision of suitable initial and boundary conditions. For the initial conditions the values of the prognostic variables are prescribed at the initial time and for the whole computational domain. In practice simulations of historical climate or reanalysis data are used to acquire appropriate initial values. For the vertical boundary an appropriate condition has already been established with (2.8). In case of a global model no further boundary conditions would be required. REMO however is a regional model and therefore also requires suitable conditions at the lateral boundaries of the domain. Again such values can be acquired from driving model simulations, both global and regional ones, or reanalysis data.

However – unlike for the vertical boundary – there is no obvious way to impose the resulting values for the prognostic variables near the lateral boundary. In REMO this is resolved by gradually relaxing the prognostic variables towards a specified reference state at the boundary according to Davies (1976). For any prognostic variable ψ with given reference state ψ_R at the lateral boundary, an additional relaxation term of the form $\mu_R(\psi - \psi_R)$ results on the right hand side of the respective prognostic equation (2.9)–(2.15). The relaxation factor μ_R is chosen in such a way that one has $\mu_R = 1$ at the lateral boundary and a rapid but smooth decay towards zero outside of the boundary.

Consequently, in practice μ_R is essentially zero everywhere but in a boundary zone of generally less than a dozen grid cells. In this way the driving values are imposed only at the boundary. At the same time the boundary zone allows for a smooth transition between the inner domain characterized by regional dynamics and the lateral boundary dominated by the forcing patterns. This strategy is effective but also likely to cause numerical noise near the lateral boundaries. In practice simulation results within the boundary zone are therefore treated cautiously and often excluded from analysis for increased robustness.

2.4 Discretization

In the last section the continuous equations of motions in the hybrid terrain-following η-coordinate were given and appropriate initial and boundary conditions were specified. Mathematically this should ensure the existence and uniqueness of a solution for which the given equation system (2.9)–(2.15) can then be solved. However, in general complex partial differential equations can not be solved explicitly, i.e., in closed form (e.g., Duran 2010). Instead solutions to such systems are typically approximated numerically, e.g., on high performance computing systems owing to the complexity of the task. Any computer can by its very nature only represent a finite number of distinct states, e.g., due to finite memory and a number of other limitations. On the other hand the system (2.9)–(2.15) – formulated in a mathematical continuum – can assume an infinite number of states.

In other words: computer systems are in general unable to solve such systems directly. Instead the equations first have to be rendered into a discrete form, i.e., one that requires only a finite number of unknowns to represent the state of the system across the domain of interest. Naturally, this representation will – except for very simple states – be only an approximation to the true solution of the underlying equation system. The more discrete points are used to represent the system, the better this approximation will be, as illustrated in Figure 2.2. Each gridbox shown is represented in the discrete model by a single value for each of the prognostic variables. With more gridboxes per area local structures including topographic features can be resolved much better. In the following equations (2.9)–(2.15) will be cast into a discrete form that facilitates the approximation of solutions on computer systems.

2.4.1 Grid Structure and Discrete Operators

First, an overview of the discrete structure employed in the REMO model is given. As mentioned before the idea is to approximate a mathematical continuum by a finite number of data points distributed within the region of interest.

Horizontal Grid

Horizontally REMO employs the so called Arakawa-C grid (see Arakawa and Lamb 1977). The main feature of this grid is that not all prognostic variables are distributed

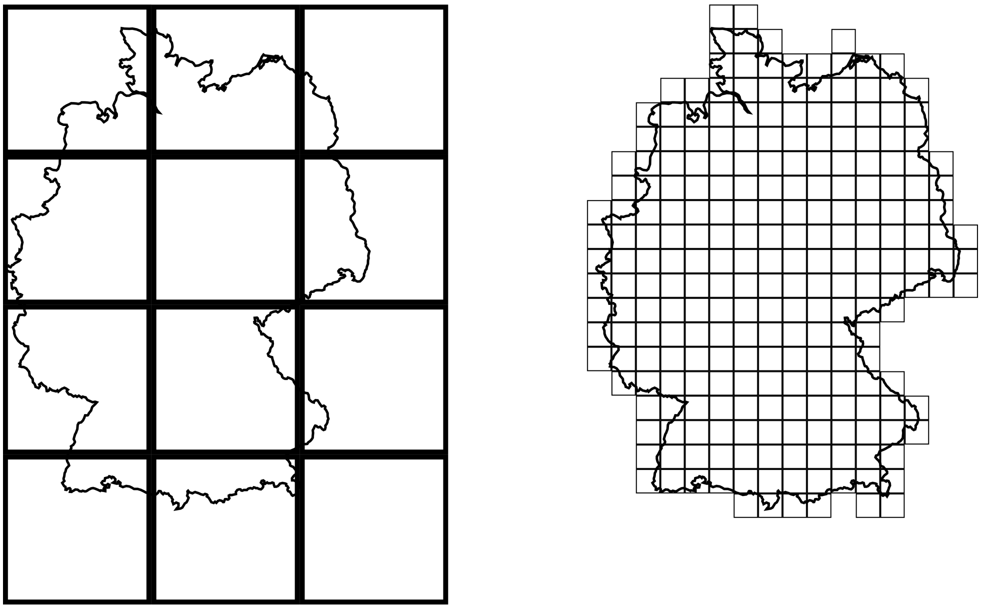

Figure 2.2: *Illustration of discrete representations of a domain with different resolutions.*

along the same discrete points, i.e., the grid is staggered. The main discretization points are labeled with full indices (i, j) as seen in Figure 2.3. At these points (shown as diamond nodes), often referred to as mass points, all the prognostic variables except for the horizontal wind components are located. The mass points are placed equidistantly within the rotated coordinate system with increments of $\Delta\lambda$ and $\Delta\varphi$, where in REMO generally $\Delta\lambda = \Delta\varphi$. If one thinks of mass points as the centers of computational cells (dashed lines in Figure 2.3) the horizontal wind components u and v are placed at the interfaces of those cells. That is, the u-component is displaced to the right by $\frac{\Delta\lambda}{2}$ and the v-component upwards by $\frac{\Delta\varphi}{2}$. Consequently, u-points labeled with indices $(i + \frac{1}{2}, j)$ and $(i, j + \frac{1}{2})$ for v-points respectively. The vorticity ζ is displaced in both horizontal directions and labeled $(i + \frac{1}{2}, j + \frac{1}{2})$. Note that despite being equidistantly chosen within the computational space (i.e., the rotated longitude-latitude system) in physical space (i.e., the geographical system) the effective horizontal resolution differs between the cells. This is most notably seen towards the poles due to meridional convergence.

Vertical Grid

Vertically the model is discretized with the so called Lorenz grid. Again the main feature of this grid is the staggering of its variables as illustrated in Figure 2.4. The solid lines are referred to as full layers and here all prognostic variables are located except for the (surface) pressure. That (as well as the diagnostic quantities Φ and $\dot{\eta}$) is instead located

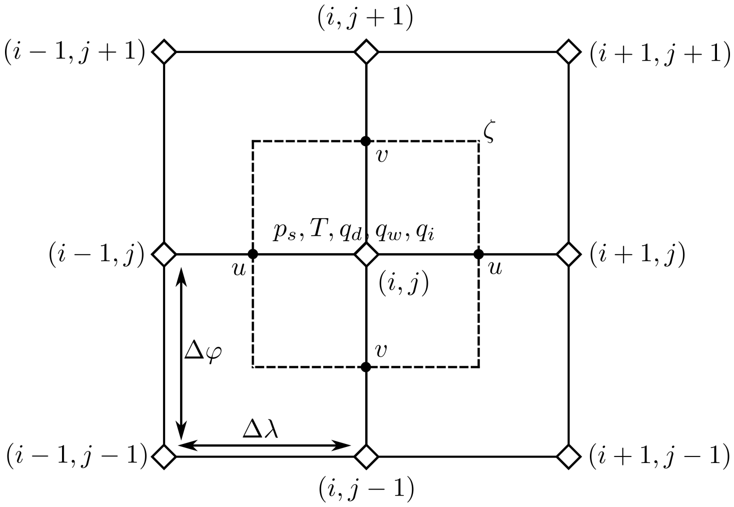

Figure 2.3: *Illustration of the Arakawa-C grid structure in REMO.*

on half layers (dashed lines in Figure 2.4), halfway between the full layers.

This construction is somewhat similar to the horizontal placement of variables, but note one of the main differences. In the horizontal arrangement the discretization points are distributed equidistantly at least within the rotated coordinate system. In the vertical grid this is generally not the case. Instead the vertical resolution in the η-system can differ substantially between different computational cells. Essentially the η-points at which the variables are to be evaluated are chosen freely and do not change over the course of a simulation. Note however that again a distinction between the computational space and the physical space has to be made. Unlike the horizontal resolution which in physical space varies between cells but is constant in time, the vertical resolution in physical space generally changes in every timestep depending on the value of the surface pressure.

The initial resolution (i.e., based on a reference pressure) in practice is chosen such that the planetary boundary layer is well-resolved. With increasing height the resolution becomes much coarser. For instance the lowest layer in standard setups often is only about 30 m thick, where the highest layers can reach thicknesses of 3 km and more. For the labeling of grid indices in the vertical k is used for full and $k+\frac{1}{2}$ for half layers. For instance a discrete temperature value on the grid is written T_{ijk}. Note however that in most cases one or several of the indices can be inferred from context. Therefore the same value will often be denoted as T_{ij} or T_k instead to improve the readability of formulas.

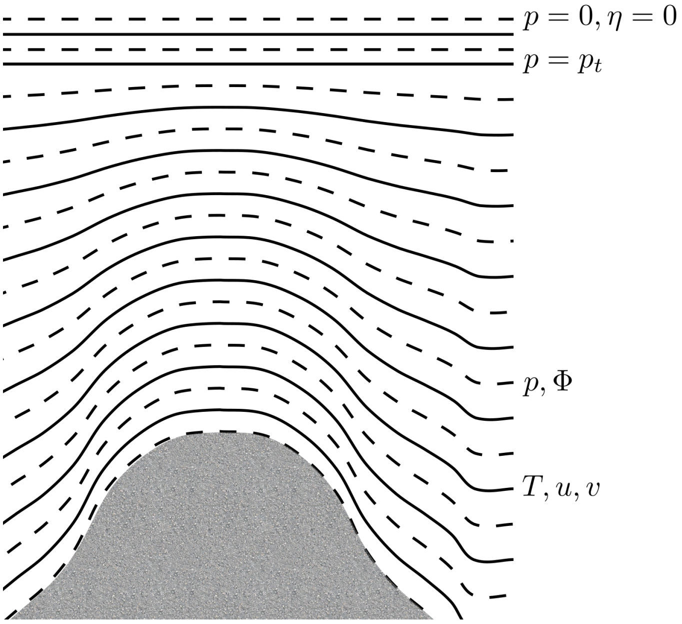

Figure 2.4: *Illustration of the Lorenz grid structure in physical space.*

Finite Difference and Averaging Operators

To construct a closed discrete equation system that allows computing the prognostic variables at the discretization points, the continuous equations have to be rendered into a discrete form. The main difficulty here is the approximation of the horizontal and vertical derivatives. In REMO finite-difference approximations, more specifically so called centered-differences, are used to achieve this. The main advantage of centered-differences is that they in principle allow for second order approximations of the derivatives, i.e., with increasing resolution $\Delta\lambda, \Delta\varphi$ the discretization error will tend to zero quadratically. At the same time, centered-differences are comparatively easy to implement in contrast to approximations that allow even higher orders of approximation. As discussed above the staggered nature of the computational grid facilitates the use of centered differences, making them the natural choice for REMO.

However, the use of staggered grids also requires in some places the transfer of quantities at mass points to u- or v-points and vice versa. The same applies to the vertical grid points. To achieve this a simple averaging approach is used which also retains the order of approximation.

The difference operators are defined as follows:

$$\begin{aligned}
\delta_\lambda \psi &= \frac{\psi_{i+1j} - \psi_{ij}}{\Delta\lambda} \\
\delta_\varphi \psi &= \frac{\psi_{ij+1} - \psi_{ij}}{\Delta\varphi}
\end{aligned} \tag{2.25}$$

where ψ is any quantity located at mass-points, such as virtual temperature T_v or surface pressure p_s. Note that according to equation (2.25) the discrete differences of such quantities in λ-direction are defined at u-points, and the ones in φ-direction at v-points respectively. At these points the operators in (2.25) constitute second-order accurate centered-differences. For quantities located on u- or v-points one likewise defines

$$\begin{aligned}
\delta_\lambda \psi &= \frac{\psi_{i+\frac{1}{2}j} - \psi_{i-\frac{1}{2}j}}{\Delta\lambda} \\
\delta_\varphi \psi &= \frac{\psi_{ij+\frac{1}{2}} - \psi_{ij-\frac{1}{2}}}{\Delta\varphi}
\end{aligned} \tag{2.26}$$

and note that the operators (2.26) are defined at mass-points, i.e., at grid cells labeled with full indices (i, j).

It is in some cases required to evaluate quantities naturally situated at $u-$ or $v-$points at mass points and vice versa. The following average operators allow for a simple but effective conversion:

$$\begin{aligned}
\overline{\psi}^\lambda &= \frac{\psi_{i+1j} + \psi_{ij}}{2} \\
\overline{\psi}^\varphi &= \frac{\psi_{ij+1} + \psi_{ij}}{2}
\end{aligned} \tag{2.27}$$

Analogously, for those quantities located on u- or v-points one instead has:

$$\begin{aligned}
\overline{\psi}^\lambda &= \frac{\psi_{i+\frac{1}{2}j} + \psi_{i-\frac{1}{2}j}}{2} \\
\overline{\psi}^\varphi &= \frac{\psi_{ij+\frac{1}{2}} + \psi_{ij-\frac{1}{2}}}{2}
\end{aligned} \tag{2.28}$$

Vertically one has to convert quantities located on half-layers to full-layers occasionally and this is again achieved by means of vertical averaging:

$$\overline{\psi}^\eta = \frac{\psi_{k+\frac{1}{2}} + \psi_{k-\frac{1}{2}}}{2} \tag{2.29}$$

Note that generally indices are omitted wherever they can be inferred from context. For instance, in (2.29) all references to the horizontal indices i and j are omitted as they are not relevant for the vertical averaging.

Leapfrog Time Integration

With the previously defined horizontal and vertical difference operators the spatial derivatives can be approximated. However, time derivatives also need to be approximated by suitable finite-differences. In REMO the leapfrog scheme is used for this purpose. Each prognostic equation can be written in the general form

$$\frac{\partial \psi}{\partial t} + A^d(\psi)\psi + A^n(\psi)\psi = 0 \tag{2.30}$$

where A^d represents all adiabatic terms and A^n all the other terms (i.e., from parameterizations). Then the leapfrog scheme can be given as

$$\frac{\psi^{t+\Delta t} - \psi^{t-\Delta t}}{2\Delta t} = -\left(A^d(\psi^t)\psi^t + A^n(\psi^{t-\Delta t})\psi^{t-\Delta t}\right) \tag{2.31}$$

where $\Delta t > 0$ is a predefined time increment. Note how in equation (2.31) the adiabatic and nonadiabatic terms are evaluated at different timesteps.

2.4.2 Prognostic Equations

With these prerequisites at hand the discrete prognostic equations can be given. The general procedure is straightforward: occurrences of prognostic variables are replaced by their discrete values at the respective grid points. Likewise, derivatives of these variables are discretized according to the operator definitions given in the preceding section. Wherever necessary average operators are used to ensure consistency between all terms in the equation. All quantities in one equation must either be located at mass points or at cell interfaces in the horizontal and on either full or half-layers in the vertical.

Surface Pressure

Approximating the integral in (2.9) with the midpoint rule one has for the surface pressure at mass points

$$\left(\frac{p_s^{t+\Delta t} - p_s^{t-\Delta t}}{2\Delta t}\right)_{ij} = -\frac{1}{a\cos\varphi_j}\sum_{l=1}^{k_m}\left[\delta_\lambda U_l + \delta_\varphi\left(V_l\cos\varphi\right)\right] \tag{2.32}$$

where k_m is the number of vertical levels. Note that in REMO $k = 1$ denotes the highest level and $k = k_m$ the lowest one above the ground.

Wind Components

Equation (2.10) yields

$$\begin{aligned}&\left(\frac{u_k^{t+\Delta t} - u_k^{t-\Delta t}}{2\Delta t}\right)_{i+\frac{1}{2}j} - \frac{1}{\cos\varphi_j}\overline{Q_k}^{\varphi}\overline{V_k \cos\varphi}^{\lambda,\varphi} + \frac{1}{a\cos\varphi_j}\delta_\lambda\left(\Phi_k + K_k\right)\\ &+ \frac{R\overline{T_{vk}}^{\lambda}}{a\cos\varphi_j}\delta_\lambda \ln p_k + \frac{1}{\overline{\Delta p_k}^{\lambda}}\overline{\overline{\overset{\star}{\eta}}^{\lambda}\ \Delta_\eta \overline{u_k}^{2t}}^{\eta} = D_{uk} + F_{uk}\end{aligned} \tag{2.33}$$

for the horizontal wind component at u-points. Likewise equation (2.11) at v-points results in:

$$\begin{aligned}&\left(\frac{v^{t+\Delta t} - v^{t-\Delta t}}{2\Delta t}\right)_{ij+\frac{1}{2}} + \overline{Q_k}^{\lambda}\overline{U_k}^{\lambda,\varphi} + \frac{1}{a}\delta_\varphi\left(\Phi_k + K_k\right)\\ &+ \frac{R\overline{T_{vk}}^{\varphi}}{a}\delta_\varphi \ln p_k + \frac{1}{\overline{\Delta p_k}^{\varphi}}\overline{\overline{\overset{\star}{\eta}}^{\varphi}\ \Delta_\eta \overline{v_k}^{2t}}^{\eta} = D_{vk} + F_{vk}\end{aligned} \tag{2.34}$$

Temperature

The discrete version of the thermodynamic equation (2.12) takes the form:

$$\begin{aligned}&\left(\frac{T_k^{t+\Delta t} - T_k^{t-\Delta t}}{2\Delta t}\right)_{ij} + \frac{1}{a\cos\varphi_j \Delta p_k}\left(\overline{U_k \delta_\lambda T_k}^{\lambda} + \overline{V_k \cos\varphi \delta_\varphi T_k}^{\varphi}\right)\\ &+ \frac{1}{\Delta p_k}\overline{\overset{\star}{\eta}\Delta_\eta \overline{T_k}^{2t}}^{\eta} = \alpha_k \omega_k + D_{Tk} + F_{Tk}\end{aligned} \tag{2.35}$$

Specific Humidity, Cloud Water and Cloud Ice

The structural similarity of equations (2.13)–(2.15) naturally carries over into these discrete representations:

$$\begin{aligned}&\left(\frac{q_{dk}^{t+\Delta t}-q_{dk}^{t-\Delta t}}{2\Delta t}\right)_{ij}+\frac{1}{a\cos\varphi_j\Delta p_k}\left(\overline{U_k\delta_\lambda q_{dk}}^{\lambda}+\overline{V_k\cos\varphi\delta_\varphi q_{dk}}^{\varphi}\right)\\&+\frac{1}{\Delta p_k}\overline{\overset{\star}{\eta}\Delta_\eta\overline{q_{dk}}^{2t}}^{\eta}=D_{q_dk}+F_{q_dk}\end{aligned}\tag{2.36}$$

$$\begin{aligned}&\left(\frac{q_{wk}^{t+\Delta t}-q_{wk}^{t-\Delta t}}{2\Delta t}\right)_{ij}+\frac{1}{a\cos\varphi_j\Delta p_k}\left(\overline{U_k\delta_\lambda q_{wk}}^{\lambda}+\overline{V_k\cos\varphi\delta_\varphi q_{wk}}^{\varphi}\right)\\&+\frac{1}{\Delta p_k}\overline{\overset{\star}{\eta}\Delta_\eta\overline{q_{wk}}^{2t}}^{\eta}=D_{q_wk}+F_{q_wk}\end{aligned}\tag{2.37}$$

$$\begin{aligned}&\left(\frac{q_{ik}^{t+\Delta t}-q_{ik}^{t-\Delta t}}{2\Delta t}\right)_{ij}+\frac{1}{a\cos\varphi_j\Delta p_k}\left(\overline{U_k\delta_\lambda q_{ik}}^{\lambda}+\overline{V_k\cos\varphi\delta_\varphi q_{ik}}^{\varphi}\right)\\&+\frac{1}{\Delta p_k}\overline{\overset{\star}{\eta}\Delta_\eta\overline{q_{ik}}^{2t}}^{\eta}=D_{q_ik}+F_{q_ik}\end{aligned}\tag{2.38}$$

2.4.3 Diagnostic Equations

Equations (2.32)–(2.38) constitute the discrete equation system that will be solved in each timestep. The required discrete forms of the auxiliary and diagnostic quantities will be given in the following.

Pressure

Equation (2.6) yields the discrete pressure on half layers:

$$p_{k+\frac{1}{2}}=A_{k+\frac{1}{2}}+B_{k+\frac{1}{2}}\cdot p_s\tag{2.39}$$

The discrete renditions of A and B here can simply be derived by evaluating equations (2.4) and (2.5) at the given discrete η-levels. These can as mentioned be arbitrarily chosen before the start of a simulation and remain constant afterwards. Often pressure values on full layers will be required instead:

$$p_k = \frac{p_{k+\frac{1}{2}} + p_{k-\frac{1}{2}}}{2} \tag{2.40}$$

Potential Absolute Vorticity

Equation (2.17) yields the discrete form

$$Q_k = \frac{1}{\overline{\Delta p_k a \cos\varphi}^{\lambda,\varphi}} \left[\overline{f}^{\lambda\varphi} a \overline{\cos\varphi}^{\lambda} + \delta_\lambda v_k - \delta_\varphi \left(u_k \cos\varphi \right) \right] \tag{2.41}$$

where discrete values of f can be evaluated with equation (2.1).

Geopotential

Applying once more the midpoint rule to the integral in equation (2.19) gives for the geopotential on half layers:

$$\Phi_{k+\frac{1}{2}} = \Phi_s + R \sum_{l=k+1}^{k_m} T_{vl} \ln \frac{p_{l+\frac{1}{2}}}{p_{l-\frac{1}{2}}} \tag{2.42}$$

From here full layer geopotentials are computed by averaging:

$$\Phi_k = \frac{\Phi_{k+\frac{1}{2}} + \Phi_{k-\frac{1}{2}}}{2} \tag{2.43}$$

Kinetic Energy

The discrete kinetic energy simply amounts to:

$$K_k = \frac{1}{2} \left(\overline{u_k^2}^{\lambda} + \frac{1}{\cos\varphi_j} \overline{v_k^2 \cos\varphi}^{\varphi} \right) \tag{2.44}$$

Virtual Temperature

For the discrete virtual temperature the discrete values of temperature and moisture variables simply have to be substituted into equation (2.21):

$$T_{vk} = T_k \left(1 + \left(\frac{R_D}{R} - 1\right) q_{dk} - (q_{wk} + q_{ik})\right) \tag{2.45}$$

Vertical Velocity in the η-System

Equation (2.22) reads in discrete form:

$$\begin{aligned} \overset{\star}{\eta}_{ijk+\frac{1}{2}} &= b_{k+\frac{1}{2}} \frac{1}{a \cos\varphi_j} \sum_{l=1}^{k_m} \left[\delta_\lambda U_l + \delta_\varphi \left(V_l \cos\varphi\right)\right] \\ &- \frac{1}{a \cos\varphi_j} \sum_{l=1}^{k} \left[\delta_\lambda U_l + \delta_\varphi \left(V_l \cos\varphi\right)\right] \end{aligned} \tag{2.46}$$

Vertical Advection

The vertical advection terms are discretized as follows

$$\begin{aligned} \left(\dot{\eta}\frac{\partial u}{\partial \eta}\right)_{i+\frac{1}{2}jk} &= \frac{1}{\overline{\Delta p_k}^{\lambda}} \overline{\overline{\overset{\star}{\eta}}^{\lambda}\ \Delta_\eta \overline{u_k}^{2t}}^{\eta} \qquad\qquad (2.47) \\ &= \frac{1}{2\overline{\Delta p_k}^{\lambda}} \left[\overline{\overset{\star}{\eta}_{k+\frac{1}{2}}}^{\lambda} \left(\overline{u_{k+1}}^{2t} - \overline{u_k}^{2t}\right) + \overline{\overset{\star}{\eta}_{k-\frac{1}{2}}}^{\lambda} \left(\overline{u_k}^{2t} - \overline{u_{k-1}}^{2t}\right)\right] \\ \left(\dot{\eta}\frac{\partial v}{\partial \eta}\right)_{ij+\frac{1}{2}k} &= \frac{1}{\overline{\Delta p_k}^{\varphi}} \overline{\overline{\overset{\star}{\eta}}^{\varphi}\ \Delta_\eta \overline{v_k}^{2t}}^{\eta} \qquad\qquad (2.48) \\ &= \frac{1}{2\overline{\Delta p_k}^{\varphi}} \left[\overline{\overset{\star}{\eta}_{k+\frac{1}{2}}}^{\varphi} \left(\overline{v_{k+1}}^{2t} - \overline{v_k}^{2t}\right) + \overline{\overset{\star}{\eta}_{k-\frac{1}{2}}}^{\varphi} \left(\overline{v_k}^{2t} - \overline{v_{k-1}}^{2t}\right)\right] \end{aligned}$$

where $\psi^{2t} = \frac{\psi^{t+\Delta t} - \psi^{t-\Delta t}}{2}$. This approach is often referred to as the Crank-Nicolson scheme. The important point is the presence of unknowns at time level $t + \Delta t$ in the three different levels $k-1, k$ and $k+1$. This means that equations (2.47) and (2.48) constitute an implicit approach. As will be seen later this requires the solution of a linear equation system in every timestep.

2.4.4 Solution of the Discrete Equations

In the preceding sections the continuous equations (2.9)–(2.15) were rendered into the discrete form (2.32)–(2.38) to facilitate the approximation of solutions on computer systems. In this section it will be detailed how the resulting equation system can be solved for the discrete values of the prognostic variables. With some reordering all the discrete prognostic equations – with exception of the surface pressure that does not contain implicit components – can be written in the general form

$$A_k(\psi_{k-1}^{t+\Delta t}) + B_k(\psi_k^{t+\Delta t}) + C_k(\psi_{k+1}^{t+\Delta t}) = D_k \tag{2.49}$$

where ψ is the prognostic variable of interest. For reasons of brevity the exact form of the coefficients A_k, B_k, C_k and D_k is not given here and the reader is instead referred to the literature and specifically Majewski and Schrodin (1995). Iterated over all levels $k = 1, \ldots, k_m$ equation (2.49) then yields a tridiagonal system that can be solved with standard methods. In REMO the system is solved using the well-known Thomas algorithm. Note that D_k also contains values of the prognostic variable, albeit only those at previous timesteps $t - \Delta t$ and t.

2.4.5 Semi-Implicit Correction

The previously presented scheme is – with the exception of vertical advection – purely explicit. In practice however the model is almost always run with additional implicit components. Since in REMO these components can be switched on and off the term semi-implicit correction is often used. First, the (mostly) explicit forecast is computed according to the preceeding section. Then terms that are known to cause gravity waves are corrected for by averaging the linear components of those terms in time.

The main advantage of the semi-implicit approach is the ability to use larger timesteps that would otherwise be prohibitive as a consequence of the CFL-criterion (e.g., Duran 2010). The CFL-criterion essentially ensures that waves do not travel across more than one gridbox per timestep. On the flipside the semi-implicit scheme requires more computational effort, as the updated values of the prognostic equations must first be derived from an appropriate equation system. For REMO this results in a Helmholtz equation, that is quite difficult to solve. Nevertheless the much larger timestep that can be used with the semi-implicit correction generally outweighs this disadvantage. This work will mostly be concerned with the explicit parts of the model and hence a detailed description of the semi-implicit correction is beyond the scope. Instead the reader is referred to the literature and specifically to Simmons and Burridge 1981 for an in-depth treatment.

2.4.6 Asselin Filter

To complete a prediction step the Asselin filter has to be applied to the intermediate results. This is required to ensure the stability of the leapfrog time integration scheme. With the definitions of equation (2.30) the Asselin filter takes the form

$$\psi^{t+\Delta t} = \overline{\psi}^{t-\Delta t} - 2\Delta t A^d(\psi^t)\psi^t - 2\Delta t A^n(\psi^{t-\Delta t})\overline{\psi}^{t-\Delta t} \tag{2.50}$$

where $\overline{\psi}$ denotes the filtered values.

This completes the introduction into the REMO dynamical core. In the next chapter the notations and definitions given here will serve as the basis for taking a closer look at the pressure gradient force in REMO and the particular problems arising from its computation.

3 The Pressure Gradient Error

In this chapter a thorough problem description to outline the difficulties associated with the computation of the pressure gradient force in terrain-following models is given. To this end, the pressure gradient error is defined, examples of its detrimental influence on model simulations are given and some of the ideas that have been applied to tackle the problem in the literature are briefly reviewed. The aim of this work is to gauge the applicability of numerical schemes developed under the umbrella of WBMs to the REMO dynamical core. The concept of well-balanced discretizations is therefore introduced and an approach suitable to address the problem in REMO is identified.

3.1 The Pressure Gradient Force

For quite some time it has been well established that numerical models of the atmosphere often fail to retain states of rest. Such conditions are characterized by horizontally homogeneous thermodynamic variables in hydrostatic balance and the absence of external forcing. From a physical point of view such states are maintained indefinitely. However, for instance Sundqvist (1975) reported erroneous winds in a global model that was initialized with such an atmosphere-at-rest. These errors, often referred to as the pressure gradient error (PGE), were most pronounced in mountainous areas and around steep slopes with spurious velocities of up to several meters per second. This suggested a connection to the representation of complex orography in the terrain-following σ-coordinate system employed.

The same study also identified inconsistent truncation errors in the computation of the pressure gradient force (PGF) as the root cause of this issue. In terrain-following models derivatives of meteorological quantities have to be computed along the sloped coordinate surfaces (cf. Figure 2.4). For the PGF this results in two terms that both have to be approximated by finite-differences. Such approximations are always afflicted with a truncation error due to the finite resolution of computational models. However, in general the truncation errors of these approximations will not cancel in a state of rest. This results in the observed generation of spurious momentum in the model atmosphere. This effect is not limited to the σ-system but occurs in all common terrain-following coordinates, such as the Gal-Chen-Somerville (Gal-Chen and Somerville 1975a; Gal-

Chen and Somerville 1975b) or the hybrid η-coordinates (Simmons and Burridge 1981) used in REMO.

To illustrate the issue Figure 3.1 shows an example of an atmosphere-at-rest in the REMO model at time $t = 0$. The model is initialized with a horizontally homogeneous and hydrostatic state. Centered in the domain is a parabola-shaped hill of 2.5 km height. A circular tracer bubble is placed above the hill representing, e.g., the concentration of a chemical or moisture species whose transport is modeled. From a physical point of view the tracer should keep its shape indefinitely because the atmosphere is in equilibrium. Figure Figure 3.2 shows the disturbances resulting from erroneous pressure gradient computations at $t = 4\,\mathrm{h}$. The tracer has visibly deformed due to the induced horizontal momentum which in turn triggers vertical transport as well. The shape of the underlying hill has to some extent been imprinted onto the tracer bubble due to the terrain-following model layers.

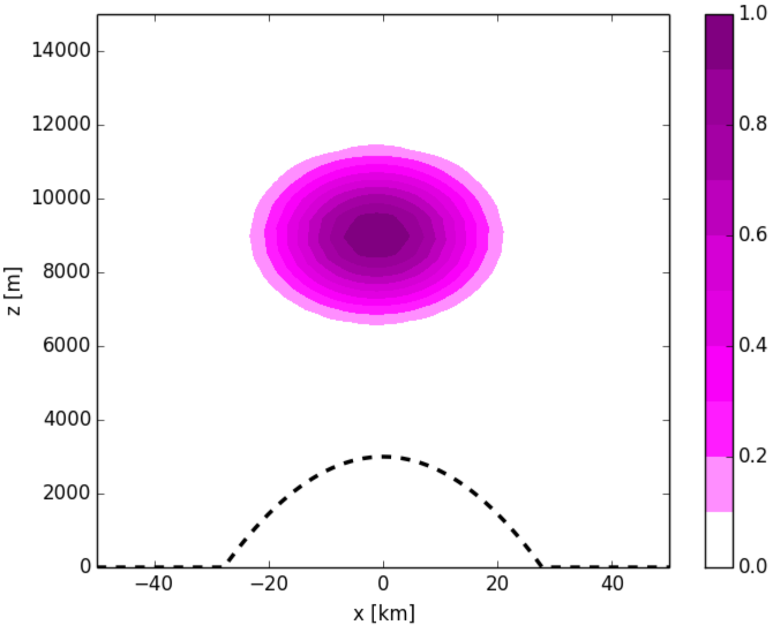

Figure 3.1: *Example of an atmosphere-at-rest with tracer bubble at time* $t = 0$

Numerous studies have since proposed strategies to more accurately compute the pressure gradient force in terrain-following coordinates both in atmosphere and ocean models. Due to the strong bathymetric variations the latter ones often suffer even more from the PGE. Probably the most widespread approach is to subtract global mean stationary states from the prognostic variables before computing the PGF (e.g., Gary 1973). Other

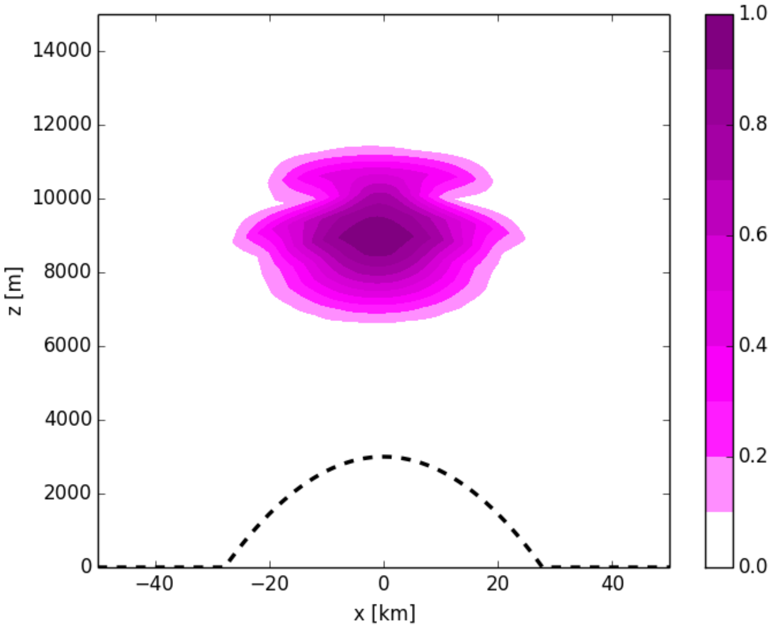

Figure 3.2: *Disturbances of atmosphere-at-rest at time $t = 4h$ in the REMO model.*

authors have opted to compute the PGF in the p-system to avoid errors resulting from the terrain-following coordinate (Smagorinsky et al. 1967).

Sometimes the terrain-following system is abandoned in favor of a vertical z-coordinate. In such cases the lower boundary conditions become much more intricate leading to the cut-cell approach (e.g., Steppeler, Bitzer, Minotte, et al. 2002; Yamazaki, Satomura, and Nikiforakis 2016; Shaw and Weller 2016; Adcroft, Hill, and Marshall 1997). Another common approach is to construct terrain-following coordinates that minimize the PGE as best as possible (e.g., Schär et al. 2002). Some authors have suggested approximations based on the conservation of integral properties or other basic physical principles (e.g., Lin 1997). Another common theme that can be identified in the literature is the use of higher order approximations to reduce the PGE (Song 1998; Song and Wright 1998). Song (1998) has also proposed a general framework based on the so called density-jacobian form of the PGF that in principle can be applied to all kinds of terrain-following coordinates.

In practice the simulation of an atmosphere-at-rest is rare and generally only carried out to validate dynamical cores. However, there is clearly considerable interest in the reduction of PGF related errors as evidenced by the amount of literature on the topic. The reason for this is that in atmospheric modeling one is interested in simulating relatively small deviations from a resting atmospheric background state. For instance, even strong storms only violate the hydrostatic equilibrium by about 20 % (e.g., Klemp and Wilhelmson 1978). That is, most common atmospheric conditions are merely small perturbations of an underlying equilibrium. Failure to account for such background states can potentially hinder the correct resolution of the perturbations of interest. Increasing the resolution can in principle resolve such issues, but the computational cost can easily become prohibitive especially for climate simulations with long integration times.

One example of detrimental effects of the PGE in realistic simulations is given by Steppeler, Bitzer, Janjić, et al. (2006). The authors suggest that reduction of the PGE via a cut-cell approach substantially improved precipitation forecasts due to improved representation of clouds in the vicinity of mountains.

3.1.1 The Cartesian System

The pressure gradient force is one of the main drivers of atmospheric motion (e.g., Haltiner and Williams 1980) and plays a prominent role in any kind of primitive equation model. In the absence of wind speed and external forcing the PGF is in fact the sole source of movement in the primitive equations. In cartesian coordinates it is commonly written

$$\mathbf{F}_{\nabla p} = \frac{1}{\rho}\nabla p \tag{3.1}$$

where $\mathbf{F}_{\nabla p}$ denotes the pressure gradient force, ∇ the gradient and ρ the density of the fluid. Note that the gradient is a vector quantity and equation (3.1) therefore has three components. It is instructive to examine the PGF in a hydrostatic equilibrium, i.e., a state of balance between the forces pushing an air parcel downwards and those lifting it upwards (see Figure 3.3). The vertical component of the PGF must then be counteracted by a gravitational force that has equal magnitude but acts in the opposite direction. Furthermore, in a state of rest the horizontal components have to vanish as well. That gives:

$$\mathbf{F}_{\nabla p} + \nabla\Phi = \begin{pmatrix} \frac{1}{\rho}\frac{\partial p}{\partial x} \\ \frac{1}{\rho}\frac{\partial p}{\partial y} \\ \frac{1}{\rho}\frac{\partial p}{\partial z} + \frac{\partial \Phi}{\partial z} \end{pmatrix} = \mathbf{0} \tag{3.2}$$

Note that the horizontal components of the gravitational force in (3.2) vanish due to the alignment of coordinate surfaces with the surfaces of constant geopotential in the cartesian system.

It is the representation of such stationary states, i.e., atmospheres-at-rest, in a numerical model that this thesis will be largely concerned with. If any given discretization of equa-

Buoyancy
Air Parcel
Gravity

Figure 3.3: *Illustration of the hydrostatic balance.*

tion (3.2) fails to evaluate to zero in a stationary state then spurious acceleration will be introduced into the model atmosphere. For the horizontal components any discretization yielding zero in a state of rest will suffice. For instance, centered finite-differences have this property. However, for the vertical component both terms are non-zero even in a state of rest and therefore have to cancel each other. The discrete approximations to these terms must be carefully engineered to respect a discrete rendition of the hydrostatic balance:

$$\frac{1}{\rho}\frac{\partial p}{\partial z} + \frac{\partial \Phi}{\partial z} = 0 \tag{3.3}$$

To illustrate the problem consider a standard centered difference approximation to the vertical component of (3.2) in a one-dimensional setting. Suppose equidistant gridpoints in the vertical z_{i-1}, z_i and z_{i+1} are given with spacing $\Delta z > 0$. Additionally, point values of pressure p and density ρ at these points are also given, i.e., $p_i = p(z_i), \rho_i = \rho(z_i)$ and so on. The goal is to approximate the PGF at z_i. Discretizing the derivative of the pressure with a centered difference and using $\frac{\partial \Phi}{\partial z} = g$ the discrete rendition of (3.3) reads:

$$\left(\frac{1}{\rho}\frac{\partial p}{\partial z}\right)\bigg|_{z_i} + g = \frac{1}{\rho_i}\frac{p_{i+1} - p_{i-1}}{2\Delta z} + g + o(\Delta z^2) \tag{3.4}$$

The Landau symbol on the right hand side of (3.4) is due to the approximation of the pressure term with a second-order accurate approximation. Assuming sufficient smoothness a Taylor expansion around the point z_i gives further insight into the nature of the resulting error:

$$\frac{1}{\rho_i}\frac{p_{i+1} - p_{i-1}}{2\Delta z} + g = \left(\frac{1}{\rho}\frac{\partial p}{\partial z}\right)\bigg|_{z_i} + g + \frac{1}{\rho_i}\sum_{n=1}^{\infty}\frac{1}{(2n+1)\,!}\frac{\partial^{(2n+1)} p}{\partial z^{(2n+1)}}\,(\Delta z)^{2n} \tag{3.5}$$

The first two terms on the left hand side of equation (3.5) cancel each other in a state of hydrostatic equilibrium. This shows that this discretization will in general not be able to retain the hydrostatic equilibrium, because the remaining third term is not balanced by a suitable counterpart. With decreased grid spacing the resulting error will decrease quadratically, but even if the initial error is small, it can grow over time and lead to considerable erroneous motion. Moreover, increasing the resolution also incurs higher computational costs. Ideally, a discretization of (3.3) should be engineered to net exactly zero in hydrostatic equilibrium even on coarse grids. This concept will be expanded on in a later section when discussing the idea of well-balanced methods.

To sum up, standard discretizations of the vertical pressure gradient force fail to retain the hydrostatic equilibrium even in the cartesian coordinate system. This is due to unbalanced local truncation errors resulting from approximations with finite differences. Retention of atmospheres-at-rest is therefore not only a problem with terrain-following coordinate systems as is sometimes implied in the literature. However, as will be seen in the following terrain-following coordinates indeed exacerbate this issue.

3.1.2 The Hybrid η-System

So far the pressure gradient force as found when using the classic height or z-coordinate has been investigated. Discrete errors occur as a result of truncation errors in the vertical momentum equation, potentially inducing spurious movement into an atmosphere-at-rest. Naturally, in hydrostatic models such as REMO the third component of (3.2) always holds, because the atmosphere is assumed to be in hydrostatic balance permanently. Such models do not feature a prognostic vertical momentum equation and hence no spurious momentum can be generated in this way. Yet, retaining states of rest remains a challenge (see Figure 3.1) in terrain-following systems.

As discussed in subsection 2.2.2 the REMO model uses the hybrid terrain following η-coordinate. To understand why computing the pressure gradient force is prone to errors equation (3.2) written in the η-system will be investigated. According to Kasahara (1974) in this system the horizontal pressure gradient force can be written:

$$\mathbf{F}^{\eta}_{\nabla p} = \begin{pmatrix} \frac{1}{a\cos\varphi}\left[RT_v\frac{\partial \ln p}{\partial\lambda} + \frac{\partial\Phi}{\partial\lambda}\right] \\ \frac{1}{a}\left[RT_v\frac{\partial \ln p}{\partial\varphi} + \frac{\partial\Phi}{\partial\varphi}\right] \end{pmatrix} \tag{3.6}$$

Note that the vertical component has been omitted as it vanishes due to the hydrostatic assumption. It can be seen that horizontal balances in (3.6) analogous to the vertical one in (3.2) appear. A balance emerges between a pressure and a gravitational term, that will cancel each other in a state of rest. The approximations to these terms must be balanced with respect to such states or spurious horizontal momentum will be introduced into the model atmosphere. Error resulting from a lack of cancellation of these approximations is often referred to as the pressure gradient error (PGE). In contrast to the cartesian system the truncation errors have to be balanced in two components rather than just one. This is one of the reasons the pressure gradient error is often found to be exacerbated in terrain-following coordinate systems. In fact, in case of non-hydrostatic models with terrain-following coordinates the approximations in all three components have to be balanced. Sundqvist (1975) found that the absolute value of the individual terms in (3.6) can surpass the value of their sum by up to 20 times. The truncation errors will scale with the size of these individual terms. Therefore, if unbalanced the truncation errors can severely impose on the actual quantity of interest, namely the (horizontal) momentum. For instance an error of 1 % in both terms can result in errors of up to 40 % in the horizontal momentum.

Despite the strong similarities to the issues encountered with the vertical z-coordinate previously there are also subtle differences. In (3.2) the balance is between the pressure gradient force and the gravitational force. For a hypothetical atmosphere without gravity the second term would simply vanish and no balancing problem would arise. In (3.6) on the other hand the balance as a whole merely describes the horizontal pressure gradient force itself. Even an atmosphere without gravity would result in a similar balance of opposing terms in the terrain-following coordinate. To elucidate this surprising difference the transformation of the horizontal PGF to the η-system has to be investigated. Using the chain rule the derivatives of the pressure can be converted between the two coordinate systems. Restricting to just one of the two momentum equations to demonstrate the principle:

$$\frac{1}{\rho}\left(\frac{\partial p}{\partial x}\right)_z = \frac{1}{\rho}\left(\frac{\partial p}{\partial x}\right)_\eta - \frac{1}{\rho}\frac{\partial p}{\partial z}\left(\frac{\partial z}{\partial x}\right)_\eta \tag{3.7}$$

Here the subscripts indicate whether the derivatives are taken along surfaces of constant z or η. Equation (3.7) shows that the representation of the PGF in η-coordinates naturally leads to a sum of two terms. This is independent of whether gravity is considered in the equations or not. Substituting the hydrostatic equation $\frac{\partial p}{\partial z} = -g\rho$ leads to:

$$\frac{1}{\rho}\left(\frac{\partial p}{\partial x}\right)_z = \frac{1}{\rho}\left(\frac{\partial p}{\partial x}\right)_\eta + g\left(\frac{\partial z}{\partial x}\right)_\eta \tag{3.8}$$

Finally, using the ideal gas law and $\Phi = gz$ yields the form that is used in the REMO model:

$$\frac{1}{\rho}\left(\frac{\partial p}{\partial x}\right)_z = RT\left(\frac{\partial \ln p}{\partial x}\right)_\eta + \left(\frac{\partial \Phi}{\partial x}\right)_\eta \tag{3.9}$$

Note that the remaining differences to (3.6) are due to the additional transformation to spherical-type coordinates and the addition of moisture equations. These aspects are not relevant for this discussion. The important point is that the balancing problem in the horizontal momentum equations is due to the vertical coordinate transformation. The balancing problem in the vertical momentum equation instead stems from the addition of gravity to the general Euler equations.

3.2 Well-Balanced Numerical Methods

Previously the pressure gradient error as found in most primitive equation models of the atmosphere has been described. Related problems also arise in other branches of scientific modeling, such as astrophysics (Käppeli and Mishra 2016), nozzle flows (Xing and Shu 2006) or shallow-water applications (Noelle et al. 2006). The common theme is the existence of nontrivial stationary or steady states owing to the balance of two opposing terms. These terms have to cancel each other on a discrete level to retain the equilibria and require discretizations specifically engineered for this purpose. In almost all instances such problems arise from the addition of source terms to a given hyperbolic conservation law. In abstract terms a conservation law can be described in differential form as

$$\frac{\partial q}{\partial t} + \nabla \cdot f(q) = 0 \tag{3.10}$$

where q is the vector of conserved quantities and f is called the flux function. The divergence of f is often referred to as the flux gradient. Common examples of such systems include the Euler equations of motion and the shallow-water equations. In many modeling applications a solution dependent term is added to the RHS of (3.10):

$$\frac{\partial q}{\partial t} + \nabla \cdot f(q) = s(q) \tag{3.11}$$

Equation (3.11) is then referred to as a balance law and s is called a source term. Clearly, in a state of equilibrium a balance between the flux gradient and the source term must hold:

$$\nabla \cdot f(q) = s(q) \tag{3.12}$$

In general both of these terms will be non-zero, equal in magnitude but opposite in sign. Any discretization of the balance law (3.11) must respect a discrete version of (3.12). Failure to do so will result in a spurious non-zero rate of change for the state vector q. Typical examples of balance laws include the shallow water equations with bottom topography and the Euler equations with gravity and or Coriolis force. It was already seen in the preceding section that the addition of gravity to the equations of motions indeed prompts a balance of this kind in the vertical momentum budget.

The first publication to systematically investigate problems of this nature was Greenberg and Leroux (1996). The authors also coined the notion of well-balanced schemes to describe numerical methods conceived to retain equilibria of the kind (3.12). For any convergent scheme errors resulting from unbalanced approximations of (3.12) can simply be reduced by increasing the resolution. The problem is that the computational cost of a sufficiently high resolution is often prohibitive. Therefore, a well-balanced discretization of (3.11) should ideally respect a discrete version of (3.12)

- for all equilibria of equation (3.11)

- independently of the given grid resolution
- and at affordable computational cost

Many well-balanced schemes developed in the literature can only fulfill these goals partially. For instance, often the first requirement is violated and only certain subclasses of equilibria can be maintained. In other cases the schemes do not fully resolve (3.12) but merely allow for an improved cancellation, i.e., are not independent of the grid resolution.

One of the aims of this thesis is to evaluate the applicability of existing well-balanced schemes to the REMO model. In the past 20 years many well-balanced discretizations have been proposed for different branches of modeling. However, most approaches are bound to the particular equation system governing the applications at hand instead of providing a generalized strategy to construct well-balanced schemes. For instance, many publications study the shallow water equations and the well-known lake-at-rest equilibrium, e.g., LeVeque (1998) and Audusse et al. (2004) to name just two seminal examples. Therefore, this discussion is restricted to the available literature on the Euler equations.

Most of the developments revolve around the use of FVMs. Such methods are based on an integral version of the conservation or balance law to be solved. The domain of interest is partitioned into a finite number of computational cells or volumes. Given suitable prerequisites one can show that the conserved quantity can only change due to inflow or outflow through the boundaries of these cells. Averaging the values over a cell an equation for the evolution of its mean value in time can be derived. In general, polygonal cells are chosen so that the boundary integrals required to advance the mean cell value in time can be efficiently computed. However, the values at the boundary between neighboring cells need not be continuous. This is resolved by solving initial value problems with discontinuous data, referred to as Riemann problems.

The literature dealing with finite difference models such as REMO is mostly concerned with non-linear high-order schemes (e.g., Ghosh and Constantinescu 2015; Xing and Shu 2006). All of these schemes are constructed for the Euler equations formulated in a cartesian coordinate system, i.e., with a vertical z-coordinate. Some schemes only conserve the most simple equilibria while others manage to tackle a wider subset. Additionally, all of them only consider atmospheres without rotation. This shows that despite considerable effort so far no universal solution to well-balancing the Euler equations has been found. Moreover, any approach has to be adapted to the terrain-following coordinate and the specific finite difference structure of the REMO model. The approach that seems most promising in this regard is due to Botta et al. (2004). On the one hand the scheme can be applied to centered-difference schemes such as REMO even though it is mostly geared towards FVM applications. Other existing FVM schemes do not easily support the transfer to the finite difference framework. On the other hand the method does not rely on explicit characterizations of equilibrium states. As will be seen in the next section such states can be easily described in z-coordinates but doing so in the terrain-following coordinate is very difficult. Moreover, the method proposed by Botta et al. (2004) is specifically aimed at climate simulations with their long integration times. Therefore, out of the available options this approach appears to be the most suitable for application within the REMO model.

3.3 Stationary and Steady States

As previously described the aim of well-balanced methods is to retain stationary or steady states in numerical models even on rather coarse grids. Depending on the model equations and the field of application such states can take many different forms. It is therefore instructive to investigate how stationary and steady states manifest within the REMO model.

First, the distinction between steady and stationary states as used in the remainder of this work is made. Both stationary and steady states are states of equilibrium, i.e., the time derivatives of the prognostic variables in equations (2.9)–(2.15) vanish. From a continuous vantage point the state of the system will then be maintained indefinitely, because there are no changes to the prognostic variables over time. Naturally, this requires the sum of all the remaining terms to vanish as well. If there is non-zero wind speed the equilibrium is referred to as a steady state and as a stationary state otherwise. It is important to differentiate the one from the other, because steady states can be much more complex. To understand the differences a closer look will be taken at the prognostic equations under such circumstances.

If $u, v = 0$ is substituted into the prognostic equations many terms vanish right away. The integral in (2.9) equates to zero resulting in no surface pressure change. The same holds true for the vertical velocity (2.22), if additionally $\frac{\partial p_s}{\partial t} = 0$ is taken into account. For the moisture equations (2.13)–(2.15) only the advection terms remain and those clearly equate to zero as well. Hence, no change in these variables will occur. The situation for the temperature equation (2.12) is similar, except for the additional omega-alpha term. From the definition of ω in (2.24) it can be concluded that this term also vanishes. This leaves only the momentum equations (2.10) and (2.11). Here in addition to the terms mentioned above the kinetic energy K equals zero by definition. The terms containing the absolute potential vorticity Q are multiplied by v or u respectively. Consequently, the momentum equations are the only ones to retain non-zero terms in this situation.

The stationary state equations for REMO can then be stated as follows:

$$\frac{\partial u}{\partial t} = -\frac{1}{a\cos\varphi}\left(RT_v\frac{\partial \ln p}{\partial \lambda} + \frac{\partial \Phi}{\partial \lambda}\right) = 0 \tag{3.13}$$

$$\frac{\partial v}{\partial t} = -\frac{1}{a}\left(RT_v\frac{\partial \ln p}{\partial \varphi} + \frac{\partial \Phi}{\partial \varphi}\right) = 0 \tag{3.14}$$

By comparing to equation (3.6) it can be seen that the remaining terms represent the horizontal pressure gradient force in the η-system. This explains why the discretization of the PGF is so fundamental to retaining stationary states. It is the only way for movement to develop in a state of rest. Likewise, if the truncation errors of the opposing terms in the discrete version of (3.13)–(3.14) are not perfectly balanced the numerical model will eventually drift out of rest.

The situation for steady states is entirely different. Since the wind speed is non-zero none of the terms except for the time derivatives of the prognostic equations vanish by default. Consequently, the complete equation set (2.9)–(2.15) is retained. To sustain such states numerically the sum of all the remaining terms has to vanish on a discrete level. This generally requires a very complex balance between the numerous discrete terms. This thesis will therefore be restricted to stationary states and the numerical treatment of the PGF terms in (3.13) and (3.14).

Equations (3.13)–(3.14) describe the requirements for any stationary state in abstract terms. This raises the question if the nature of such states can be described in a more tangible manner. Clearly, since these equations are derived from the classical primitive equation by means of coordinate transformation the stationary states of both systems are identical. In the cartesian system they take a particularly simple form that has been described many times (e.g., Haltiner and Williams 1980). First, such states need to be vertically hydrostatic, i.e.,

$$\frac{\partial p}{\partial z} = -g\rho \tag{3.15}$$

holds. Second, they need to be horizontally homogeneous. That means the thermodynamic variables only depend on z and have no horizontal variation:

$$T = T(z), p = p(z) \text{ and } \rho = \rho(z) \tag{3.16}$$

Consequently, any variation between two points must exclusively be caused by the height difference between them. The ease of characterizing equilibrium states in cartesian coordinates unfortunately does not carry over to the η-system. To illustrate this an idealized atmosphere will be analytically transferred to the η-system. This idealized atmosphere will be modeled after the US standard atmosphere (see NASA 1976). It will also serve as a basis for testing the ability of the numerical developments to retain an atmosphere-at-rest in later chapters.

The standard atmosphere is characterized by a piecewise linear vertical temperature distribution given as a function of geopotential altitude. Note that gravity in REMO is assumed to have no vertical variation and therefore the difference between geopotential and geometric altitude can be ignored for this purpose. Together with given initial values at a reference height the atmospheric pressure can then be derived from equation (3.15). The density values required can be diagnosed from the ideal gas equation resulting in a horizontally homogeneous and vertically hydrostatic state. Table 3.1 lists the reference values at various altitudes and the linear temperature lapse rates assumed between those. The temperature in any of the atmospheric layers described in Table 3.1 can be written

Table 3.1: Standard Atmosphere in REMO

Name	Height [m]	Pressure [hPa]	Temperature [K]	Lapse Rate [K/m]
Troposphere	0.0	1013.25	288.15	0.0065
Tropopause	11000	226.320	216.65	0.0
Stratosphere	20000	54.7488	216.65	-0.001
Stratosphere	32000	8.68017	228.65	-0.0028
Stratopause	47000	1.10906	270.65	0.0
Mesosphere	51000	0.66939	270.65	0.0028
Mesosphere	71000	0.03956	214.65	0.002

$$T(z) = T_{ref} - l_{ref}\left(z - z_{ref}\right) \tag{3.17}$$

where T_{ref} and z_{ref} are the reference temperature and height at the bottom of the layer and l_{ref} the lapse rate through the layer. Substituting the ideal gas law

$$\rho = \frac{p}{RT} \tag{3.18}$$

into equation (3.15) and using (3.17) an initial value problem for the logarithm of the atmospheric pressure can be posed as follows:

$$\frac{\partial \ln p}{\partial z} = -\frac{g}{R\left(T_{ref} - l_{ref}\left(z - z_{ref}\right)\right)}, \; p(z_{ref}) = p_{ref} \tag{3.19}$$

Here z_{ref} and p_{ref} are the reference height and pressure respectively at the bottom of the layer of interest. Equation (3.19) is separable, i.e., it can be solved by vertically integrating the equation from the reference height upwards. This leads to:

$$\ln p = \ln p_{ref} - \frac{g}{R}\int_{z_{ref}}^{z} \frac{1}{T_{ref} - l_{ref}\left(z' - z_{ref}\right)}\,\mathrm{d}z' \tag{3.20}$$

To retrieve an explicit expression for the pressure the integral on the RHS of (3.20) must be solved. With the antiderivative of the integrand the integral can be restated as:

$$\int_{z_{ref}}^{z} \frac{1}{T_{ref} - l_{ref}\left(z' - z_{ref}\right)}\,\mathrm{d}z' = \left[-\frac{1}{l_{ref}}\ln\left(T_{ref} - l_{ref}\left(z - z_{ref}\right)\right)\right]_{z_{ref}}^{z} \tag{3.21}$$

to arrive after some further rearrangement at:

$$p = p_{ref}\left(\frac{T_{ref} - l_{ref}\left(z - z_{ref}\right)}{T_{ref}}\right)^{\frac{g}{Rl_{ref}}} \tag{3.22}$$

However, equation (3.22) only holds for non-zero lapse rates. If the lapse rate vanishes this reads:

$$p = p_{ref}\exp\left(-\frac{g\left(z - z_{ref}\right)}{RT_{ref}}\right) \tag{3.23}$$

With equations (3.22) and (3.23) the standard atmosphere can be created according to the layer definitions in Table 3.1. Figure 3.4 shows a plot of the resulting temperature and pressure distribution. Note that small differences to the definition of the US standard atmosphere can occur due to slightly different values of R and g. For consistency the values from the REMO model are used here. The standard atmosphere can now be

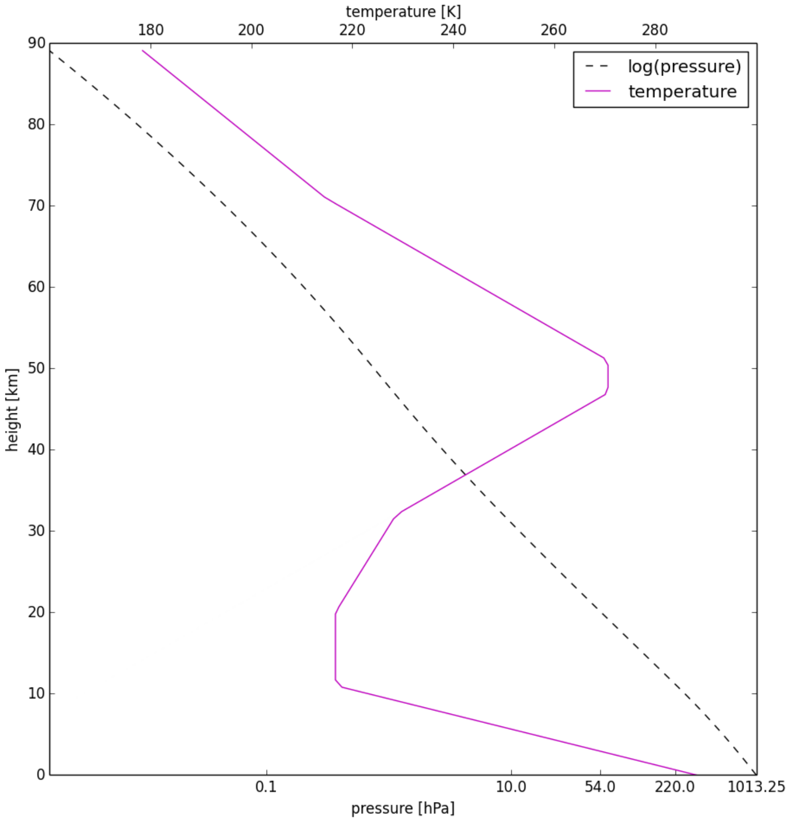

Figure 3.4: *Plot of pressure and temperature distribution for the standard atmosphere.*

transferred to the η-system. To that end, the above relationships between pressure and height will be inverted. For non-zero lapse rates this gives

$$z = z_{ref} + \frac{T_{ref}}{l_{ref}} \left(1 - \left(\frac{p}{p_{ref}} \right)^{\frac{Rl_{ref}}{g}} \right) \tag{3.24}$$

and otherwise:

$$z = z_{ref} - \frac{RT_{ref}}{g} \ln \frac{p}{p_{ref}} \tag{3.25}$$

With equations (3.24) and (3.25) any pressure value can be mapped onto the corresponding geometric height. Substituting relationship (2.6) into the above equations yields the geometric height as a function of η:

$$z = z_{ref} + \frac{T_{ref}}{l_{ref}} \left(1 - \left(\frac{A(\eta) + B(\eta)p_s}{p_{ref}} \right)^{\frac{Rl_{ref}}{g}} \right) \tag{3.26}$$

Substituting (3.26) into the definition of the temperature in (3.17) gives:

$$T = T_{ref} \left(\frac{A(\eta) + B(\eta)p_s}{p_{ref}} \right)^{\frac{Rl_{ref}}{g}} \tag{3.27}$$

Equations (3.26) and (3.27) show that even a simple linear temperature distribution in the z-coordinate leads to nonlinear power laws for temperature and height in the η-system. These also depend on p_s which is dominated by the orographic structure. In this way, more complex terrain gives rise to more intricate representations of the basic thermodynamic variables. Figure 3.5 shows a plot of the temperature and geopotential distributions in the η-system up to a height of 30 km for the parabola-shaped hill. The lines of constant temperature and geopotential show the expected curvature due to the given orography. Towards higher altitudes the lines flatten and the influence of the terrain is reduced gradually. Above the defined pressure threshold the lines become completely isobaric.

3.4 A Novel Characterization of Equilibrium

In this section an alternative characterization of stationary states that only relies on pressure and temperature is derived, that makes no reference to the geopotential. To that end, the integro-differential equation (4.20) is cast into the form:

$$-RT \frac{\partial \ln p}{\partial \lambda} = \frac{\partial \Phi_s}{\partial \lambda} - \frac{\partial}{\partial \lambda} \int_1^{\eta} RT \frac{\partial \ln p}{\partial \eta} \, \mathrm{d}\eta' \tag{3.28}$$

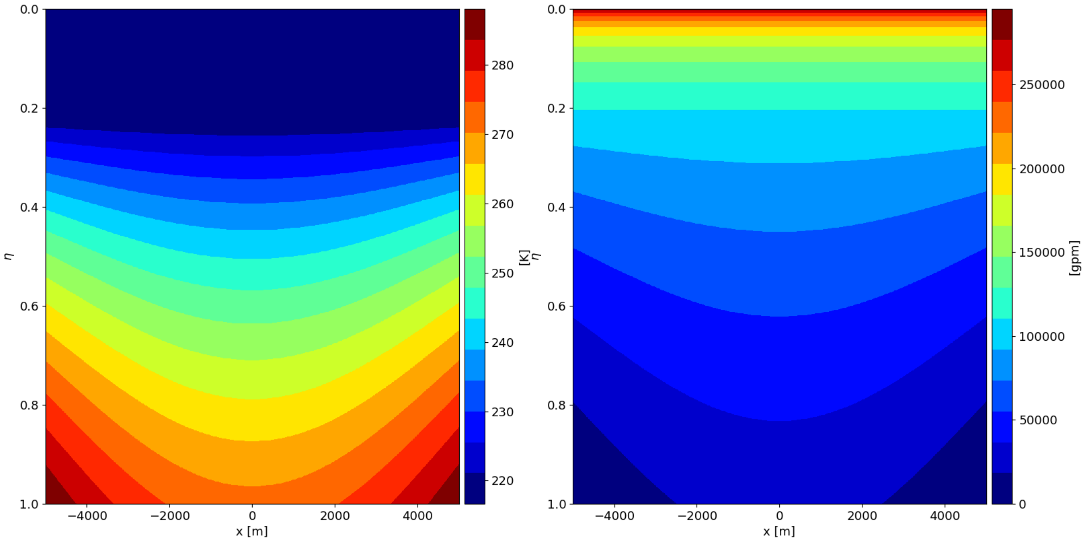

Figure 3.5: *Temperature (left) and Geopotential (right) in the η-system.*

This is a rendition of the complete stationary state equation for the REMO model. The standard discretization in REMO is constructed by using centered differences for the horizontal and vertical derivatives. The integral on the right hand side is evaluated with the midpoint rule as detailed in chapter 2. Consequently, the resulting discrete operators are structured very differently. The pressure term is discretized in a purely local manner relying only on known values of p and T along the given coordinate surface. Contrary to this the discretization of the geopotential term involves values not only from the given coordinate surfaces, but also from all the coordinate surfaces below it down to the surface layer. This is a consequence of enforcing the hydrostatic assumption via equation (2.18). Cancellation thus requires a delicate discrete balance between a number of terms, that continually increases towards the top of the model atmosphere.

First, transposing differentiation and integration in (3.28) – note that this is only possible because the derivatives are taken along surfaces of constant η – and integrating by parts yields the following representation for the gradient of the geopotential:

$$\begin{aligned}
\frac{\partial \Phi}{\partial \lambda} &= \frac{\partial \Phi_s}{\partial \lambda} - R\int_1^\eta \frac{\partial T}{\partial \lambda}\frac{\partial \ln p}{\partial \eta} + T\frac{\partial^2 \ln p}{\partial \eta \partial \lambda}\,\mathrm{d}\eta' \\
&= \frac{\partial \Phi_s}{\partial \lambda} - R\int_1^\eta \frac{\partial T}{\partial \lambda}\frac{\partial \ln p}{\partial \eta}\,\mathrm{d}\eta' - R\left[T\frac{\partial \ln p}{\partial \lambda}\right]_1^\eta + R\int_1^\eta \frac{\partial T}{\partial \eta}\frac{\partial \ln p}{\partial \lambda}\,\mathrm{d}\eta' \\
&= \frac{\partial \Phi_s}{\partial \lambda} + R\int_1^\eta \frac{\partial T}{\partial \eta}\frac{\partial \ln p}{\partial \lambda} - \frac{\partial T}{\partial \lambda}\frac{\partial \ln p}{\partial \eta}\,\mathrm{d}\eta' - R\left(T\frac{\partial \ln p}{\partial \lambda} - T_s\frac{\partial \ln p_s}{\partial \lambda}\right) \\
&= \left(\frac{\partial \Phi_s}{\partial \lambda} + T_s\frac{\partial \ln p_s}{\partial \lambda}\right) + R\int_1^\eta \frac{\partial T}{\partial \eta}\frac{\partial \ln p}{\partial \lambda} - \frac{\partial T}{\partial \lambda}\frac{\partial \ln p}{\partial \eta}\,\mathrm{d}\eta' - RT\frac{\partial \ln p}{\partial \lambda}
\end{aligned} \tag{3.29}$$

It can immediately be seen that the surface term in brackets vanishes due to the lower boundary condition $u = 0$. Substituting the result back into equation (3.28) then yields:

$$R\int_1^\eta \frac{\partial T}{\partial \lambda}\frac{\partial \ln p}{\partial \eta} - \frac{\partial T}{\partial \eta}\frac{\partial \ln p}{\partial \lambda}\,\mathrm{d}\eta' = R\int_1^\eta \frac{\partial}{\partial \lambda}\left(T\frac{\partial \ln p}{\partial \eta}\right) - \frac{\partial}{\partial \eta}\left(T\frac{\partial \ln p}{\partial \lambda}\right)\mathrm{d}\eta' = 0 \tag{3.30}$$

That is, any stationary state can be characterized by the vanishing of the integrals in (3.30). Moreover, outside of equilibrium these integrals describe the residual of the stationary state equation, i.e., the horizontal PGF. Note that the above equation gives rise to a geometrical interpretation of an equilibrium state. The integral on the RHS of (3.30) has to vanish for any given η for the equation to hold. It can be deduced that the integrand vanishes as well. That is, the partial differential equation

$$\frac{\partial}{\partial \lambda}\left(RT\frac{\partial \ln p}{\partial \eta}\right) - \frac{\partial}{\partial \eta}\left(RT\frac{\partial \ln p}{\partial \lambda}\right) = 0 \tag{3.31}$$

holds. If a vector field of the form

$$\begin{pmatrix} RT\frac{\partial \ln p}{\partial \lambda} \\ RT\frac{\partial \ln p}{\partial \eta} \end{pmatrix} \tag{3.32}$$

is pictured, then equation (3.31) essentially states that it is curl-free. Such vector fields have scalar potentials, i.e., can be expressed as the gradient of a scalar function. Clearly, this potential must be given by the geopotential:

$$\nabla \Phi = \begin{pmatrix} RT\frac{\partial \ln p}{\partial \lambda} \\ RT\frac{\partial \ln p}{\partial \eta} \end{pmatrix} \tag{3.33}$$

The second component of (3.33) is simply the hydrostatic equation which always holds. The first component is the stationary state equation and only holds for equilibrium states. In such cases (3.31) simply reduces to Schwarz's theorem applied to Φ:

$$\frac{\partial^2 \Phi}{\partial \lambda \partial \eta} = \frac{\partial^2 \Phi}{\partial \eta \partial \lambda} \tag{3.34}$$

The advantage of using equation (3.30) to characterize the equilibrium is that both the surface geopotential term and the pressure term have already been eliminated. An integral over the whole atmospheric column as in (3.28) is still retained, but it suffices to balance the integrand in each level individually. In (3.28) the integral has to cancel with both the remaining surface terms instead. Moreover, the structure of the opposing terms in the remaining balance under the integral is rather similar. The transposition of derivatives is the only difference here. This equation also gives rise to an intuitive geometric interpretation of stationary states in the η-system. Namely, a state is stationary if and only if the change in a thermodynamic variables between two points in the atmosphere is exclusively due to their difference in geometric height. This will be useful in developing a reconstruction technique in the next chapter.

4 Well-Balancing Strategy

In this chapter the balancing strategy that will be applied to the REMO model in the subsequent chapters is derived. In the first section the approach for a co-located grid structure is developed. Subsequent sections then aim to transfer this approach to the staggered grid used in REMO as described in chapter 2. It turns out that some of the differences to the framework of Botta et al. (2004), namely the change from a height-based to a pressure-based coordinate system and the presence of horizontal and vertical grid staggering, present substantial additional challenges. Therefore modifications to the basic method are developed as needed and a well-balancing strategy that can readily be applied to the REMO model is presented towards the end of this chapter.

4.1 Introductory Example

It has been seen previously that balancing problems in computing the PGF can arise in different ways. The addition of gravity to the Euler equations results in a balance in the vertical momentum budget irrespective of the coordinate system used. Employing a terrain-following coordinate system additionally poses analogous problems in the horizontal momentum equations. The method developed by Botta et al. (2004) is geared towards the z-coordinate, i.e., is built to deal with the spurious generation of vertical momentum. Before applying these ideas to the horizontal momentum equations in REMO it is instructive to demonstrate them on a simple Cartesian example given by Botta et al. (2004). Therefore, in this introductory section a one-dimensional example with a vertical z-coordinate is examined. As pointed out before in this situation the balancing problem can only occur in the vertical momentum budget, as the horizontal gradient of the geopotential taken along the coordinate lines naturally vanishes. In this one-dimensional example there is no difference between hydrostatic and stationary states. Therefore, the starting point is the familiar hydrostatic equation:

$$\frac{\partial w}{\partial t} = \frac{\partial p}{\partial z} + \rho \frac{\partial \Phi}{\partial z} = \frac{\partial p}{\partial z} + \rho g = 0 \tag{4.1}$$

Assume now that this equation is discretized on a regular grid $(z_i)_{i \in I}$ with spacing Δz using centered differences in the vertical. The time discretization will not be specified, as this is not of importance for the following considerations. Now let p_i, ρ_i be exactly hydrostatic point values, i.e., for these values (4.1) holds exactly on a continuous level. Ideally in such a case the discrete version of (4.1)

$$\frac{p_{i+1} - p_{i-1}}{2\Delta z} + \rho_i g = 0 \tag{4.2}$$

should also hold and the scheme would be well-balanced. However, this is generally not the case. While the second term in (4.2) will be evaluated exactly, the first term will be afflicted with a truncation error that is caused by the approximation to the gradient of the pressure with a finite difference. The magnitude of this error will depend on the grid spacing Δz. Especially on rather coarse grids the error induced in (4.2) can introduce spurious momentum into the system. Over time such errors can conflate and grow leading to considerable vertical motion. One idea to tackle this issue is to seek a discretization for the gradient of the geopotential that allows for better cancellation of the overall equation. In addition to the references given earlier such an approach has for example been applied successfully to the shallow-water equations in Audusse et al. (2004). Following these ideas the second term in (4.2) is represented discretely by

$$\rho_i g \approx -\frac{p^*_{i+1} - p^*_{i-1}}{2\Delta z} \tag{4.3}$$

with a suitable pressure variable p^*. Using the same discrete gradient formulation for both terms in equation (4.2) a substantial improvement of cancellation can be expected. Clearly, the question is how to construct an appropriate pressure p^* to achieve this. On the one hand for stationary states ideally $p^* = p$ would hold to yield perfect cancellation. On the other hand the RHS of (4.3) must still be a valid second-order approximation to the gradient of the geopotential. In general as will be seen later only the latter requirement can be fulfilled exactly with the approach presented here. However notable improvements with regards to the former requirement can still be realized, as long as p^* is constrained to stay close to the current model pressure p.

A natural approach to construct suitable candidates for p^* is to solve (4.1), i.e., to find pairs of hydrostatically balanced solutions p^*, ρ^* around a given grid point z_i. Locally this gives:

$$\frac{\partial p^*}{\partial z} = -\rho^* g \tag{4.4}$$

However, the ordinary differential equation (4.4) on its own does not provide unique solutions. The remaining degrees of freedom, namely a cell-centered initial value at $z = z_i$ and provision of ρ^*, can then be used to constrain p^* towards p around z_i. To this end it is required that p^* take the given point value of the model pressure at the cell center:

$$p^*(z_i) = p(z_i) = p_i \tag{4.5}$$

The goal is to integrate (4.4) together with (4.5). However, a local density distribution ρ^* has still to be provided. Note that for any p^* acquired in this manner it is by construction

$$-\frac{p^*_{i+1} - p^*_{i-1}}{2\Delta z} = \frac{g}{2\Delta z} \int_{z_{i-1}}^{z_{i+1}} \rho^* \ \mathrm{dz}' \tag{4.6}$$

provided (4.4) can be integrated analytically across the cell. This is referred to as the discrete Archimedes buoyancy principle. It can be shown (see Botta et al. 2004) that for any ρ^* with $\rho^*(z_i) = \rho(z_i) = \rho_i$ the left hand side (LHS) of equation (4.6) yields a second-order approximation to the term $g\rho_i$ of (4.3). Instead of the naive formulation (4.2) (4.1) can now be discretized by

$$\frac{p_{i+1} - p_{i-1}}{2\Delta z} - \frac{p^*_{i+1} - p^*_{i-1}}{2\Delta z} \tag{4.7}$$

retaining the second-order accuracy. If ρ^* is exactly equal to ρ around z_i and the pair p, ρ is hydrostatically balanced then (4.4) and (4.5) will yield $p^* = p$. Then both terms in (4.7) will cancel out perfectly. Therefore, the better of an approximation ρ^* is to ρ, the more well-balanced the approximation (4.7) can be expected to be.

To sum up, the fundamental idea is to express both the pressure gradient and the gravitational source term with the same discrete approximation. This is achieved by finding local hydrostatic background states p^*, ρ^* via solving the hydrostatic equation. Suitable initial values and the provision of a local density approximation ensure that the hydrostatic solutions stay close to the current model state. With the help of these functions an approximation to the source term can then be constructed employing the discrete Archimedes buoyancy principle.

This technique is remarkably similar to the widespread technique of subtracting a hydrostatic reference profile to reduce cancellation errors (e.g., Gary 1973). However, the above approach has two major advantages. Firstly the background states are local to each cell instead of spanning whole vertical columns. This allows for improved approximation of the hydrostatic components. Secondly the background states are readjusted to the evolving conditions in each timestep. This is very important for applications in climate simulations. Over time any initially computed background state may cease to approximate the hydrostatic components of the solution. Adjusting the background state in each timestep to the evolving atmospheric conditions allows for continued benefits throughout long integrations.

4.2 Balancing in η-Coordinates

In this section the ideas presented previously are applied to the numerical scheme of the hydrostatic regional climate model REMO as described in chapter 2. Particular difficulties arise from the nature of the pressure-based vertical coordinate, the hydrostatic assumption and the use of a staggered Lorenz-type computational grid. These challenges will be addressed step by step to yield a scheme directly applicable to the REMO model towards the end of this section.

The aim is to transfer the ideas put forward in the previous section to the REMO framework. It has already been seen in section 3.1 that one of the key differences stems from the vertical coordinate system. In the Cartesian vertical coordinate z the balancing problem arises due to the addition of a source term that represents gravity. It is limited to the vertical equation of motion. In the η-system the balancing problem is a consequence of the coordinate transformation itself and essentially unrelated to the source term. It is restricted to the horizontal momentum equations.

On the other hand the structural similarity of the resulting terms in (3.3) and each component of (3.6) is striking. In both cases the balance of a pressure and a gravitational term characterizes certain equilibrium states. In one case these are hydrostatic and in the other stationary states. Failure to respect such balances in the discrete approximations leads to unbalanced local truncation errors and generation of spurious vertical or horizontal momentum respectively. Therefore, it appears promising to adapt the technique from the example section 4.1 to the REMO framework.

Firstly, note that the following developments can be applied independently in both horizontal directions and that this exposition can with no loss of generality be restricted to a horizontally one-dimensional setting. Moreover, the analysis of the stationary state equations in section 3.3 suggests that the momentum equations are the only potential source of erroneous movement. Consequently, a dry atmosphere can be assumed for this purpose. In that case the virtual temperature reduces to the absolute temperature: $T_v = T$. The stationary state equation (3.13) can then be written:

$$-\frac{1}{a\cos\varphi}\left(RT\frac{\partial \ln p}{\partial\lambda} + \frac{\partial\Phi}{\partial\lambda}\right) = 0 \tag{4.8}$$

To formulate a general roadmap the steps taken to improve local truncation error (LTE) cancellation in the example from section 4.1 are recapitulated. The aim is to express both terms in (4.8) with the same discrete formulation. To that end, local stationary states are constructed by solving equation (4.8) under provision of suitable initial conditions and local thermodynamic approximations. These local stationary states will then be used to construct approximations to the horizontal PGF with improved cancellation properties via the discrete Archimedes buoyancy principle.

To express these ideas most clearly it is assumed in this section that the equations are solved on a co-located grid. That means all prognostic and diagnostic quantities are assumed to be located at the same points in the discrete grid structure. In later sections the basic method will be adapted to the vertical and horizontal staggering used in the REMO model. In this setting the discrete grid points take the form (λ_i, η_j) with the notation from chapter 2. Assume that discrete point values p_{ij}, T_{ij} and Φ_{ij} of pressure, temperature and geopotential at these locations are given. In practice this will either be initial data or the values computed for the last timestep during the course of a simulation.

To construct a discrete approximation of (4.8) on the co-located grid the pressure term is treated first. Using standard centered finite differences a second-order approximation to $\frac{\partial \ln p}{\partial \lambda}$ at a given gridpoint (λ_i, η_j) can be given as:

$$\frac{\partial \ln p}{\partial \lambda} = \frac{\ln p_{i+1j} - \ln p_{i-1j}}{2\Delta\lambda} + o\left(\Delta\lambda^2\right) \tag{4.9}$$

To gain more insight into the nature of the LTE a Taylor-expansion of $\ln p$ around the central point (λ_i, η_j) is applied. Assuming sufficient smoothness this gives:

$$\frac{\ln p_{i+1j} - \ln p_{i-1j}}{2\Delta\lambda} = \frac{1}{2\Delta\lambda}\sum_{n=0}^{\infty}\frac{1}{n!}\left(\frac{\partial^n \ln p}{\partial\lambda^n}\left(\lambda_{i+1}-\lambda_i\right)^n - \frac{\partial^n \ln p}{\partial\lambda^n}\left(\lambda_{i-1}-\lambda_i\right)^n\right) \tag{4.10}$$

The even terms in the sum in equation (4.10) cancel and the odd terms double, because of $(\lambda_{i+1} - \lambda_i) = \Delta\lambda$ and $(\lambda_{i-1} - \lambda_i) = -\Delta\lambda$. Isolating the first term yields:

$$\frac{\ln p_{i+1j} - \ln p_{i-1j}}{2\Delta\lambda} = \left.\frac{\partial \ln p}{\partial\lambda}\right|_{ij} + \sum_{n=1}^{\infty}\frac{1}{(2n+1)\,!}\frac{\partial^{(2n+1)}\ln p}{\partial\lambda^{(2n+1)}}\left(\Delta\lambda\right)^{2n} \tag{4.11}$$

That is, the local truncation error decreases at least quadratically with the horizontal grid spacing $\Delta\lambda$.

Assume now that a local stationary state is given, i.e., a pair of temperature and pressure (T^*, p^*) that solves (4.8) around the cell-center (λ_i, η_j):

$$\frac{\partial \ln p^*}{\partial\lambda} = -\frac{1}{RT^*}\frac{\partial\Phi}{\partial\lambda} \tag{4.12}$$

If the same discrete difference operator used for the pressure in equation (4.9) to p^* is applied one has by construction:

$$\frac{\partial \ln p^*}{\partial\lambda} = \frac{\ln p^*_{i+1j} - \ln p^*_{i-1j}}{2\Delta\lambda} + o\left(\Delta\lambda^2\right) = \frac{1}{2\Delta\lambda}\int_{\lambda_{i-1}}^{\lambda_{i+1}}\frac{\partial \ln p^*}{\partial\lambda}\,\mathrm{d}\lambda' + o\left(\Delta\lambda^2\right) \tag{4.13}$$

Note that in (4.13) the vertical index j for the background pressure p^* has been omitted, because p^* is a local approximation essentially limited to the given horizontal coordinate surface. Substituting (4.12) into the RHS of equation (4.13) yields:

$$\frac{\ln p^*_{i+1j} - \ln p^*_{i-1j}}{2\Delta\lambda} = -\frac{1}{2\Delta\lambda}\int_{\lambda_{i-1}}^{\lambda_{i+1}}\frac{1}{RT^*}\frac{\partial\Phi}{\partial\lambda}\,\mathrm{d}\lambda' \tag{4.14}$$

That is, the discrete Archimedes buoyancy principle has been exploited to construct a discrete approximation to the RHS of equation (4.12). This approximation is achieved using the same discrete operator that has been applied to the pressure term in (4.9). It should be stressed again that the discrete operator structure is a key point in controlling the resulting LTE and thus in improving cancellation properties. The local stationary solution (T^*, p^*) is supposed to approximate the stationary component of the current model state (T, p) around the cell-center (λ_i, η_j). Since the local stationary components cancel exactly only the residual components have to be taken into account for the approximation of the PGF. A balance of two terms with similar magnitude but opposing signs is still retained. However, the residual components are much smaller in magnitude. The LTE scales with these magnitudes and so the vulnerability to errors discussed before is reduced. This approach is similar to the subtraction of constant background states from the thermodynamic variables before evaluating the PGF (e.g. Gary 1973). The main advantages of the technique applied here are the locality and time-adaptivity. The locality allows for more accurate approximations of the background states, because they do not have to be applicable to a whole vertical column. In this way, the available degrees of freedom can solely be used towards approximating the background states more precisely. The time-adaptivity refers to the fact that the local background states are approximated in each timestep based on the current model state. This allows applications in climate modeling with very long integration times.

So far (T^*, p^*) have only been required to solve the stationary state equation (4.8) or equivalently (4.12). Without constraining the local solutions appropriately they can not be expected to relate to the stationary components of the given model state. To this end, it is required that both the background pressure and temperature take the given point values of the model:

$$T^*_{ij} = T^*(\lambda_i, \eta_j) = T_{ij} \text{ and } p^*_{ij} = p^*(\lambda_i, \eta_j) = p_{ij} \tag{4.15}$$

In this way, the local approximations are guaranteed to be close to the true model state at least near the cell-center. Now all ingredients needed to construct an approximation to the PGF with improved cancellation properties are given. To that end, the difference between equations (4.9) and (4.13) is investigated. Defining

$$D^{ij}_{\lambda} = \frac{\ln p_{i+1j} - \ln p_{i-1j}}{2\Delta\lambda} - \frac{\ln p^*_{i+1j} - \ln p^*_{i-1j}}{2\Delta\lambda} \tag{4.16}$$

and applying (4.11) to both $\ln p$ and $\ln p^*$ yields:

$$D^{ij}_{\lambda} = \left(\frac{\partial \ln p}{\partial \lambda} - \frac{\partial \ln p^*}{\partial \lambda} \right)\bigg|_{ij} + \sum_{n=1}^{\infty} \frac{1}{(2n+1)\,!} \frac{\partial^{(2n+1)} (\ln p - \ln p^*)}{\partial \lambda^{(2n+1)}} (\Delta\lambda)^{2n} \tag{4.17}$$

Note that all terms are evaluated at the cell-center (λ_i, η_j). Exploiting both the stationarity of p^*, i.e., equation (4.12), and the constraints on the local approximation (4.15) this can be written:

$$D^{ij}_{\lambda} = \left(\frac{\partial \ln p}{\partial \lambda} + \frac{1}{RT} \frac{\partial \Phi}{\partial \lambda} \right)\bigg|_{ij} + \sum_{n=1}^{\infty} \frac{1}{(2n+1)\,!} \frac{\partial^{(2n+1)} \ln \frac{p}{p^*}}{\partial \lambda^{(2n+1)}} (\Delta\lambda)^{2n} \tag{4.18}$$

Firstly, equation (4.18) shows that D^{ij}_{λ} is a second-order accurate approximation to $\frac{\partial \ln p}{\partial \lambda} + \frac{1}{RT} \frac{\partial \Phi}{\partial \lambda}$ at the cell-center. Secondly, the individual summands of the LTE each scale with a derivative of $\ln \frac{p}{p^*}$. The closer the local background state p^* is to the true pressure p, the smaller these derivatives will be. The idea is that if the model state (p, T) is stationary then approximations (p^*, T^*) fulfilling (4.12) and (4.15) will generally be very accurate. Ideally, one would have $p = p^*$ and $T = T^*$ and the truncation error in equation (4.18) would vanish completely. However, in general the true model state can only be approximated based on the given local point values. More accurate approximations will lead to better cancellation properties. The question how to construct these approximations will be addressed in the next section. Before, equation (4.18) is used to finally give an approximation to the PGF in equation (4.8):

$$-\frac{1}{a\cos\varphi}\left(RT\frac{\partial \ln p}{\partial \lambda} + \frac{\partial \Phi}{\partial \lambda}\right)\bigg|_{ij} = -\frac{RT_{ij}}{a\cos\varphi_j} D_\lambda^{ij} + o\left(\Delta\lambda^2\right) \tag{4.19}$$

with D_λ^{ij} according to (4.16).

To sum up, with the help of a local stationary background state a discrete approximation (4.19) to the PGF that is second-order accurate can be constructed. Moreover, the remaining LTE can be decreased by improving the accuracy of these approximations potentially leading to greatly improved cancellation. The caveat is that it has so far not been specified how to actually reconstruct suitable background states (p^*, T^*) from given point values of p, T and Φ. This will be attempted in the next section.

4.2.1 Reconstructing the Local Background State

It has been seen in the preceding section that cancellation of the PGF can be improved if suitable approximations of a background equilibrium state (p^*, T^*) are acquired. Clearly, the stationary state equation (4.12) within the given cell needs to be solved. If the solution also respects (4.15), i.e., is linked to the local thermodynamic state of the model, the approximation (4.19) will retain the desired properties. In the example from section 4.1 the background states were reconstructed by solving an initial value problem for the separable ordinary differential equation (4.1). Aside from substituting a local density approximation the separability relied on the simple form of the vertical geopotential gradient $\frac{\partial \Phi}{\partial z} = g$. Applying the same principle here is difficult, because the stationary state equation in the η-system instead features the horizontal gradient of the geopotential. It is already known from the previous chapters that this gradient is in general not constant along surfaces of constant η. Moreover, since the model is hydrostatic it must respect a discrete version of (2.18). In REMO this is achieved by discrete integration of the hydrostatic equation based on the given values of p and T. Expanding the stationary state equation (4.12) with the definition of the geopotential in (2.19) yields:

$$\frac{\partial \ln p^*}{\partial \lambda} = -\frac{1}{RT^*}\left(\frac{\partial \Phi_s}{\partial \lambda} - R\frac{\partial}{\partial \lambda}\int_1^\eta T^* \frac{\partial \ln p^*}{\partial \eta}\,\mathrm{d}\eta'\right) \tag{4.20}$$

Equation (4.20) needs to be solved in order to reconstruct the local background states, but it is not separable even if suitable local approximation of the temperature are substituted. Instead, it is of the integro-differential type, i.e., it involves an integral of the unknown p^*. Additionally, the equation is a partial differential equation that features both horizontal and vertical derivatives. This severely complicates the solution and one can not expect to attain analytical solutions as in the introductory example. This complication is a result of both the pressure-based coordinate system and the hydrostatic nature of the model. For instance, a terrain-following coordinate based on geometric height would allow to compute the geopotential exactly in every level of the model. Integration of (2.18) would not be required anymore. However, if such a model was hydrostatic equation (2.18) would still have to be enforced in a different way. Consequently, such a model would have to attain the pressure values by integration of the hydrostatic equation instead. This would also result in an integro-differential equation similar to (4.20). The main culprit is therefore the enforced hydrostatic consistency of the model. However, a non-hydrostatic model with a height-based terrain-following coordinate may retain a simple form of the stationary state equation and lend itself more towards the approach presented here.

If analytical solutions of (4.20) are too difficult to attain the remaining option is to aim for approximate solutions instead. Note that to construct the approximation (4.19) only the values of p^* at the adjacent gridpoints (λ_{i-1}, η_j) and (λ_{i+1}, η_j) are required. The precise evolution of the background state between those need not be known. This can be exploited by integrating the stationary state equation (4.12) from the cell-center to these adjacent points and introducing a change of variables:

$$\ln p^*_{i+1j} = \ln p^*_{ij} - \int_{\lambda_i}^{\lambda_{i+1}} \frac{1}{RT^*} \frac{\partial \Phi}{\partial \lambda} \, \mathrm{d}\lambda' = \ln p^*_{ij} - \frac{g}{R} \int_{z_i}^{z_{i+1}} \frac{1}{T^*} \, \mathrm{dz}' \tag{4.21}$$

Applying the initial condition (4.15) for p^* and repeating the procedure for the other gridpoint one arrives at:

$$\begin{aligned} \ln p^*_{i+1j} &= \ln p_{ij} - \frac{g}{R} \int_{z_i}^{z_{i+1}} \frac{1}{T^*} \, \mathrm{dz}' \\ \ln p^*_{i-1j} &= \ln p_{ij} - \frac{g}{R} \int_{z_i}^{z_{i-1}} \frac{1}{T^*} \, \mathrm{dz}' \end{aligned} \tag{4.22}$$

The advantage of using equation (4.22) to compute the point values of p^* is that no assumptions about the geopotential gradient have to be made. This avoids most of the complications with equation (4.20) and gives an equation that can be integrated in a straightforward manner at least for simple local temperature approximations. On the other hand point values of the geometric height or equivalently the geopotential are still needed. These are required not only because they control the range of integration in (4.22), but also because T^* needs to be formulated as a function of z in this case. This emphasizes once more the relevance of the geometric height for the approach considered here. The only recourse is to estimate such values via the hydrostatic equation. Clearly, any errors made will be detrimental to the cancellation properties of the method but some improvement can still be expected.

In principle equations (4.22) and (4.19) can now be used to construct an approximation for the horizontal PGF. However, the point values of z and the local temperature approximation T^* must be specified to actually make use of (4.22). Also all of the developments so far rely on the assumption of a co-located grid structure. Before clarifying the computation of z and T^* the scheme will be adapted to the vertical and horizontal staggering of the REMO model in the following section.

4.2.2 Vertical and Horizontal Staggering

So far it has been assumed that the discrete variables of the model all reside at the same points in the computational grid. For the REMO model this does not actually hold. Instead, the variables are arranged on a grid that is both vertically and horizontally staggered (see Figure 2.3 and Figure 2.4). The approximations (4.22) and (4.19) do not depend on any specific vertical grid arrangement. That is, the vertical staggering can be neglected for now. It will only be relevant for computing the height values required to compute p^* with (4.22). On the other hand the horizontal staggering is very relevant, because the discrete form of the approximation (4.19) depends explicitly on the horizontal grid structure. In REMO the u-points are located halfway between the points at which the temperature and pressure are defined. Since the PGF appears in the momentum equation it must also be defined at u-points. Ideally, one would like to use an adapted form of (4.19)

$$D_\lambda^{i+\frac{1}{2}} = \frac{\ln p_{i+1j} - \ln p_{ij}}{\Delta\lambda} - \frac{\ln p^*_{i+1j} - \ln p^*_{ij}}{\Delta\lambda} \tag{4.23}$$

to construct the approximation. Note that this in accordance with the definitions of the horizontal difference operators in equation (2.25). That means $D_\lambda^{i+\frac{1}{2}}$ is located at the point $\left(\lambda_{i+\frac{1}{2}}, \eta_j\right)$, i.e., the u-point between the adjacent cell-centers.

It has however been stressed that the local approximations (p^*, T^*) must be linked to the thermodynamic state of the model via equation (4.15). In the co-located setting this simply meant that the approximations interpolate (p, T) in the cell-center. However, due to the horizontal staggering the approximation is now defined at the u-point between the adjacent mass-points, i.e., at a cell boundary. The values of T and p at these points are unknown. They can only be estimated based on the given point values in the vicinity. The problem is that doing so would introduce additional truncation error into equation (4.18), namely in the first term. In light of this it appears more fruitful to first use equations (4.16) and (4.19) to compute balanced approximations at the adjacent mass-points (λ_i, η_j) and (λ_{i+1}, η_j). These approximations can then be averaged to construct a balanced approximation at the respective u-point, i.e.,

$$-\frac{1}{a\cos\varphi}\left(RT\frac{\partial\ln p}{\partial\lambda}+\frac{\partial\Phi}{\partial\lambda}\right)=-\frac{R}{2a\cos\varphi_j}\left(T_{ij}D_\lambda^{ij}+T_{i+1j}D_\lambda^{i+1j}\right)+o\left(\Delta\lambda^2\right) \tag{4.24}$$

D_λ^{ij} will be referred to as the left hand and D_λ^{i+1j} as the right hand approximation.

The remaining questions then are how to define the local temperature approximation T^* and the height values required for an evaluation of (4.22), (4.16) and finally (4.24). For the temperature two alternatives are formulated based on the assumption of either a constant or piecewise linear temperature distribution across the cell

$$T^* = T_{ij} \tag{4.25}$$

$$T^* = \begin{cases} T_{ij} + G^{i+1}\left(z - z_i\right), & \text{for } z \text{ between } z_i \text{ and } z_{i+1} \\ T_{ij} + G^{i-1}\left(z - z_i\right), & \text{for } z \text{ between } z_i \text{ and } z_{i-1} \end{cases} \tag{4.26}$$

where G^{i+1} and G^{i-1} are given by:

$$G^{i+1} = \frac{T_{i+1j} - T_{ij}}{z_{i+1} - z_i} \tag{4.27}$$

$$G^{i-1} = \frac{T_{i-1j} - T_{ij}}{z_{i-1} - z_i} \tag{4.28}$$

Note that (4.25) and (4.26) are the approximations used around the cell-center (λ_i, η_j) for use with the left hand approximation D_λ^{ij}. For the right hand approximation D_λ^{i+1j} around (λ_{i+1}, η_j) they have to be modified in the obvious way. Especially a linear distribution appears as a plausible choice given that the temperature is often assumed to be linear in z, e.g., when applying height corrections in the analysis of ensemble predictions. The standard atmosphere also works with piecewise constant or linear distributions. Note that both formulations are consistent with the constraints specified in equation (4.15) in the sense that z_i corresponds to λ_i and so on. Moreover, T^* has been given as a function of z as required by (4.22). Having specified the local temperature approximation one can continue by analytically evaluating the integrals in equation (4.22). For the constant temperature case this yields:

$$\begin{aligned} \ln p^*_{i+1j} &= \ln p_{ij} - \frac{g}{RT^*}\left(z_{i+1} - z_i\right) \\ \ln p^*_{i-1j} &= \ln p_{ij} - \frac{g}{RT^*}\left(z_{i-1} - z_i\right) \end{aligned} \tag{4.29}$$

This representation has to be modified analogously for the right hand approximation D_λ^{i+1j}. In case of the piecewise linear temperature distribution the result is

$$\begin{aligned} \ln p^*_{i+1j} &= \ln p_{ij} - \frac{g}{RG^{i+1}}\ln\frac{T_{ij} + G^{i+1}\left(z_{i+1} - z_i\right)}{T_{ij}} \\ \ln p^*_{i-1j} &= \ln p_{ij} - \frac{g}{RG^{i-1}}\ln\frac{T_{ij} + G^{i-1}\left(z_{i-1} - z_i\right)}{T_{ij}} \end{aligned} \tag{4.30}$$

Finally, the height values used in (4.30) have to be estimated to complete the scheme. The improved cancellation properties of the method will crucially depend on both: the accuracy of the local temperature approximation T^* and the estimated height values. Finding suitable approximations of the geometrical height is much more difficult, because the hydrostatic equation has to be integrated from the surface up to the given layer η_j. In this way, more and more vertical discretization error is introduced into the estimation as one progresses towards the top of the atmosphere. Consequently, the method is expected to yield better results towards the surface layer. Recall from (2.19) that one can write

$$\Phi = \Phi_s - R \int_1^\eta T \frac{\partial \ln p}{\partial \eta} \, \mathrm{d}\eta' \tag{4.31}$$

and that exact values of the surface geopotential Φ_s at the mass-points are given. The main question is then how to approximate the integral in (4.31). Once again one can avoid making assumptions about the gradient by introducing a change of variables:

$$z = z_s - \frac{R}{g} \int_{\ln p_s}^{\ln p} T \, \mathrm{d}\ln p' \tag{4.32}$$

The point values of the pressure in (4.32) are given, but the vertical temperature distribution has to be estimated to make use of (4.32). It appears sensible to use approximations that are consistent with the ones used before, i.e., either piecewise constant or piecewise linear ones. For the evaluation of the integral a common quadrature rule will be used, known as the Simpson rule. For low order polynomials this rule gives the exact integral and it can be used without additional loss of accuracy. According to the Simpson rule one can write the integral of a constant or linear function f as:

$$\int_a^b f \, \mathrm{d}\ln p' = \frac{b-a}{2} \left(f(a) + f(b) \right) \tag{4.33}$$

Clearly, for a constant function it is $f(a) = f(b)$. This rule can now be applied to approximate the geometrical height up to any given layer. Due to the staggered vertical grid a temperature at the surface is not given, but only at the full layers above (see Figure 2.4). Therefore, a constant temperature between the surface and the lowest full layer is assumed. The estimated height in the lowest full layer k_m can then be given as:

$$z_{ik_m} = z_{si} - \frac{R \left(\ln p_{ik_m} - \ln p_{si} \right)}{g} T_{ik_m} \tag{4.34}$$

For any of the remaining layers j with $1 \leq j < k_m$ above one has for the piecewise constant vertical temperature distribution:

$$z_{ij} = z_{ij-1} - \frac{R \left(\ln p_{ij} - \ln p_{ij-1} \right)}{g} T_{ij} \tag{4.35}$$

Assuming a piecewise linear temperature distribution instead yields:

$$z_{ij} = z_{ij-1} - \frac{R \left(\ln p_{ij} - \ln p_{ij-1} \right)}{2g} \left(T_{ij} + T_{ij-1} \right) \tag{4.36}$$

Now all the prerequisites to approximate the PGF according to (4.24) are assembled. However, there is a caveat. As can be seen from the definition of G^{i+1} and G^{i-1} in equations (4.27) and (4.28) the local approximation T^* becomes singular if $z_i = z_{i+1}$ or $z_i = z_{i-1}$. This is a consequence of transforming the integral in equation (4.21) into z-space, which is essentially predicated on the assumption of a one-to-one relationship between longitude λ and height z. The result is that the two sampling points for the linear approximation coincide prohibiting the use of a linear interpolation. In such cases the constant temperature distribution will instead be used which poses no such problems.

Now the procedural approach to computing the approximation in the form of pseudo code can be given. First, the algorithm based on constant horizontal and vertical temperature approximations is given, see Algorithm 1.

For the alternative of linear temperature approximations one instead has Algorithm 2. Here ϵ is a threshold for receding to the constant temperature approximation if the adjacent points are too close in terms of geometric height. Technically, this is only required if there is no change in height between the points at all, but due to the limited precision of floating point calculations a threshold close to zero has to be used. Both algorithms will be tested and compared to the standard scheme in REMO in the next chapter.

4.2.3 The Isothermal Equilibrium

It has already been shown that the cancellation properties of the scheme largely rest on the accuracy of both the local temperature and height approximations. Clearly, for most cases it will not be possible to deliver perfectly well-balanced approximations due to the limitations of these approximations. For the most simple stationary state, i.e., an isothermal equilibrium, one can however show that both schemes given here will exactly retain such states. An isothermal equilibrium is characterized by a constant atmospheric temperature. To this end, the height approximations, i.e., equations (4.35) and (4.36) are investigated. The initial values given by the surface height are known exactly beforehand, as are the pressure values controlling the range of integration. The only source of error in these equations is thus the assumed temperature distribution. However, in an isothermal state the temperature is simply equal to a constant reference temperature. Hence, both the piecewise constant and linear approximations will yield exact height values. This removes the most prominent source of error from the approximation.

The second source of error is the assumption about the horizontal distribution of the temperature for computing the pressure p^* in (4.29) or (4.30). Both the constant and linear assumption will obviously lead to the true temperature distribution across the cell for the isothermal state. The integrals have been evaluated analytically, hence no error can be introduced in this way either. Locally, one then has $p^* = p$ and from equation (4.18) it can be seen that the discretization error for both the left and right hand approximations D_λ^{ij} and D_λ^{i+1j} will vanish completely. As a result, the averaged approximation (4.24) will also vanish. This shows that the isothermal equilibrium will be retained by the schemes given here.

Algorithm 1 PGFCONS

```
for all i do
    for all j do
        Compute $z_{ij}$ according to (4.35)
for all i do
    for all j do
        Compute $p^*$ according to (4.29)
        Use $p^*$ to compute $D^{ij}$ and $D^{i+1j}$ with (4.16)
        Approximate PGF using (4.24)
```

Algorithm 2 PGFLIN

```
for all i do
    for all j do
        Compute $z_{ij}$ according to (4.36)
for all i do
    for all j do
        if $|z_{ij} - z_{i+1j}| \leq \epsilon$ then
            Compute $p^*$ according to (4.29)
        else
            Compute $p^*$ according to (4.30)
        Use $p^*$ to compute $D^{ij}$ and $D^{i+1j}$ with (4.16)
        Approximate PGF using (4.24)
```

5 Validation in Idealized Test Cases

In this chapter numerical examples of the scheme developed in the previous chapter are presented demonstrating its capacity to reduce the pressure gradient error in idealized scenarios. To this end, a 2D vertical-plane version of the REMO model is initialized with different stationary states and the generation of spurious momentum in the vicinity of steep orographic gradients is investigated.

5.1 The Isothermal Atmosphere

In this section the most simple example of a stationary state, namely the isothermal equilibrium is examined. This state is characterized by a vertically and horizontally constant reference temperature. As pointed out in subsection 4.2.3 the new scheme is expected to retain such an equilibrium due to theoretical argument. However, due to the finite precision of floating point computations the error can in general not exactly equal zero. Ideally, a well-balanced scheme produces errors close to the system dependent roundoff error ϵ_m, often referred to as machine epsilon. All computations in this chapter were carried out on a 64-bit architecture in double precision with the GNU FORTRAN compiler. In this framework one has the estimation $\epsilon_m \approx 2.22 \times 10^{-16}$. Note that errors of this magnitude can be considered to be numerically zero, i.e., are not inherent to the numerical scheme but merely a consequence of machine limitations. However, depending on the sensitivity of a scheme to roundoff errors, which is closely linked to the number of floating point operations expended, larger errors may accrue over time.

5.1.1 Computational Domain and Orography

A domain of 1° longitudinal extent around the prime meridian and located on the equatorial great circle is considered. This equates to a domain width of approximately 111 km. Two different orographies are tested, both characterized by a domain-centered mountain of $z_m = 2.5\,\mathrm{km}$ maximum height. The first one is a bell shaped mountain given in parameterized form as:

$$f_b(\lambda) = z_m \exp\left(-\frac{\lambda^2}{2r_b}\right) \tag{5.1}$$

with the shape parameter $r_b = 0.001$.

The second orography is substantially more complex and given by a Schär-type mountain (see Schär et al. 2002) in parameterized form

$$f_s(\lambda) = h_0 \cos^2\left(\frac{\pi\lambda}{r_f}\right) \tag{5.2}$$

with

$$h_0(\lambda) = \begin{cases} z_m \cos^2\left(\frac{\pi\lambda}{2r_a}\right) & |\lambda| < r_a \\ 0 & \text{otherwise} \end{cases} \tag{5.3}$$

where the shape parameters are given by $r_f = 0.1$ and $r_a = 0.25$. Figure 5.1 shows a

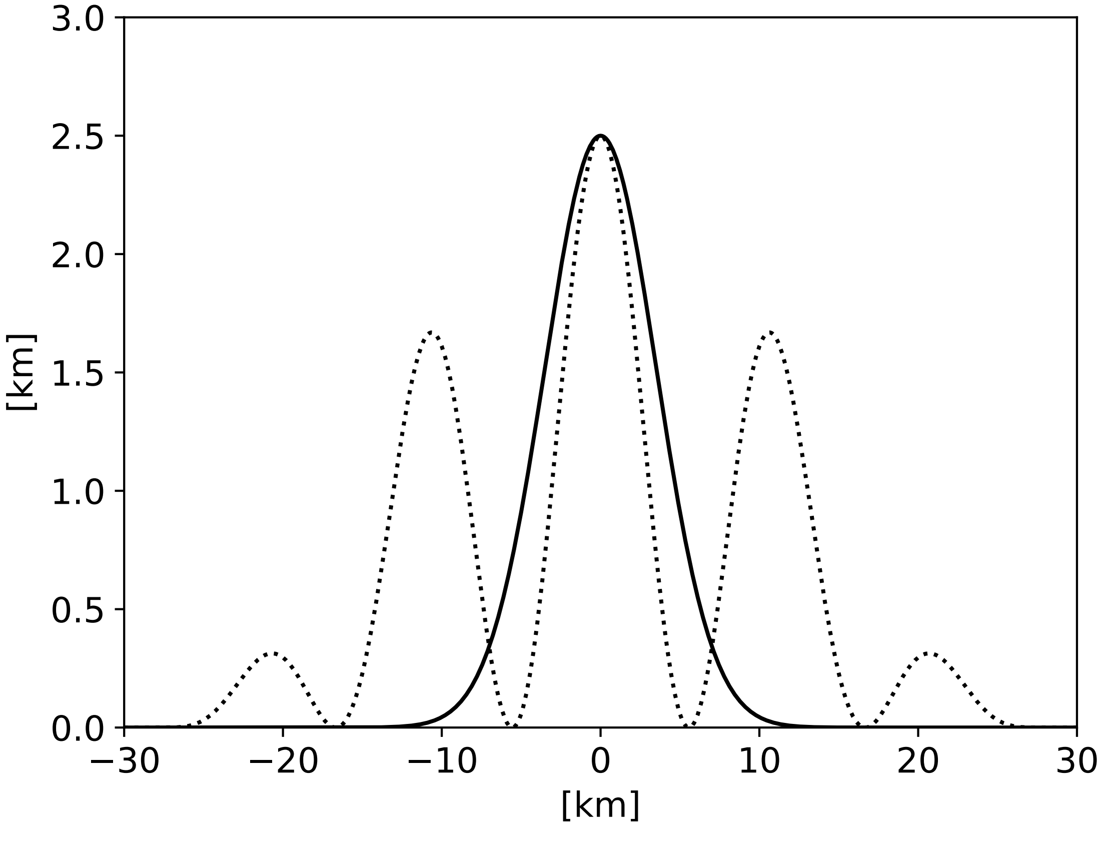

Figure 5.1: *Test case orography: bell shaped mountain (solid) and Schär-type mountain (dotted).*

plot of the two test orographies. The tests for the bell-shaped mountain are conducted at two different resolutions both horizontally and vertically. For the former resolutions of 0.1° and 0.01° are investigated corresponding to about 10 km and 1 km respectively. For a hydrostatic model these resolutions are relatively high given that the hydrostatic assumption becomes questionable when the ratio of horizontal and vertical scales approaches one (e.g., Orlanski 1981; Daley 1988). However, these tests merely serve to assess the ability of the discretization to retain equilibrium states. To that end, the physical validity of the hydrostatic approximation is of little importance. It is more important to capture the orographic features with sufficient accuracy especially for the Schär-type mountain. Therefore, the Schär-test is only conducted at the higher horizontal but both vertical resolutions.

For the vertical resolution two options commonly used in operational applications of the REMO model are investigated. The actual vertical resolution in meters is highly inhomogeneous along a given vertical column and depends on both the chosen vertical coordinate parameters and the surface pressure, i.e., is time-dependent. Therefore, the vertical resolutions are characterized by the total number of vertical levels used. For classical hydrostatic applications REMO is generally run with 27 levels. For computations with the non-hydrostatic model version REMO-nh 40 levels are used to allow for an improved resolution. The appendix contains a detailed list of the corresponding vertical coordinate parameters A and B for both vertical resolutions. Figure 5.2 shows the level distributions for both test orographies at the higher vertical and horizontal resolutions. The typical structure emerges with orography-dominated levels near the ground slowly tending towards flat pressure levels in the upper atmosphere. Above approximately 18 km the levels have become completely isobaric.

5.1.2 Initial and Boundary Values

To assess the ability of the new discretization to retain an isothermal state the model must be initialized with suitable initial and boundary data. Note that an isothermal state is equivalent to the equilibrium derived in section 3.3 when a vanishing lapse rate is assumed. A mean sea level reference pressure of $p_{ref} = 1013.25\,\text{hPa}$ and an atmosphere wide reference temperature $T_{ref} = 288.15\,^{\circ}\text{K}$ is prescribed. Equation (3.23) is used together with the known surface height to find the matching surface pressure. Equation (2.39) then yields the pressure for each column and the temperature values of the model are all set to T_{ref}. The equilibrium is also initialized into the two boundary lines used in the REMO model to avoid perturbations entering the domain from outside. Boundary assimilation has been switched off for all computations in this chapter. This concludes the initialization procedure. The model is then run for a total of one hour to investigate the development and growth of spurious motion during this time.

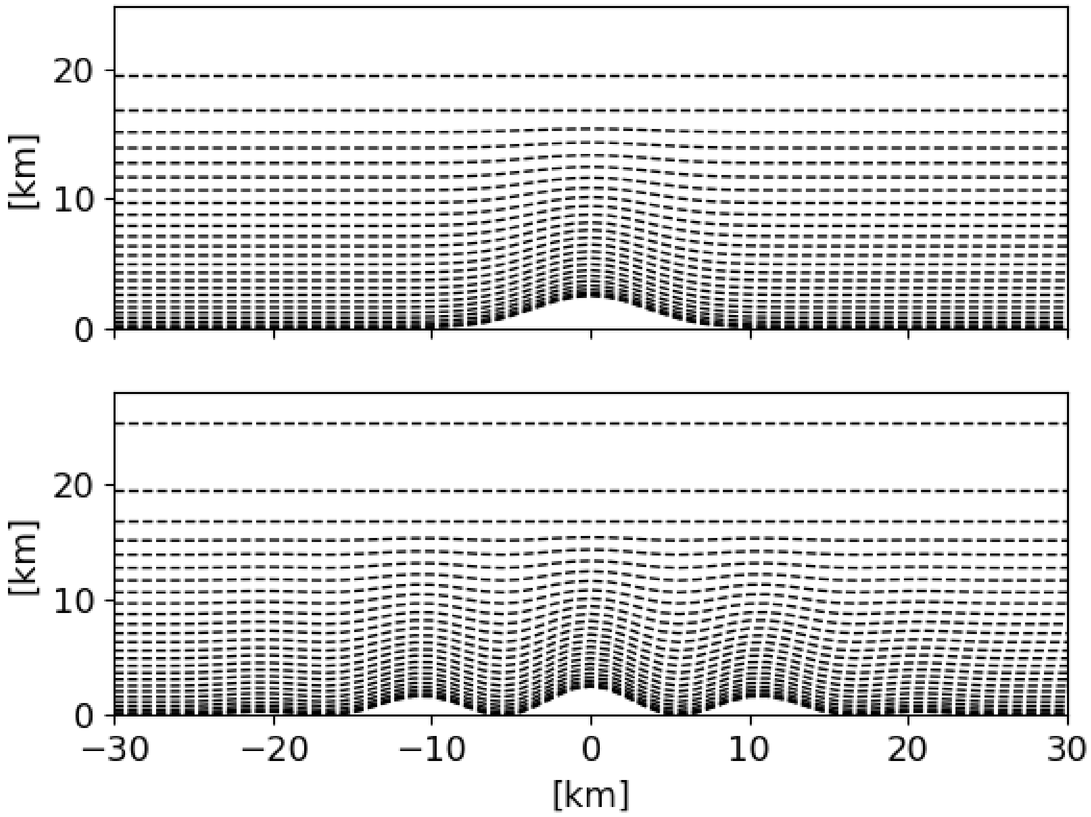

Figure 5.2: *Vertical level distributions for the isothermal test case with* 40 *levels and* 1 km *horizontal resolution.*

5.1.3 Results

In this section the results for the isothermal test case are evaluated and both the spatial structure of the resultant PGE as well as its evolution over time are investigated.

Spatial Error Structure

The most straightforward performance measure is the absolute value of u-wind speed at any given time $t > 0$. Note that the analytic solution gives $u = 0$ at all times and therefore the magnitude of deviations from this value is a sensible measure of error.

Non-zero windspeed in the given test environment should accrue exclusively due to errors in the PGF and hence represents the combined detrimental effect over the course of a simulation. Inspecting PGF errors directly on the other hand is merely a measure of how much additional spurious acceleration is created at that point in time.

Figure 5.3 shows the u-error at the final time of computation $t = 3600\,\mathrm{s}$ for the classic PGF discretization. First note that the orography for the lower horizontal resolution (left hand side) appears to be much flatter than for the high resolution (right hand side). This is solely due to graphical limitations where the computational cells are drawn as quadrilaterals with vertices at cell interfaces. Intra-cell variation of orography is not taken into account. Due to the low amount of sampling points at 10 km resolution this gives the impression of a lower overall mountain height. However, in the initial data the mountain is actually sampled at $z_m = 2.5\,\mathrm{km}$ among other points. The results immediately suggest a strong dependency on both the chosen vertical and horizontal resolution. For all but one case (upper right) the highest errors are found in the stratosphere above 15 km. Increasing the vertical resolution while keeping the horizontal resolution fixed strongly reduces the errors. As expected the lowest error is observed with a combination of high vertical and horizontal resolution (lower right) with values between -0.05 and $0.05\,\mathrm{m\,s^{-1}}$. For lower resolutions spurious motion can reach more than $\pm 0.15\,\mathrm{m\,s^{-1}}$ which is quite substantial given the short simulation time. Somewhat peculiar is the result for high horizontal and low vertical resolution as shown in the upper right. The error is most prominent in the upper troposphere and shows indications of a computational mode. It can be conjectured that this is a result of mismatched resolutions which would indicate that the PGE can have detrimental effects on stability as well at least if resolutions are not chosen carefully. Interestingly, the opposite combination of low horizontal but high vertical resolution (lower left) does not appear to suffer from any such issues. Instead the structure of the error is virtually the same as in the low resolution case above albeit with much lower magnitudes. The importance of the geopotential approximation in computing the PGF has already been pointed out. That approximation is built from adding up discrete vertical derivatives whose accuracy depends mostly on the vertical resolution. Therefore, these results may give credence to the notion that vertical resolution is overall more important for reducing the PGE and that the geopotential approximation may be at least as relevant to the problem as the choice of coordinate system.

Next the results for the newly developed scheme are investigated. Recall that in chapter 4 two algorithms PGFCONST and PGFLIN have been given that differ only in the kind of approximations (piecewise constant or linear) used to reconstruct the local hydrostatic background states. Figure 5.4 shows the results for the PGFCONST scheme. Clearly, the new scheme produces substantially reduced errors in all cases with typical magnitudes between -1×10^{-11} and $1 \times 10^{-11}\,\mathrm{m\,s^{-1}}$, i.e., several orders of magnitude smaller than the classic discretization. This is rather close to round-off error but the deviation from the theoretical predictions in subsection 4.2.3 is apparent. The scheme does not appear to produce fully well-balanced results even for this simple test case. Possible reasons for this discrepancy will be addressed later in this section. However, a qualitative examination

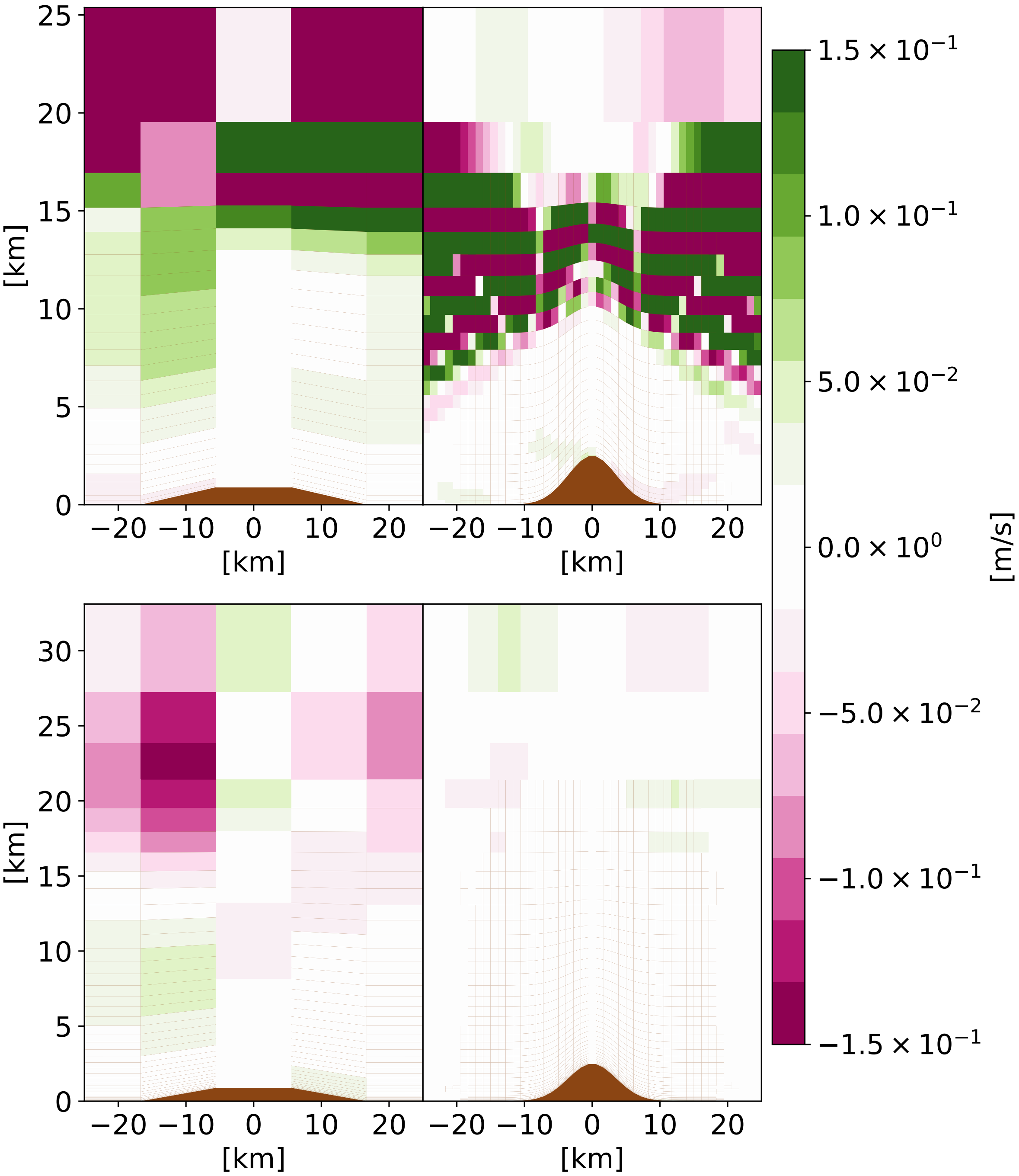

Figure 5.3: *u-error at final time $t = 3600\,\mathrm{s}$ for the classic scheme and the bell-shaped mountain. Shown are the results for 27 and 40 levels (top to bottom) and 10 km as well as 1 km (left to right) respectively. Orography is shown in brown.*

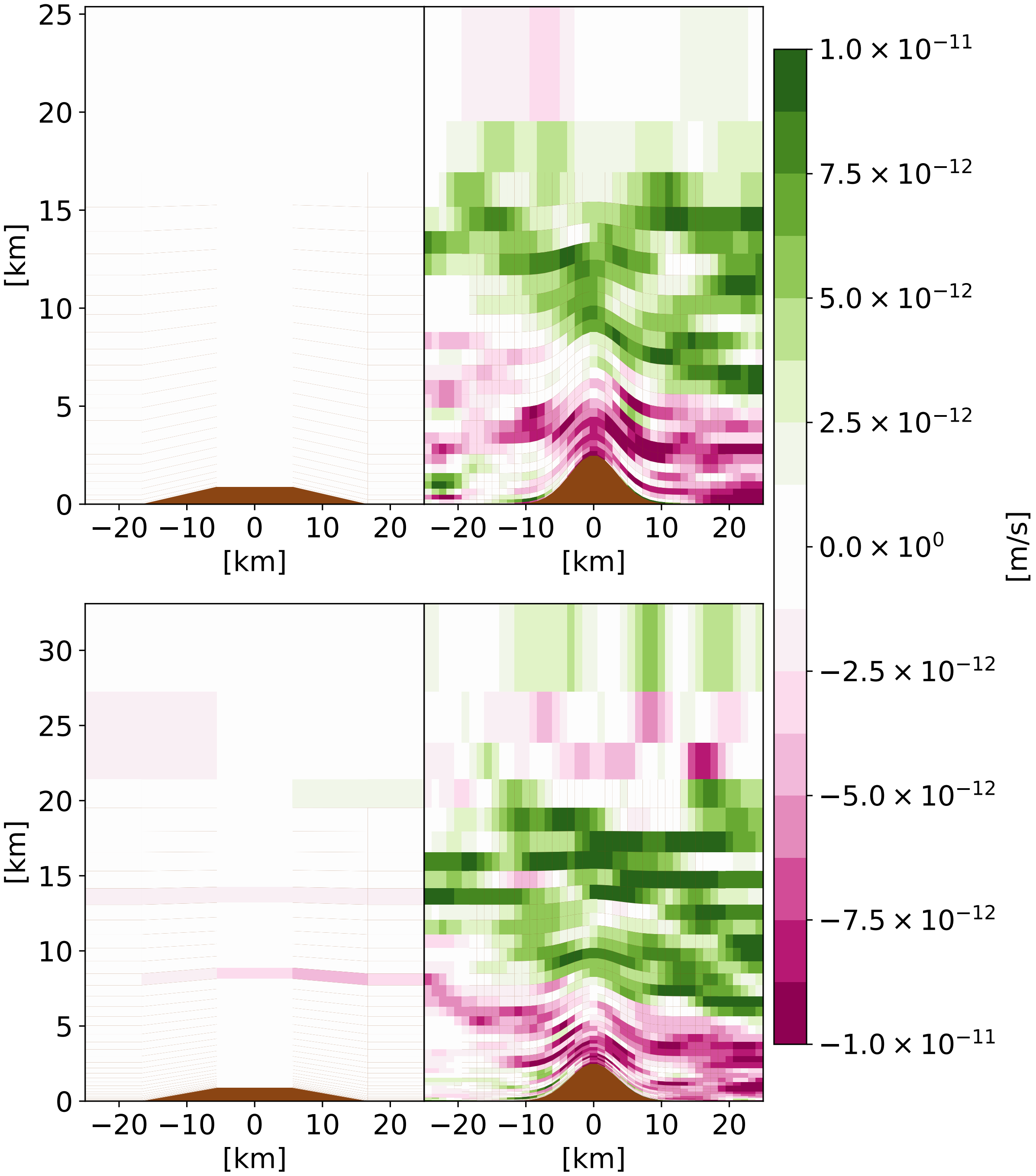

Figure 5.4: *u-error at final time t = 3600 s for the PGFCONST scheme and the bell-shaped mountain. Shown are the results for 27 and 40 levels (top to bottom) and 10 km as well as 1 km (left to right) respectively. Orography is shown in brown.*

of these results may already give rise to a possible explanation. In stark contrast to the results for the classic scheme the error appears to increase with improved resolution both horizontally and vertically. No sign of a computational mode can be identified, but clearly higher resolutions tend to produce higher magnitudes of error and appear more noisy. As mentioned before even a perfectly well-balanced method will generally produce non-zero error due to the finite precision of floating point operations. Often the results will oscillate around zero with magnitudes ideally in the range of machine epsilon. However, the error is related to the number of floating point operations expended in the scheme because each operation will cause additional round-off. The computation of the geopotential requires additional operations for each additional vertical level. Possibly, this may in part explain the observed tendency to produce larger errors with increased resolution. Another interesting observation is that the new scheme seems to produce the largest errors close to the ground and in the troposphere in contrast to the classic one. Overall the error seems to be a bit more evenly distributed.

Figure 5.5 shows the results for the PGFLIN scheme. The structure of the error appears to be virtually if not exactly the same as that in Figure 5.4, i.e., there is no benefit of using a linear over a constant approximation for the given test case. This is rather easily explained because of the isothermal equilibrium. The local constant or linear temperature approximations used in constructing background states naturally give the same results for a temperature constant among cells as in the isothermal example.

Figure 5.6 shows the results for the Schaer-type mountain. The classic scheme produces errors comparable in magnitude to the ones from the bell-shaped mountain in Figure 5.3. The increased complexity of the orography does not appear to have any direct effect in this regard. However, the results for the lower vertical resolution are somewhat reminiscent of the possible computational mode encountered before albeit less pronounced. Possibly, the more complex terrain in this example requires the highest vertical and horizontal resolution to be adequately resolved. In that case (right hand side) the error is greatly reduced and remarkably similar to the one observed for the bell-shaped mountain. The results for the PGFCONST and PGFLIN schemes are also quite similar to those in Figure 5.4 and Figure 5.5. Note that the schemes seem to handle even the lower resolution without any indication of numerical issues. The magnitudes and spatial structure of the errors also are consistent with the results for the bell-shaped mountain. At least for the given test case the new schemes appear to be independent of the orographic complexity as conjectured in subsection 4.2.3.

To gain more insight into the representation of the PGF the PGE is now investigated directly. As mentioned the PGE is a measure of how fast new spurious momentum is produced at a given time. Figure 5.7 shows the PGE results for the bell-shaped mountain and the classic discretization at the initial time of the simulation. As expected the highest errors are found in the upper atmosphere with values in the range of $\pm 1 \times 10^{-2}\,\mathrm{m\,s^{-2}}$. The results show a spatial structure with four distinct regions of errors centered above the mountain and arranged in a symmetrical pattern. Most likely this is due to the

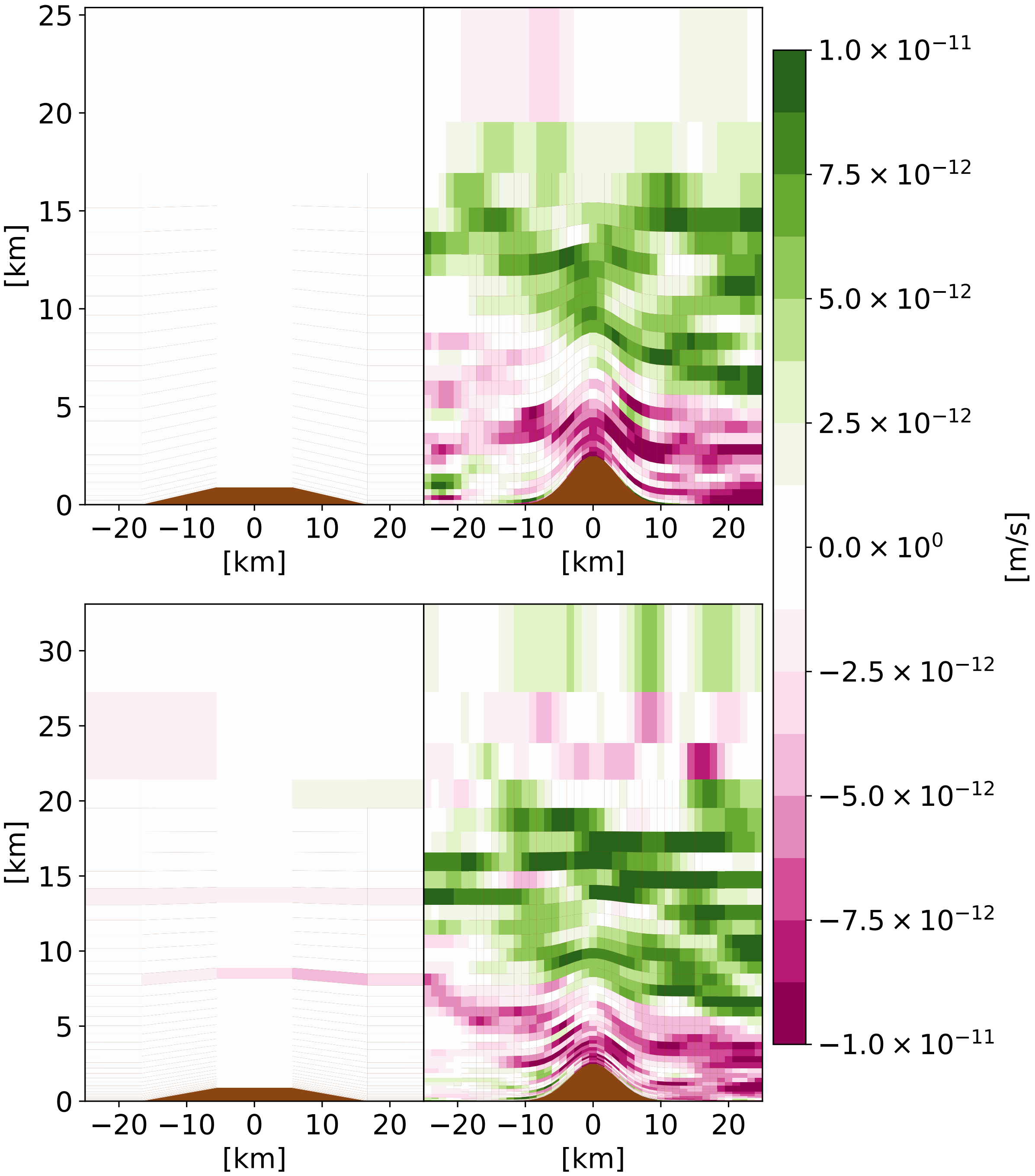

Figure 5.5: *u-error at final time $t = 3600\,\mathrm{s}$ for the PGFLIN scheme and the bell-shaped mountain. Shown are the results for 27 and 40 levels (top to bottom) and 10 km as well as 1 km (left to right) respectively. Orography is shown in brown.*

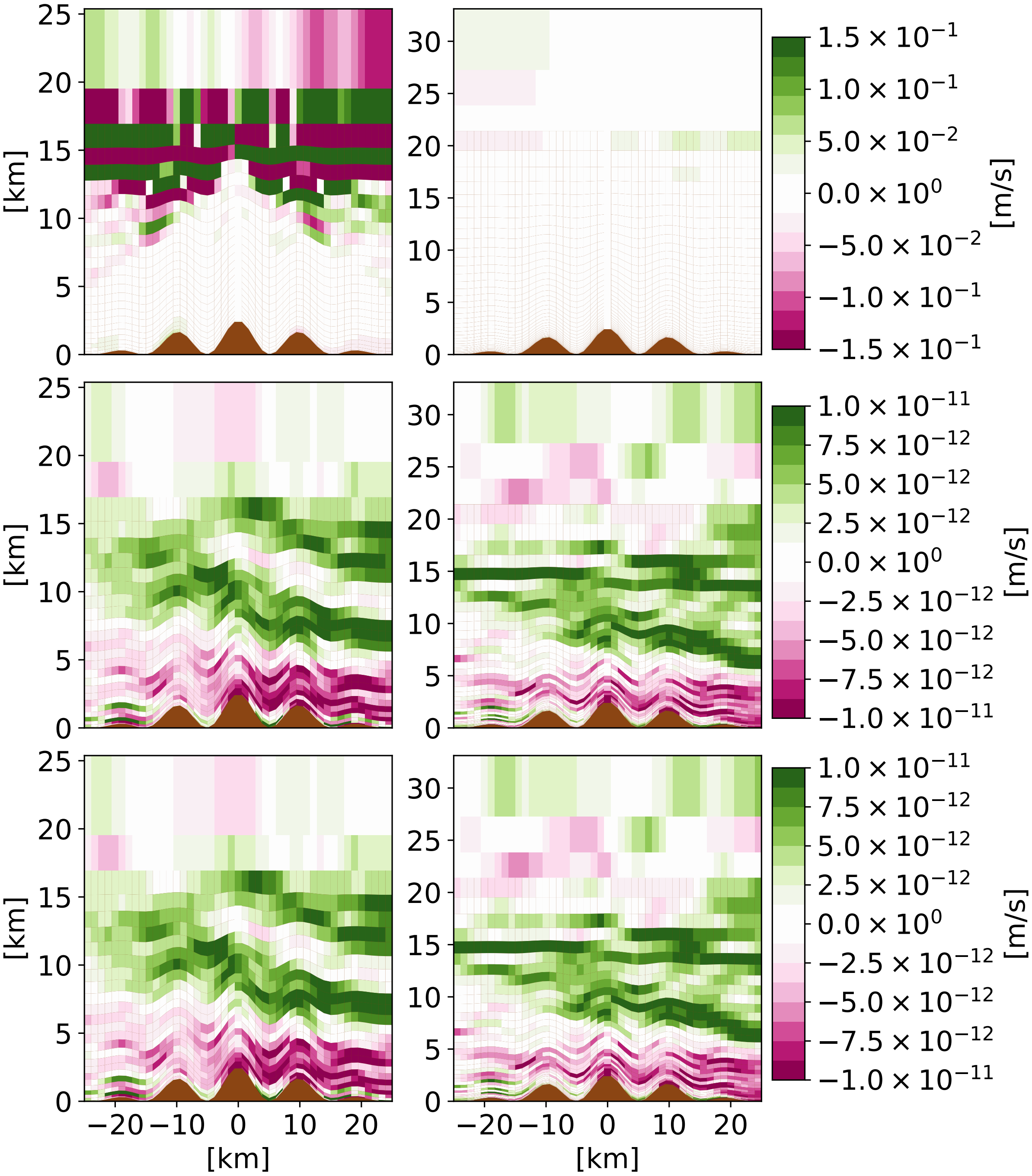

Figure 5.6: *u-error at final time $t = 3600\,\mathrm{s}$ for the Schär-type mountain. Shown are the results for 27 and 40 levels (left to right) and for the classic, the PGFCONST and PGFLIN schemes (top to bottom).*

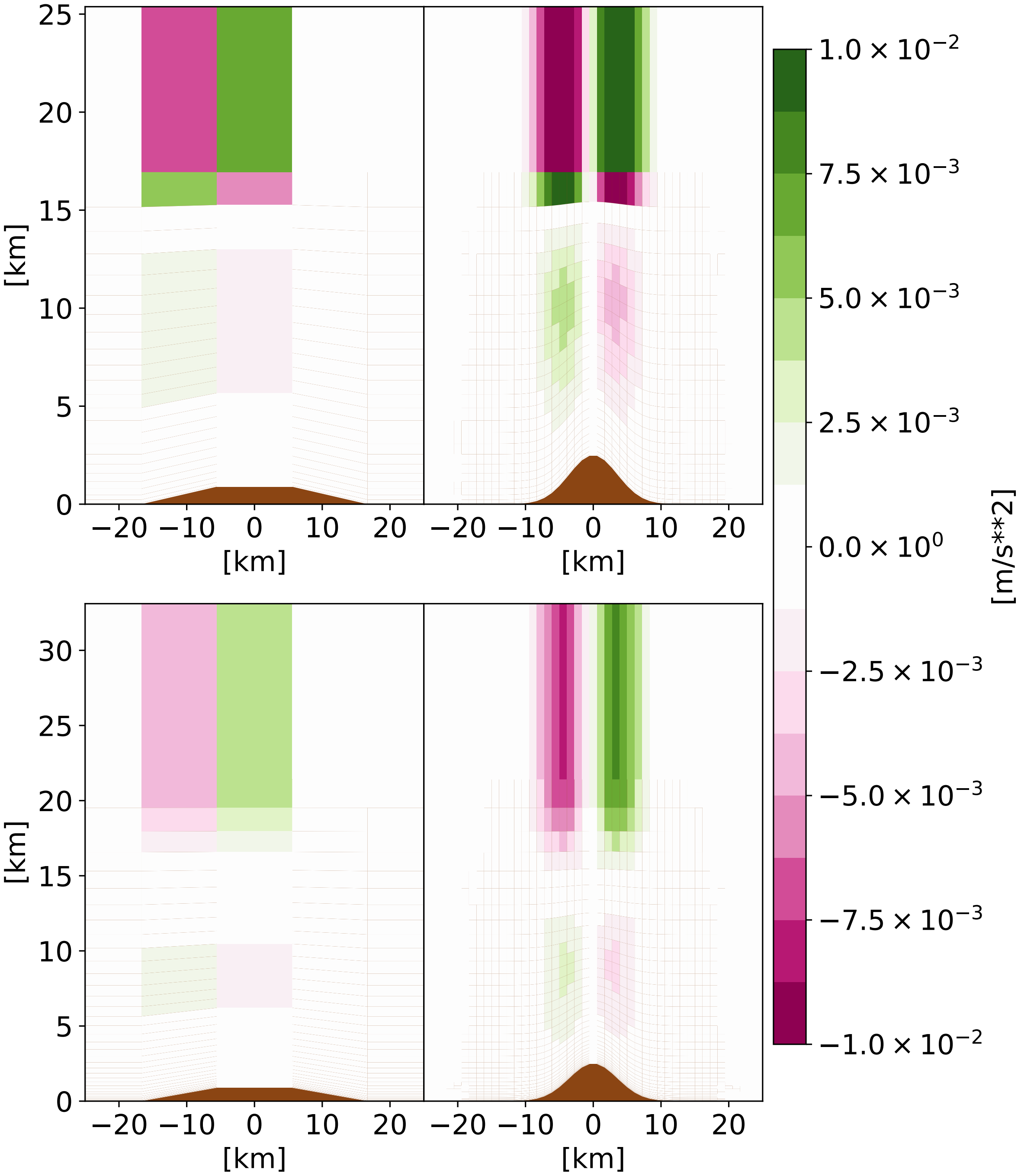

Figure 5.7: *Pressure gradient error at initial time* $t = 0\,\mathrm{s}$ *for the classic scheme and the bell-shaped mountain. Shown are the results for 27 and 40 levels (top to bottom) and* 10 km *as well as* 1 km *(left to right) respectively. Orography is shown in brown.*

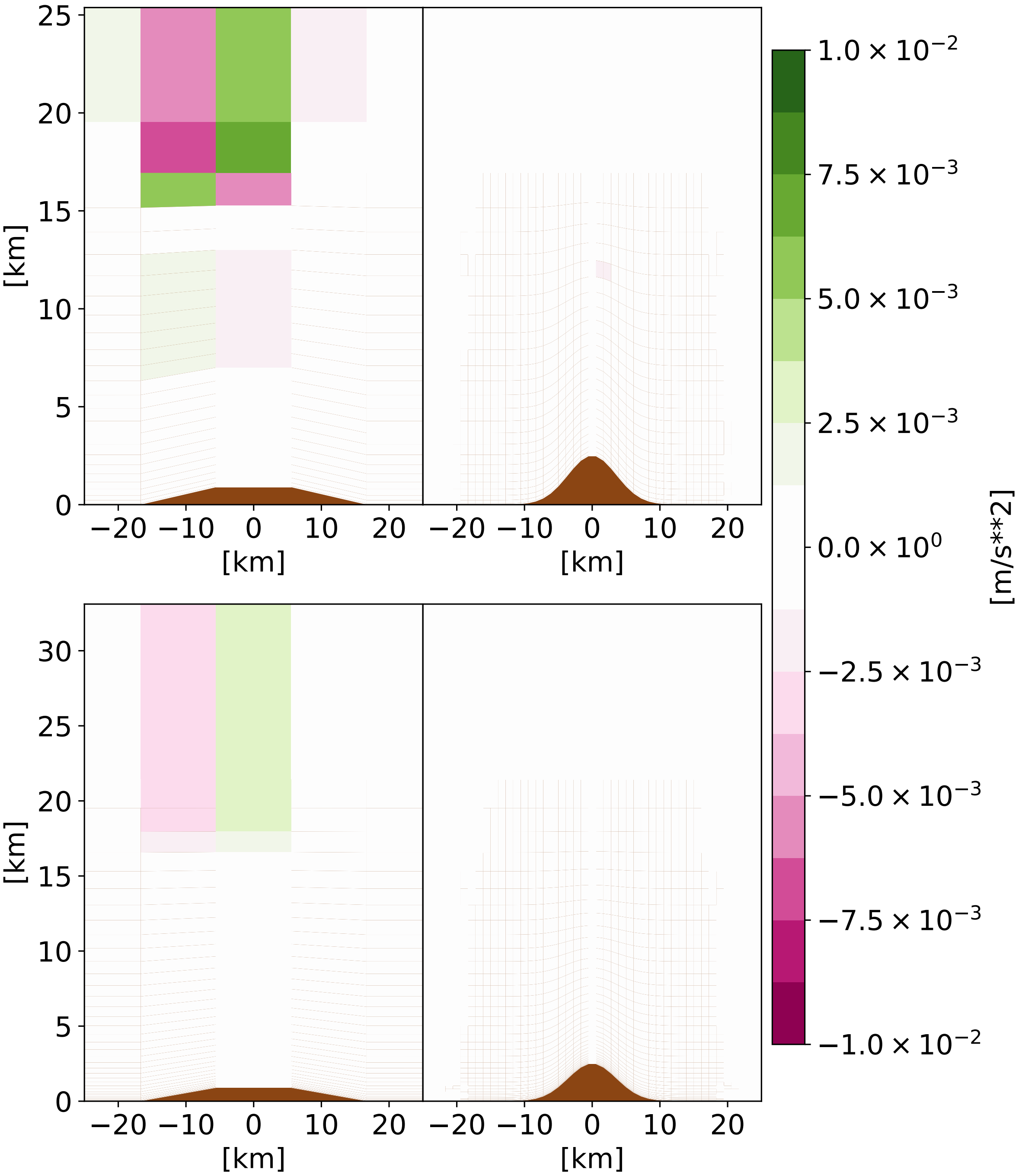

Figure 5.8: *Pressure gradient error at final time* $t = 3600\,\mathrm{s}$ *for the classic scheme and the bell-shaped mountain. Shown are the results for 27 and 40 levels (top to bottom) and* 10 km *as well as* 1 km *(left to right) respectively. Orography is shown in brown.*

symmetry of the bell-shaped mountain and the change of sign of the inclination along the mountain top. All resolutions show qualitatively similar results. It appears that increasing the vertical resolution (from top to bottom) is more effective in reducing the error than increasing the horizontal resolution (from left to right). Figure 5.8 shows the same plot but for the final time of the simulation. Interestingly, the left hand side (low horizontal resolution) shows a similar picture compared to the initial time. However, the magnitude of error has clearly reduced significantly. The right hand side shows that for the higher resolutions the error is greatly reduced after 1 h of simulation. The results suggest that the initial PGE slowly reduces over time leading into a perturbed steady-state at which little or no further momentum is produced.

Figure 5.9 shows the PGE for the PGFCONST scheme at the initial time. The scheme produces greatly reduced errors very close to round-off error. As observed with the u-error previously higher resolutions exhibit larger errors. The spatial structure is completely different from the classic scheme with a more evenly distributed error but a more noisy appearance. Figure 5.10 shows the PGE for the final time of simulation. Unlike the classic scheme the picture has hardly changed over time. Both the magnitude and structure of errors are very similar compared to the initial time. This suggests once more that these errors are related to round-off errors and in that sense are not inherent to the scheme itself.

Time Evolution

Previously the spatial structure of the mountain-induced circulation has been investigated for both the classic and the new schemes. Another interesting question is how the error evolves over the course of the simulation. Figure 5.11 shows the growth of the domain-wide maximum absolute (top) and mean (bottom) u-error over the duration of the experiment. Note that the error curves are plotted on a logarithmic y-axis to allow for direct comparison of the classic and the new discretization in one plot. The results of the PGFLIN scheme have been omitted as they have been previously seen to be virtually identical to those of the PGFCONST scheme. The new scheme produces substantially smaller maximum errors over the duration of the simulation as expected. Both schemes appear to produce the bulk of the spurious motion immideately after initialization and then tend to stagnate and settle into the attained speed. This is consistent with the PGE at the final time examined before. Interestingly, the highest resolution for the classic scheme shows the largest variation but produces the smallest errors. The new scheme in contrast produces the lowest errors for the lowest resolutions as observed before. Both schemes produce very similar curves for both maximum and mean error suggesting that the overall variance of the error is rather limited.

Figure 5.12 shows the results for the Schär-type mountain. Qualitatively the picture is very similar to the one for the bell-shaped mountain. After initial growth the errors tend

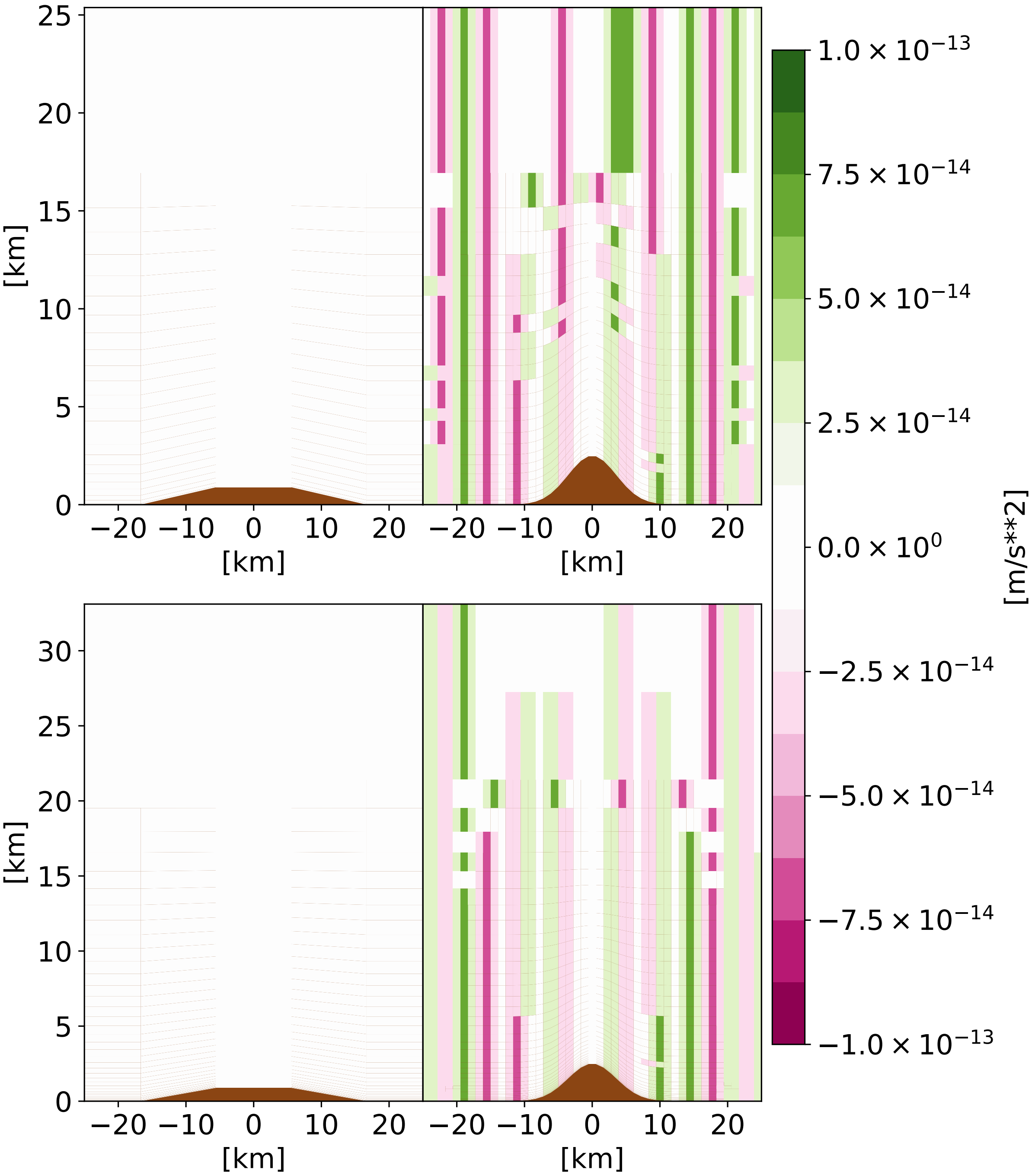

Figure 5.9: *Pressure gradient error at initial time* $t = 0\,\mathrm{s}$ *for the PGFCONST scheme and the bell-shaped mountain. Shown are the results for 27 and 40 levels (top to bottom) and* 10 km *as well as* 1 km *(left to right) respectively. Orography is shown in brown.*

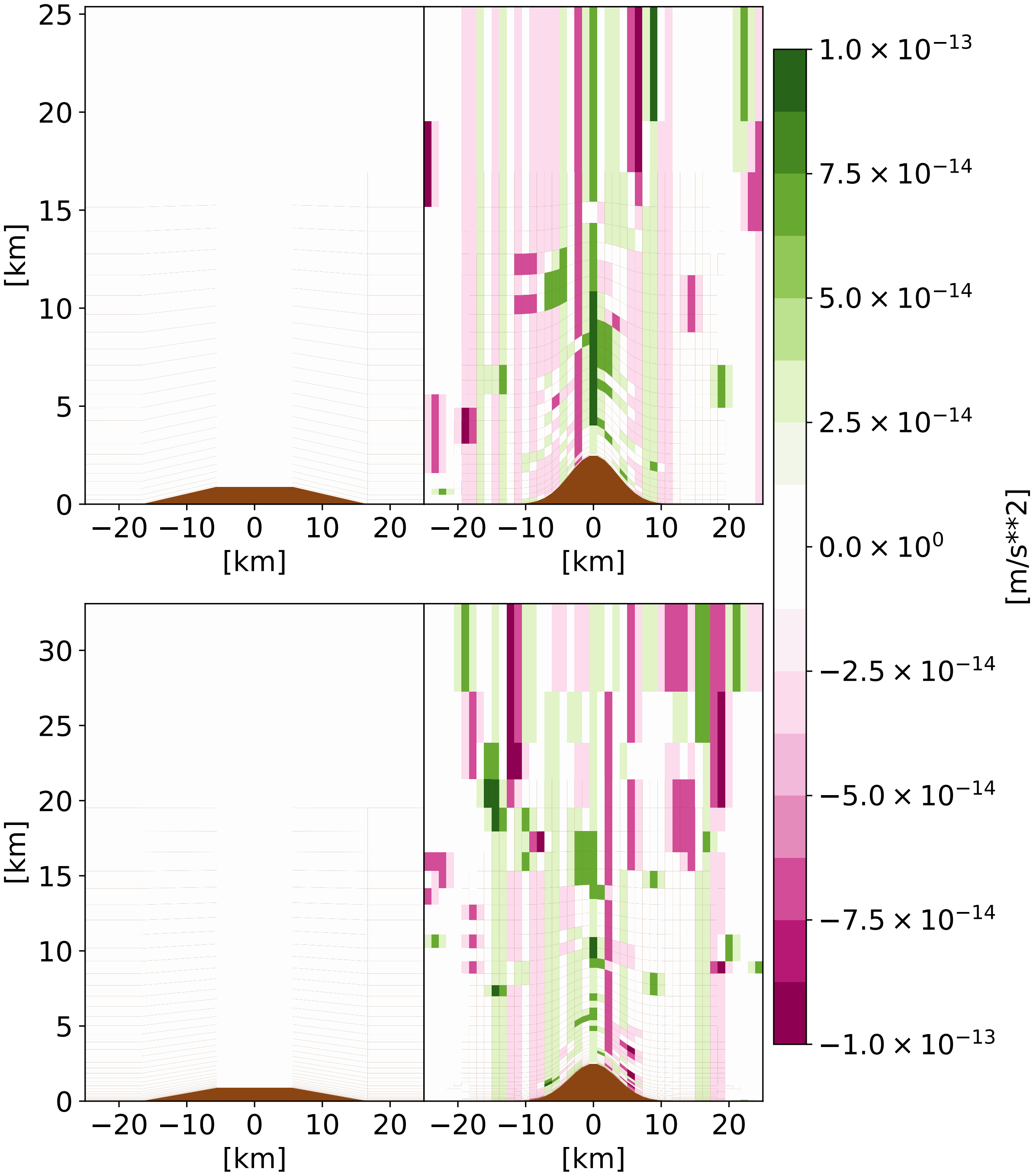

Figure 5.10: *Pressure gradient error at final time $t = 3600\,\mathrm{s}$ for the PGFCONST scheme and the bell-shaped mountain. Shown are the results for 27 and 40 levels (top to bottom) and 10 km as well as 1 km (left to right) respectively. Orography is shown in brown.*

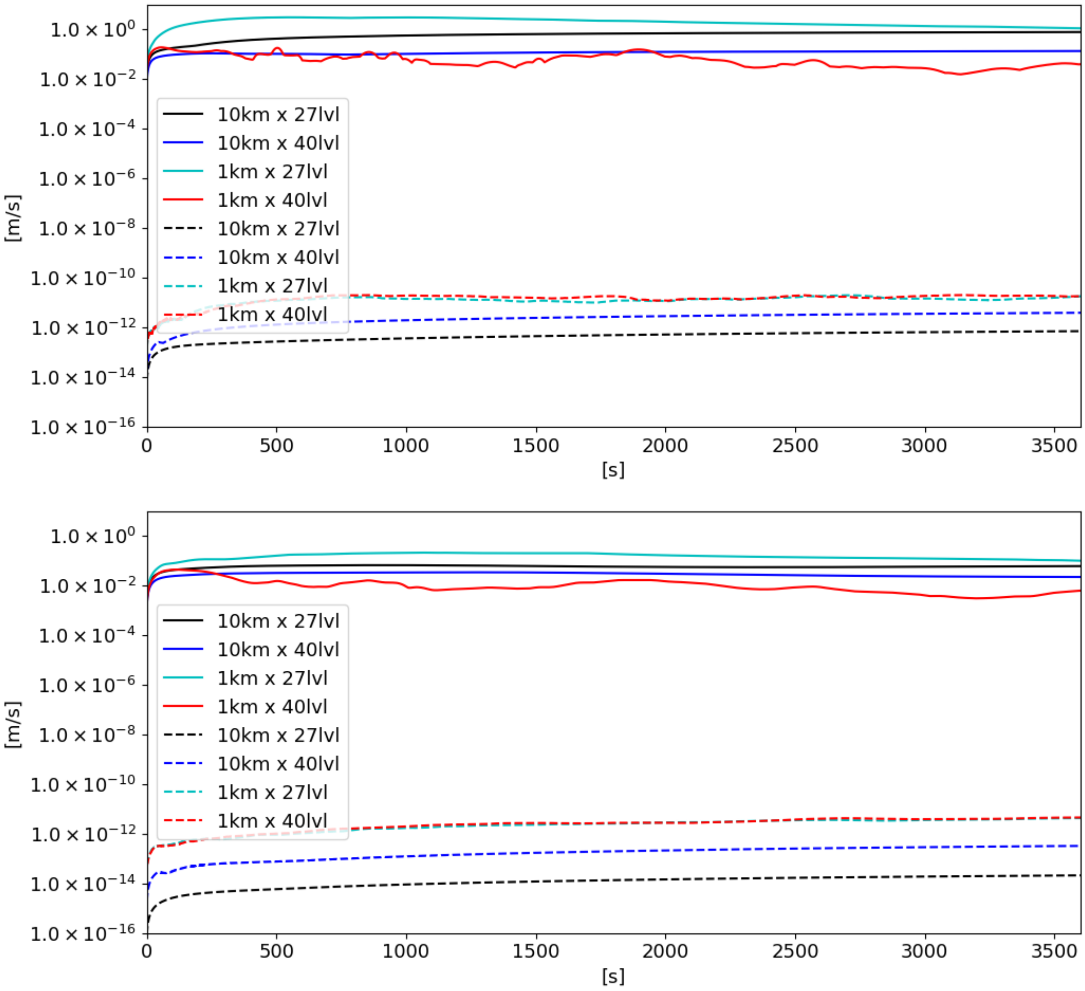

Figure 5.11: *Maximum (top) and mean (bottom) absolute u-error for the isothermal case and the bell-shaped mountain. Values are shown for the classic scheme (solid) and the PGFCONST scheme (dashed). Colors indicate different resolutions.*

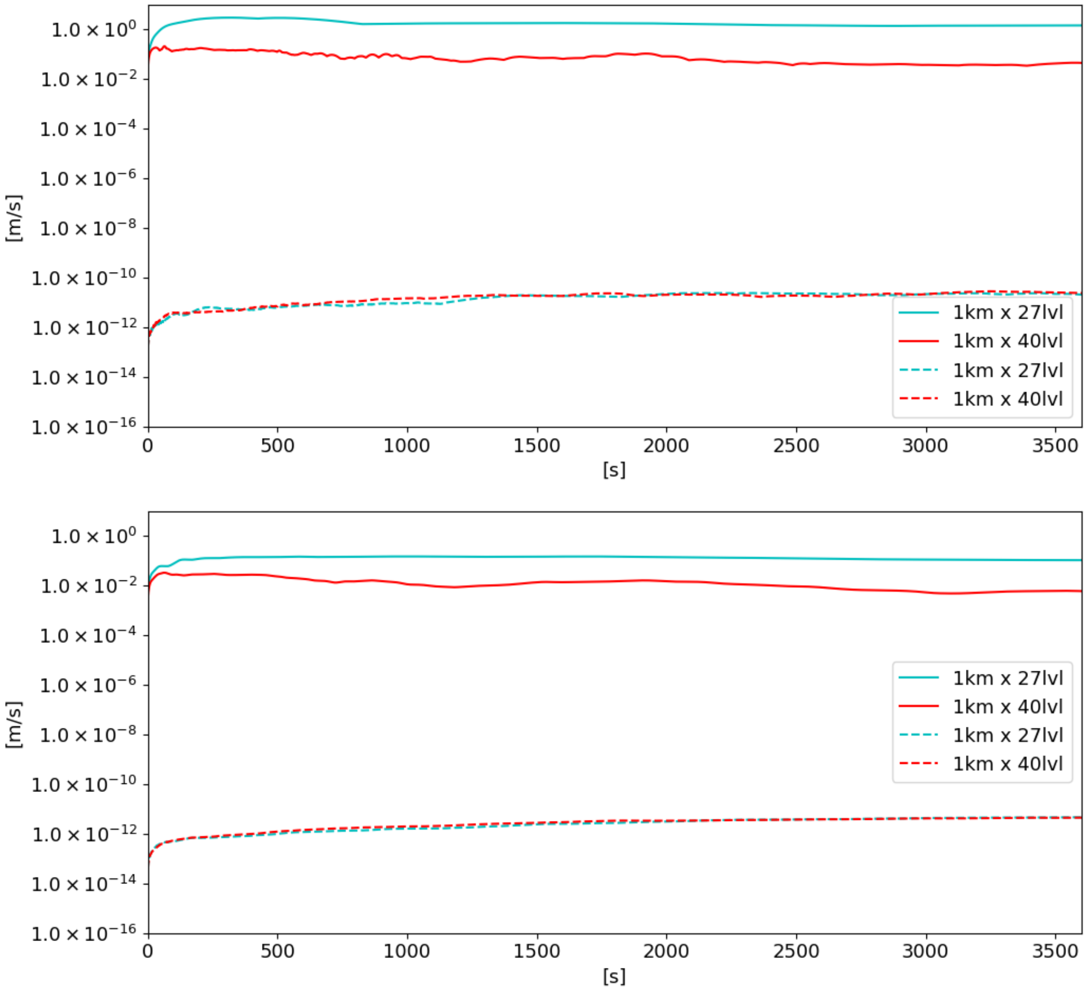

Figure 5.12: *Maximum (top) and mean (bottom) absolute u-error for the isothermal case and the Schär-type mountain. Values are shown for the classic scheme (solid) and the PGFCONST scheme (dashed). Colors indicate different resolutions.*

to settle into a new equilibrium for the classic scheme. The new scheme also exhibits slight initial error growth but the magnitude is essentially negligible.

Clearly, the new scheme produces substantially smaller errors both for the PGF and the u-wind. However, the errors are significantly larger than machine epsilon. According to the theoretical predictions this should only be possible due to rounding errors which are hardware dependent and not inherent to the scheme itself. I.e., if carried out with infinite precision the scheme should produce no error at all. It has also been conjectured that the unexpectedly large error may be connected to the high number of floating point operations used to calculate the geopotential. Each such operation introduces additional round-off error. This would also explain why the errors for the scheme appear to grow with higher resolution. To confirm this hypothesis the simulations were repeated as before but this time the known geopotential was prescribed instead of estimating it based on the given data. In this way the summation over the vertical levels can be avoided to greatly reduce the round-off error incurred. If the hypothesis is correct most or all of the error exhibited in the previous results should vanish. Figure 5.13 shows the pressure gradient error for the first 5 min of the simulation for a single point centered above the mountain in the mid-atmosphere. The upper picture shows the error for the PGFCONST scheme without provision of the exact geopotential values. The values oscillate with high frequency around the zero line as is common for well-balanced schemes. The lower picture shows the results of the PGFCONST scheme when the exact geopotential is prescribed. The errors exhibited before completely vanish and are exactly zero. This confirms the initial suspicion: the observed errors stem exclusively from the approximation of the geopotential. However, due to the simplicity of the isothermal case the geopotential approximation is exact outside of round-off error. Therefore, it can be concluded that the errors encountered are due to round-off and round-off alone. That is, the scheme is well-balanced for the isothermal case as previously predicted. However, in light of the perturbation produced by round-off error alone much larger errors can be expected when the geopotential is additionally afflicted by truncation errors. Such an example will be investigated in the next section.

To sum up, it has been shown that the new scheme is well-balanced for the isothermal equilibrium with substantial improvements over the classic method. The new scheme is able to achieve much better results with much lower resolutions. Moreover, in some cases stability benefits of the new scheme were observed. On the other hand, round-off errors incurred in the computation of the geopotential prevent the scheme from producing errors in the range of machine epsilon. Instead the errors are two to four orders of magnitude above this threshold. This suggests a high susceptibility of the new scheme to even small errors in the geopotential.

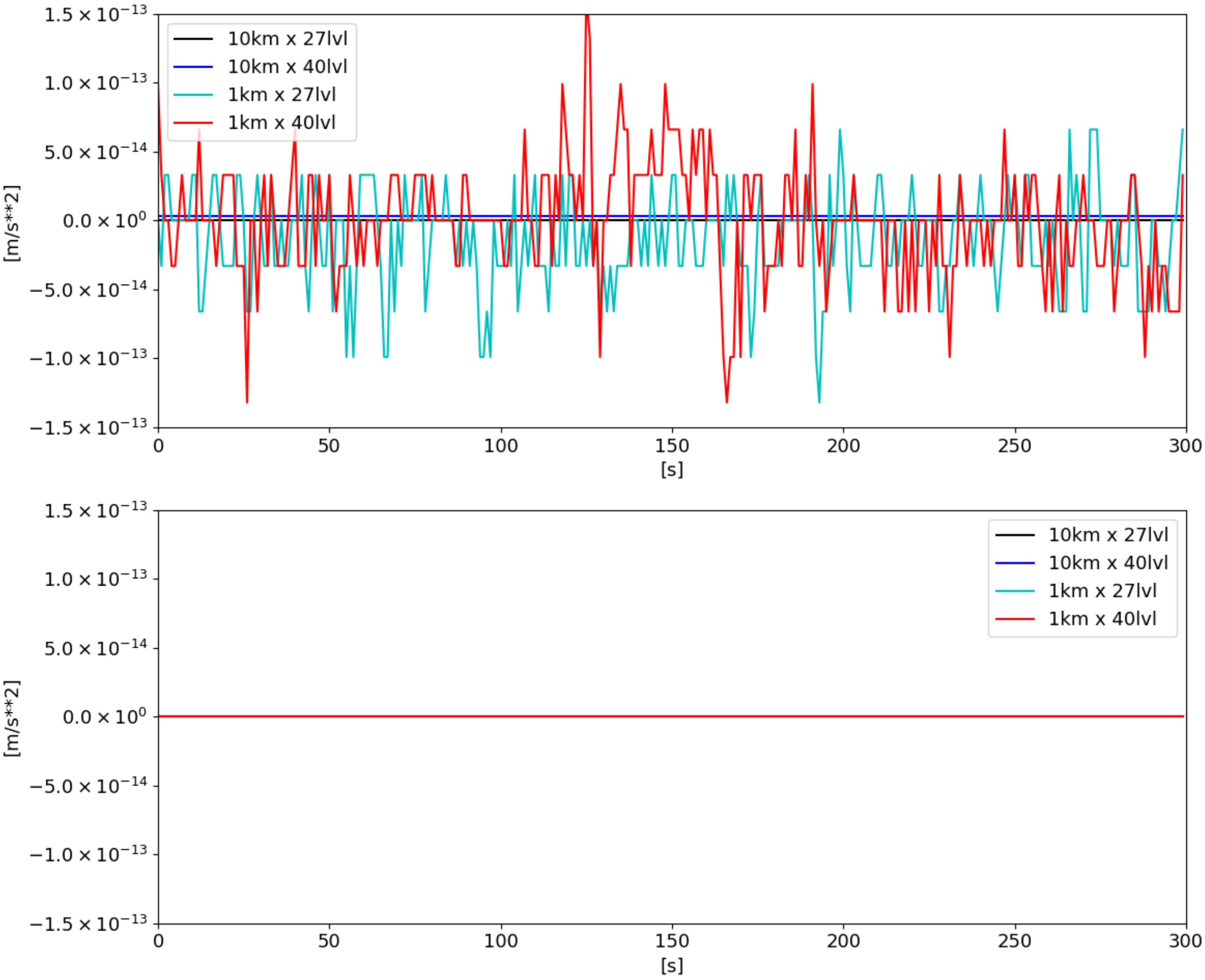

Figure 5.13: *Pressure gradient error for a single point centered above the bell-shaped mountain. Values are shown for the PGFCONST scheme (top) and the PGFCONST scheme with exact geopotential (bottom). Colors indicate different resolutions.*

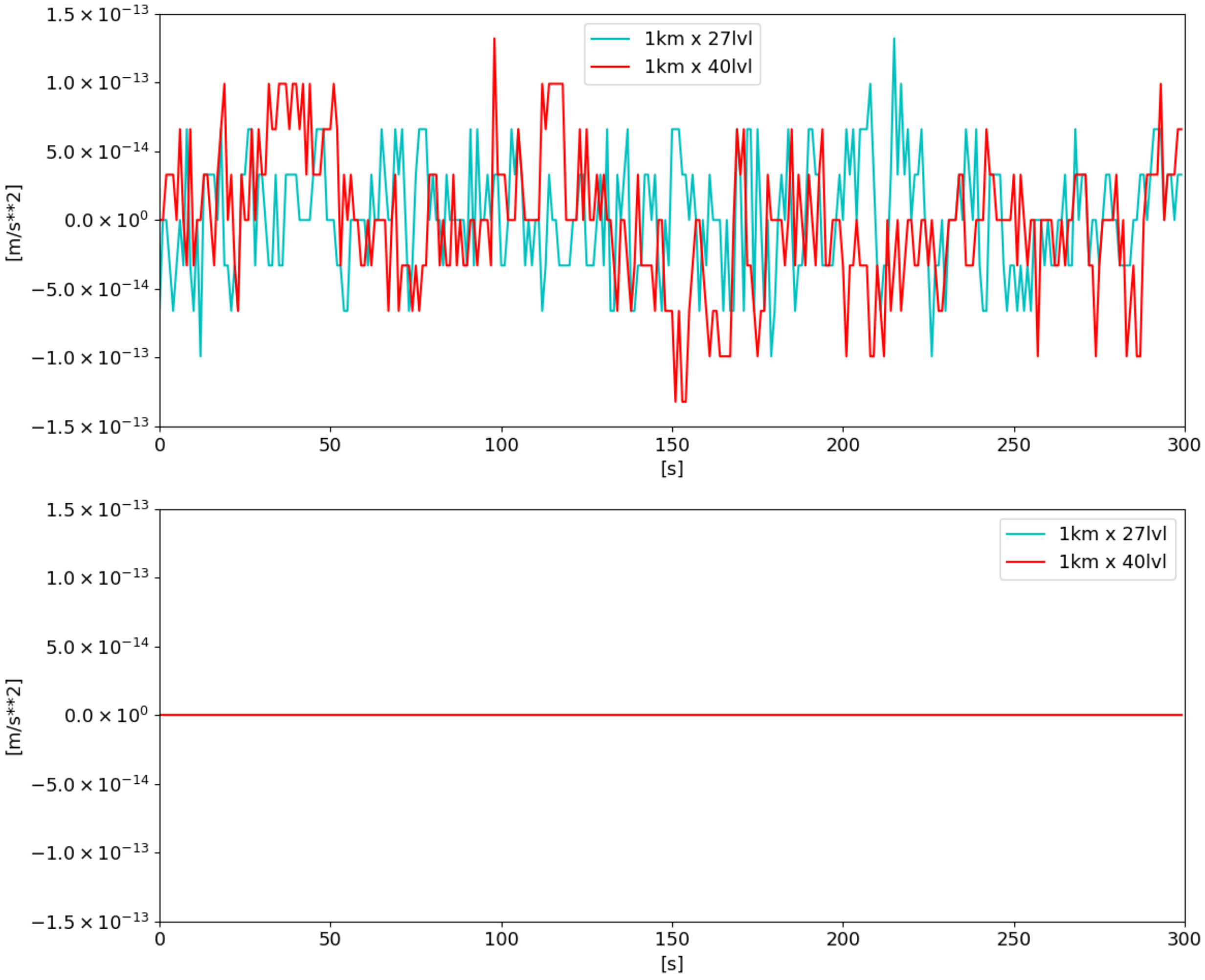

Figure 5.14: *Pressure gradient error for a single point centered above the Schär-type mountain. Values are shown for the PGFCONST scheme (top) and the PGFCONST scheme with exact geopotential (bottom). Colors indicate different resolutions.*

5.2 The Standard Atmosphere

In this section the performance of the scheme on a more complex test case is investigated. The same computational domain and orographies as in the previous section is used but the model is initialized with the standard atmosphere derived in chapter 3. This test case is characterized by a piecewise linear temperature distribution. In such a case the geopotential will not only contain round-off errors as in the previous example but also truncation errors. Looking at the apparent high sensitivity of the scheme in regards to the geopotential drastically different results are to be expected.

5.2.1 Results

Here, the results for the standard atmosphere test case are presented both in terms of spatial error structure and evolution over time.

Spatial Error

Figure 5.15 shows the results for the classic scheme and the bell-shaped mountain at the end of the simulation. The magnitude of the error especially for the lower resolutions is much larger than for the isothermal equilibrium. This is likely due to the increased complexity of the vertical temperature distribution in this scenario. It has been seen previously that the classic scheme often produces large initial errors that settle down over time. The higher resolutions both vertically (lower right) and horizontally (upper right) exhibit drastically smaller errors. It is likely that the scheme needs a longer time at the lower resolutions to disperse the initial disturbances and reach a new equilibrium. Interestingly, at least for the higher resolutions the largest errors are now found more in the mid-atmosphere in contrast to the stratospheric maximum in the isothermal case. This is likely due to the structure of the standard atmosphere that is characterized by a constant temperature lapse rate below 11 km followed by an isothermal layer above that.

Figure 5.16 shows the results for the PGFCONST scheme. Interestingly, the picture is strikingly similar to that for the classic scheme. While the magnitude of error is slightly reduced the spatial structure is virtually the same quite unlike the situation in the isothermal case. Clearly, this is due to the additional truncation error generated in approximating the geopotential. It has previously been seen how very small round-off errors can accumulate and have a significant influence on the results. The truncation errors however are much larger than round-off errors and consequently exhibit a much stronger influence. Unfortunately, this appears to prohibit any substantial improvement on the

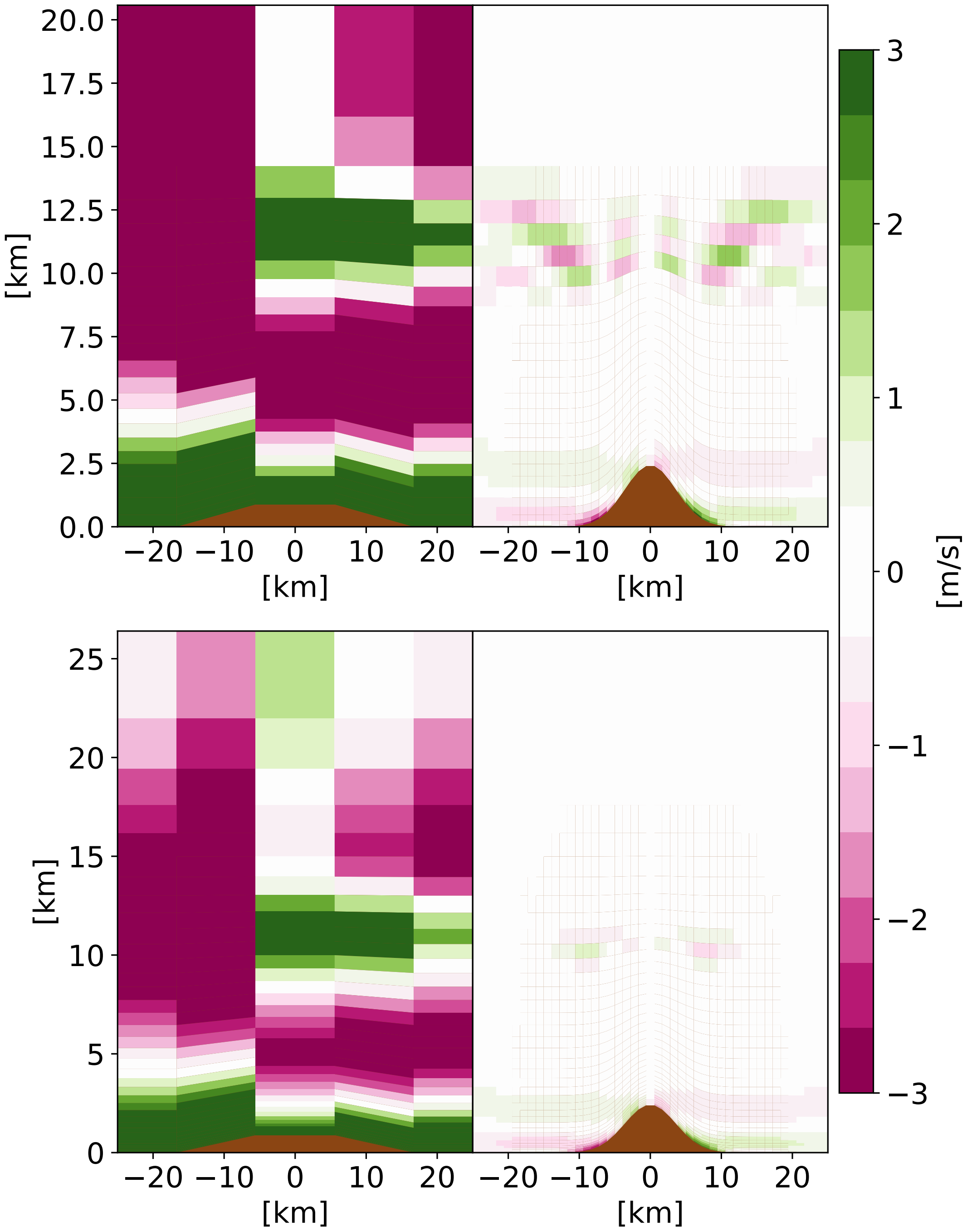

Figure 5.15: *u-error at final time $t = 3600\,\mathrm{s}$ for the classic scheme and the bell-shaped mountain (standard atmosphere case). Shown are the results for 27 and 40 levels (top to bottom) and $10\,\mathrm{km}$ as well as $1\,\mathrm{km}$ (left to right) respectively. Orography is shown in brown.*

results of the classic scheme. Figure 5.17 shows the results for the PGFLIN scheme. Both qualitatively and quantitatively the results agree with those of the PGFCONST and the classic scheme. There is a slight improvement over the PGFCONST scheme due to the linear approximations but it is negligible. Apparently, the geopotential errors are much too pronounced to allow the linear approximations to have a stronger impact.

Figure 5.18 shows the results for the Schär-type mountain. The overall picture is similar but the largest errors now occur closer to the ground most likely due to the increased complexity of the orography. Again the classic and the new schemes produce very similar errors structurally and quantitatively. As previously seen the new schemes produce slightly smaller errors but the difference is mostly negligible. In some areas the PGFLIN scheme improves over the PGFCONST scheme but the effect of the linear approximations is limited as in the previous situation.

Now the PGE for the standard atmosphere case is investigated. Figure 5.19 shows the pressure gradient error at the initial time for the classic scheme. The PGE exhibits virtually the same spatial structure with four distinct and symmetric regions of large error centered above the mountain. The largest errors are found in the upper atmosphere as before and the magnitude of the error is also very similar to the isothermal case. This suggests that at least some of the greatly increased u-error found in the standard atmosphere case is not a direct consequence of the PGE but due to indirect effects when the initial disturbance interacts with the rest of the scheme. Figure 5.20 depicts the situation at the end of the simulation. Interestingly, the results with lower horizontal resolution (left) show greatly increased PGE compared to the initial time. The simulations with higher horizontal resolution (right) on the other hand exhibit greatly reduced error. This is consistent with the situation in the isothermal case where the initial PGE has been seen to disperse over time leading into a disturbed equilibrium. However, in the isothermal case the error also decreased for the lower resolutions albeit more slowly. It is possible that this process simply needs more time for the standard atmosphere case or that the low resolution prevents dispersion and instead drifts off into an atmosphere in full motion.

Figure 5.21 shows the pressure gradient error for the PGFCONST scheme at the beginning of the simulation. The plots with higher horizontal resolution (right) exhibit a pattern similar to the classic scheme. The error in the upper atmosphere is slightly reduced over the classic scheme but conversely the error close to the ground is increased. On the other hand, the results for the lower horizontal resolution (left) show greater differences to the classic scheme. Quantitatively and qualitatively the results for the lower atmosphere are comparable. However, the upper atmosphere exhibits greatly decreased error. Possibly, the error builds up from the bottom of the atmosphere up to the top and this process is faster for the classic scheme. Figure 5.22 shows the situation by the end of the simulation and gives some credence to this conjecture. The picture on the right hand side now looks very similar to the one for the classic scheme again including the separating layer observed around the 5 km mark. The pictures with high horizontal

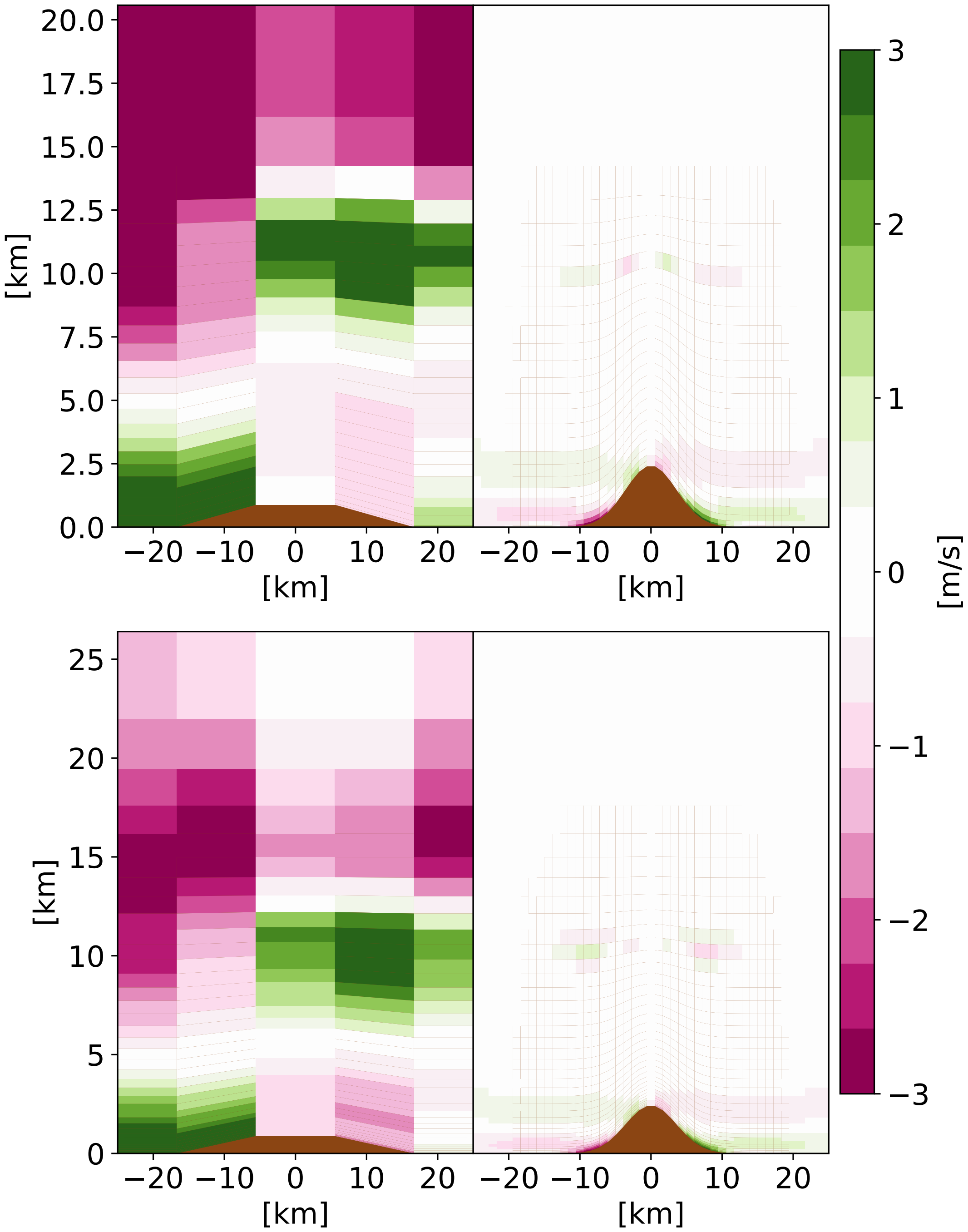

Figure 5.16: *u-error at final time* $t = 3600\,\mathrm{s}$ *for the PGFCONST scheme and the bell-shaped mountain (standard atmosphere case). Shown are the results for* 27 *and* 40 *levels (top to bottom) and* 10 km *as well as* 1 km *(left to right) respectively. Orography is shown in brown.*

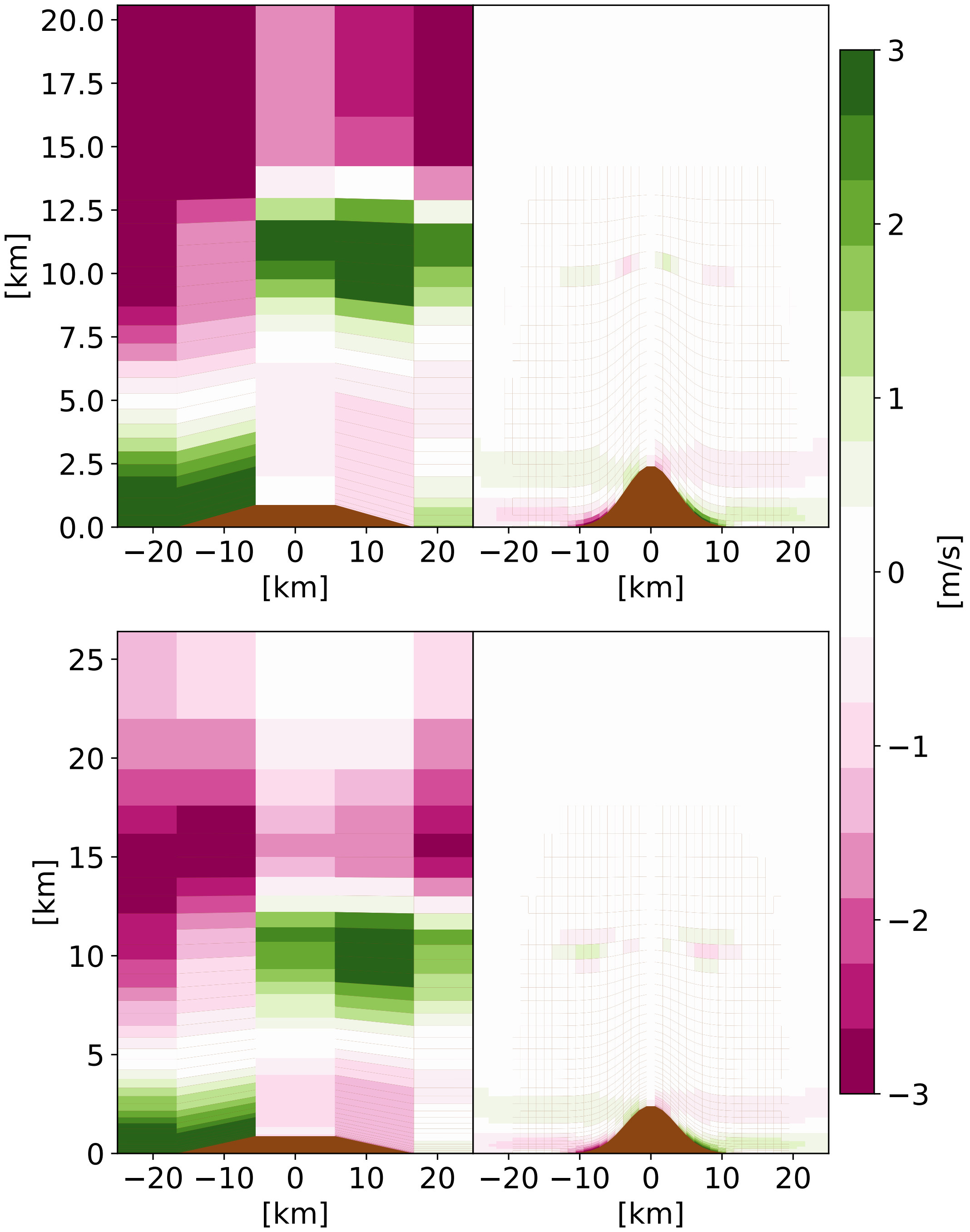

Figure 5.17: *u-error at final time $t = 3600\,\mathrm{s}$ for the PGFLIN scheme and the bell-shaped mountain (standard atmosphere case). Shown are the results for 27 and 40 levels (top to bottom) and 10 km as well as 1 km (left to right) respectively. Orography is shown in brown.*

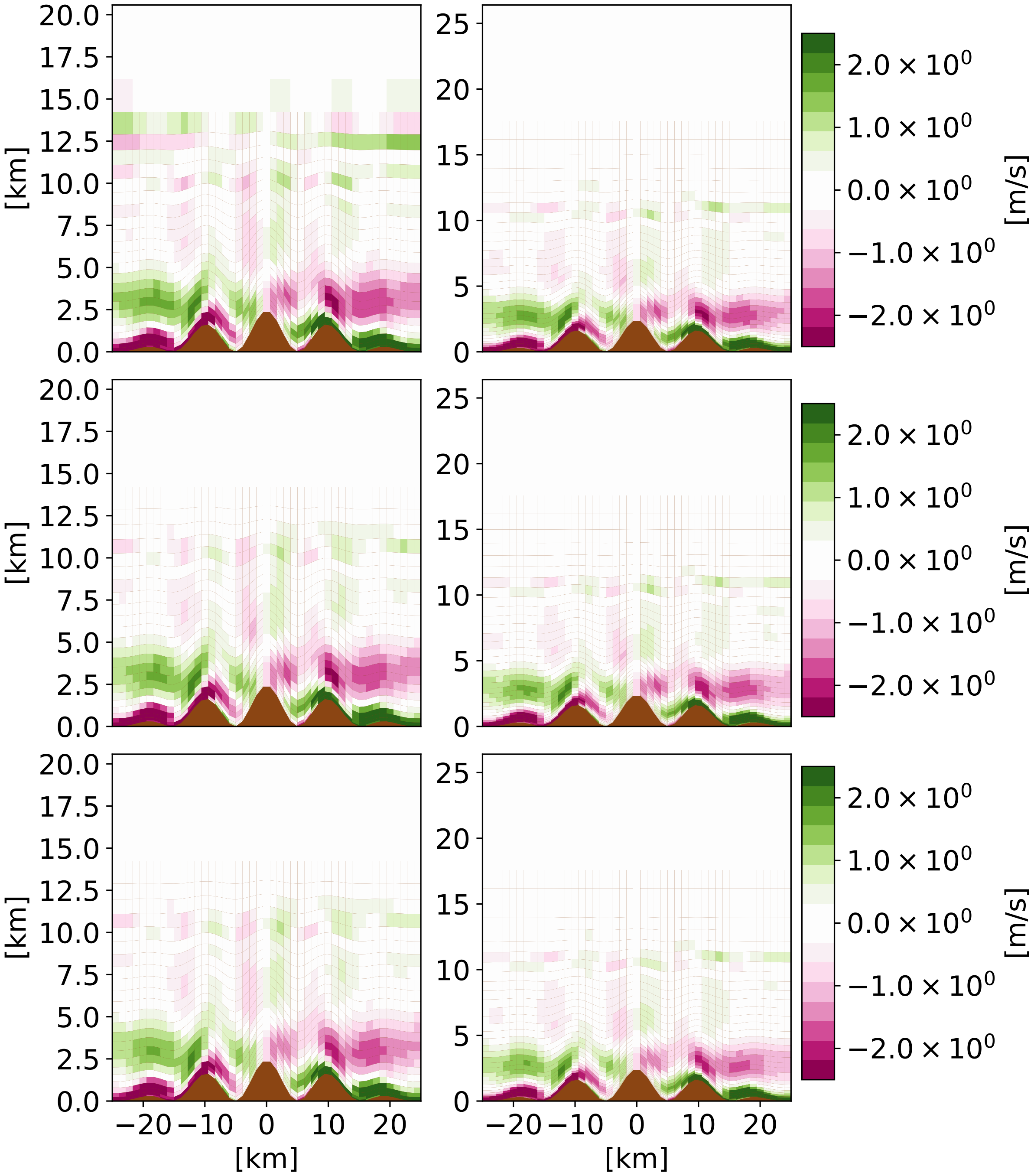

Figure 5.18: *u-error at final time $t = 3600\,\mathrm{s}$ for the Schär-type mountain (standard atmosphere case). Shown are the results for 27 and 40 levels (left to right) and for the classic, the PGFCONST and PGFLIN schemes (top to bottom).*

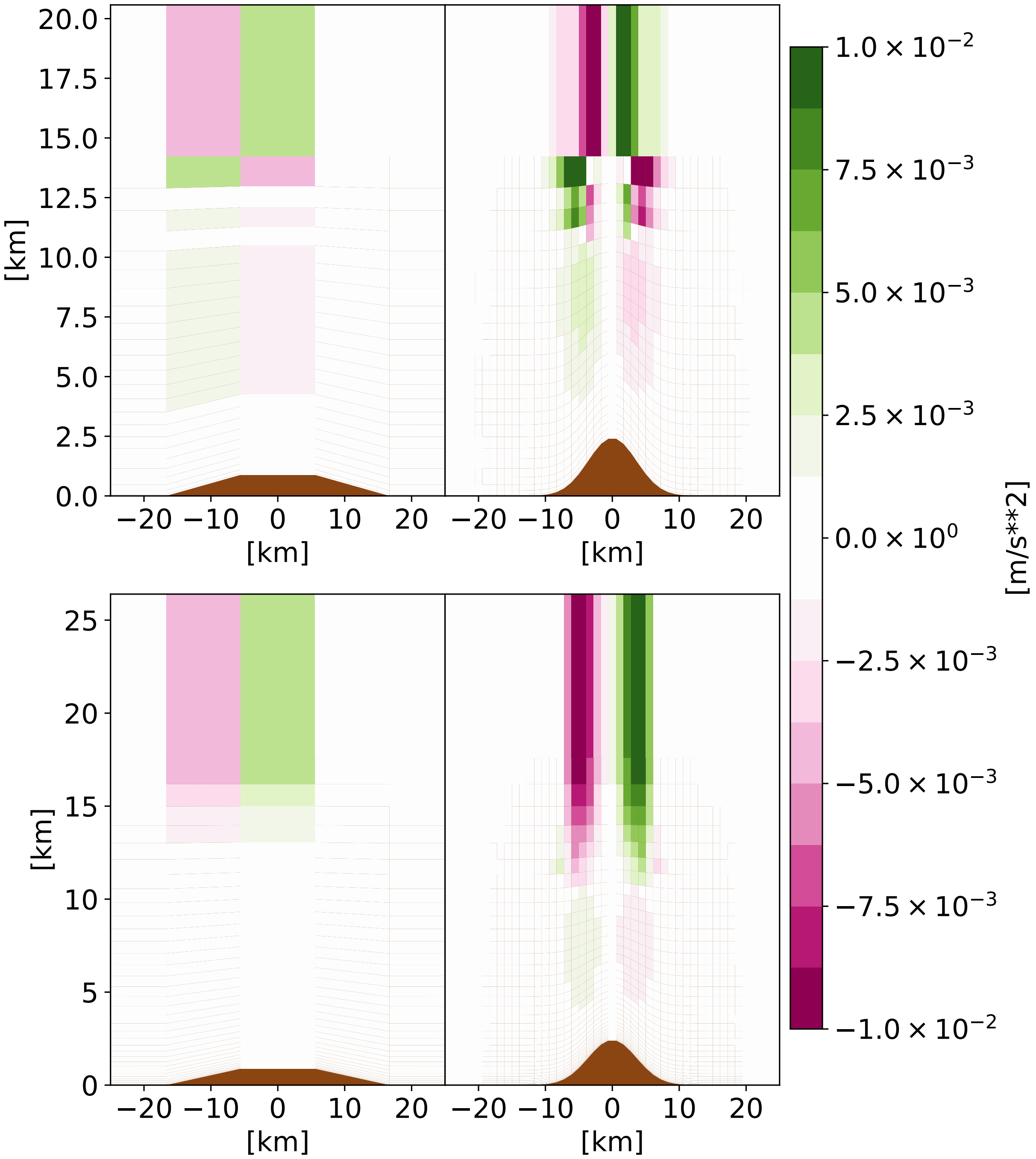

Figure 5.19: *Pressure gradient error at initial time $t = 0\,\mathrm{s}$ for the classic scheme and the bell-shaped mountain (standard atmosphere case). Shown are the results for 27 and 40 levels (top to bottom) and 10 km as well as 1 km (left to right) respectively. Orography is shown in brown.*

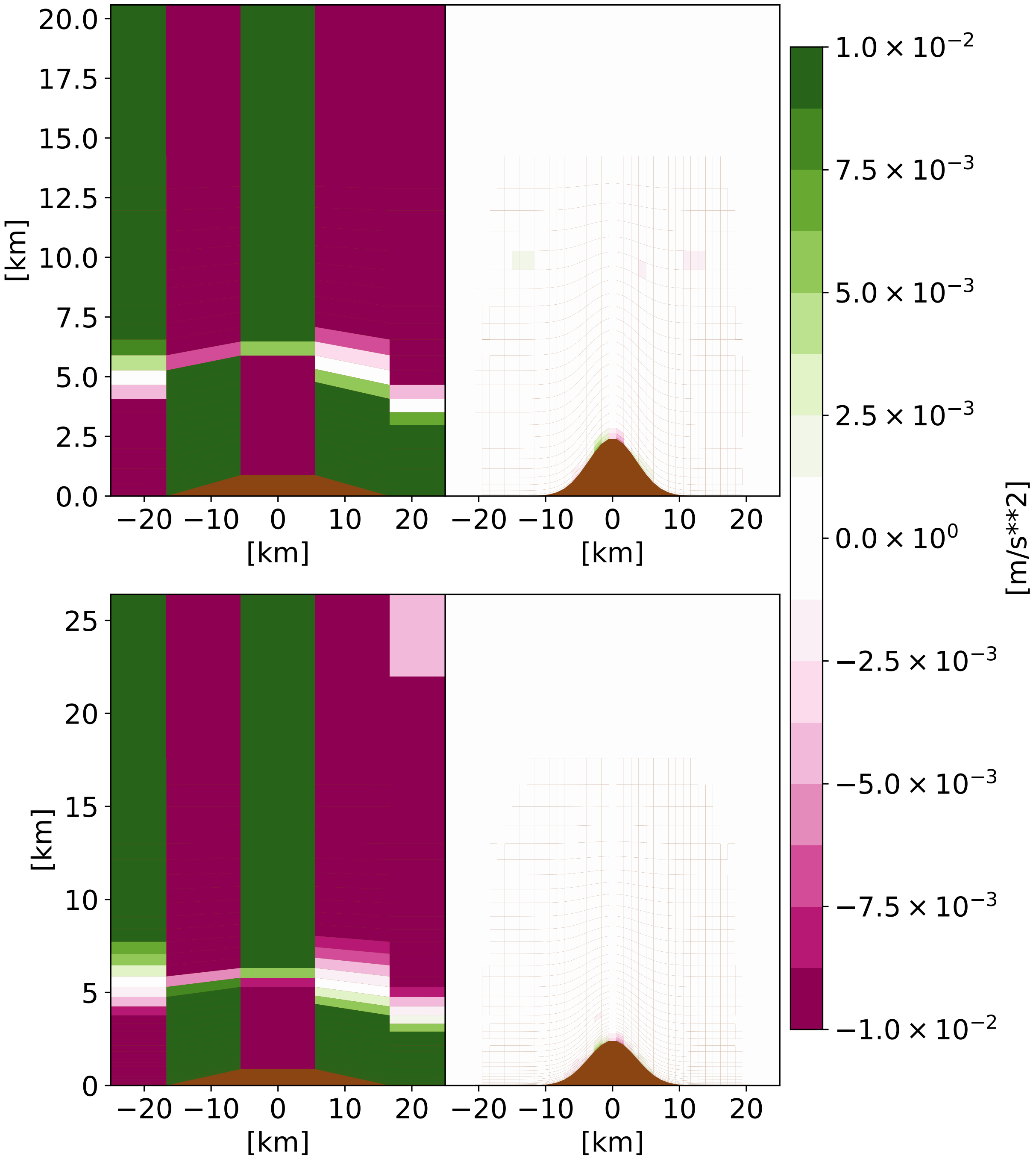

Figure 5.20: *Pressure gradient error at final time* $t = 3600\,\mathrm{s}$ *for the classic scheme and the bell-shaped mountain (standard atmosphere case). Shown are the results for 27 and 40 levels (top to bottom) and* 10 km *as well as* 1 km *(left to right) respectively. Orography is shown in brown.*

resolution (right) show substantially reduced error compared to the classic scheme. One interpretation is that both schemes disperse the initial PGE over time (at least if the resolution is sufficient) but that the new scheme is slightly more efficient at this.

Finally, Figure 5.23 shows the results for the PGFLIN scheme. The only significant difference to the PGFCONST scheme is the absence of the large errors close to the ground in the simulations with low horizontal resolution (left). As before this error is expected to build up over time as in the previous example. The improved linear approximations appear to slow this process down even further in comparison to the classic and PGFCONST scheme. Figure 5.24 confirms the expectations and shows virtually the same structure as for the two other schemes. For the higher horizontal resolutions (right) the PGE has mostly dispersed suggesting that no or little further spurious motion is produced at this point in time.

Time Evolution

The development of the u-error over the course of the experiments is briefly investigated here. Figure 5.25 shows the maximum (top) and mean (bottom) u-error for the standard atmosphere case. Particularly interesting are the curves for the low horizontal resolutions (blue and black). The error initially decreases as observed in previous examples but then starts to grow rapidly again. Apparently the initial disturbances in the PGF are too large to readjust to a disturbed equilibrium as seen before. This behavior is however only observed for the classic scheme. The errors for the PGFCONST scheme (dashed) continue to decline after the initial growth period. The higher resolutions are both qualitatively and quantitatively similar between the classic and the new scheme as expected from the spatial error analysis.

Figure 5.26 shows the results for the Schär-type mountain. For the maximum error (top) the situation is similar to the bell-shaped example, but all errors exhibit sustained growth including the new scheme. At the same time a large difference between the maximum and mean (bottom) error can be observed. This suggests that only a few grid points produce very large errors whereas most points do not. Likely this can be attributed to the increased complexity of the Schär-type mountain but a more detailed analysis would be required to confirm that.

To sum up, the results for the standard atmosphere case appear to suggest that the new scheme produces slightly improved results. However, the magnitude of improvement is essentially negligible and the scheme is far from well-balanced. Before it has been shown that most of the error is connected to the accuracy with which the geopotential is approximated. Clearly, for the standard atmosphere the errors in the geopotential are too large and overpower most of the improvements that may have manifested otherwise. To confirm this the simulations were also repeated with prescribed exact geopotential.

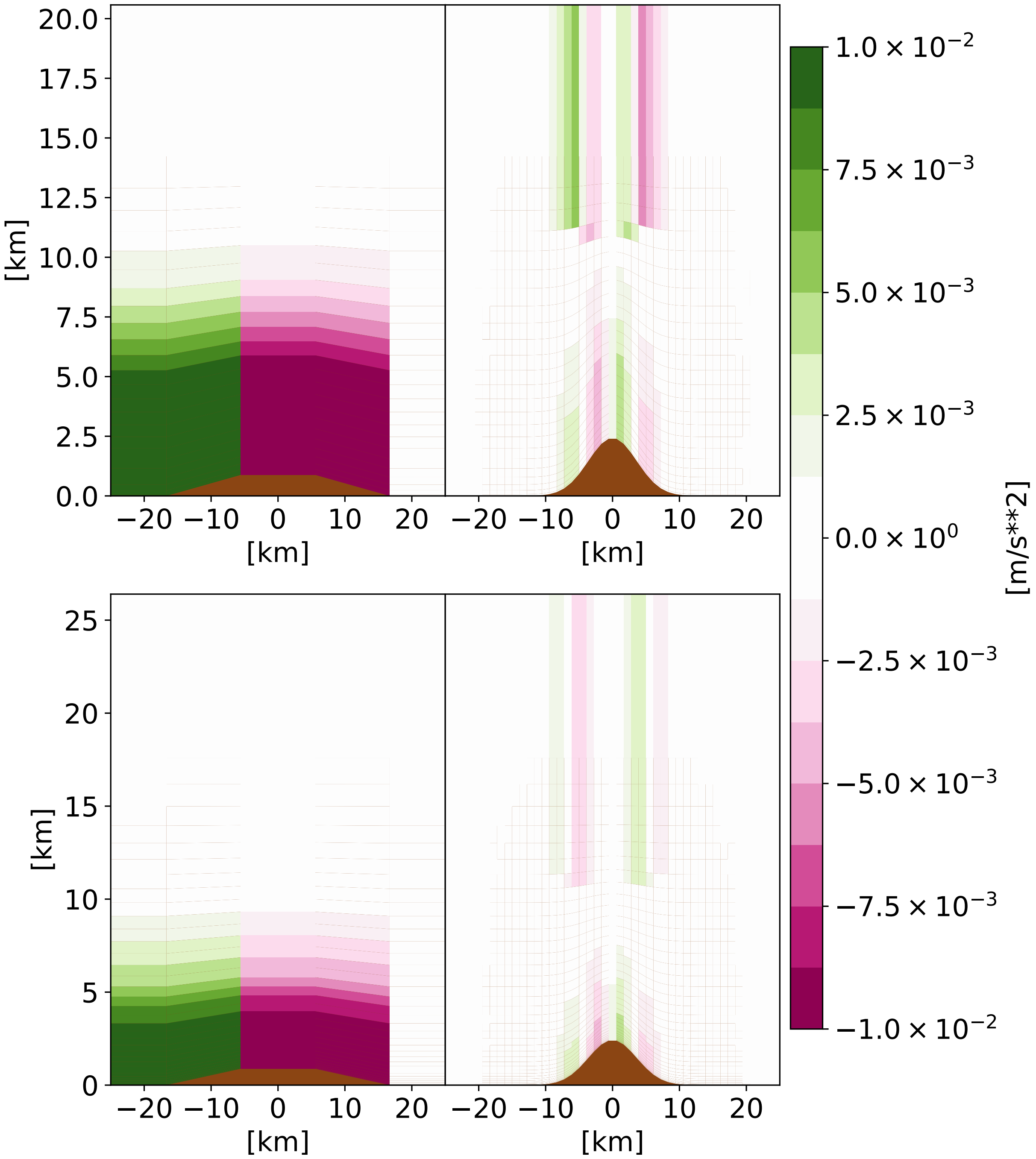

Figure 5.21: *Pressure gradient error at initial time $t = 0\,\mathrm{s}$ for the PGFCONST scheme and the bell-shaped mountain (standard atmosphere case). Shown are the results for 27 and 40 levels (top to bottom) and 10 km as well as 1 km (left to right) respectively. Orography is shown in brown.*

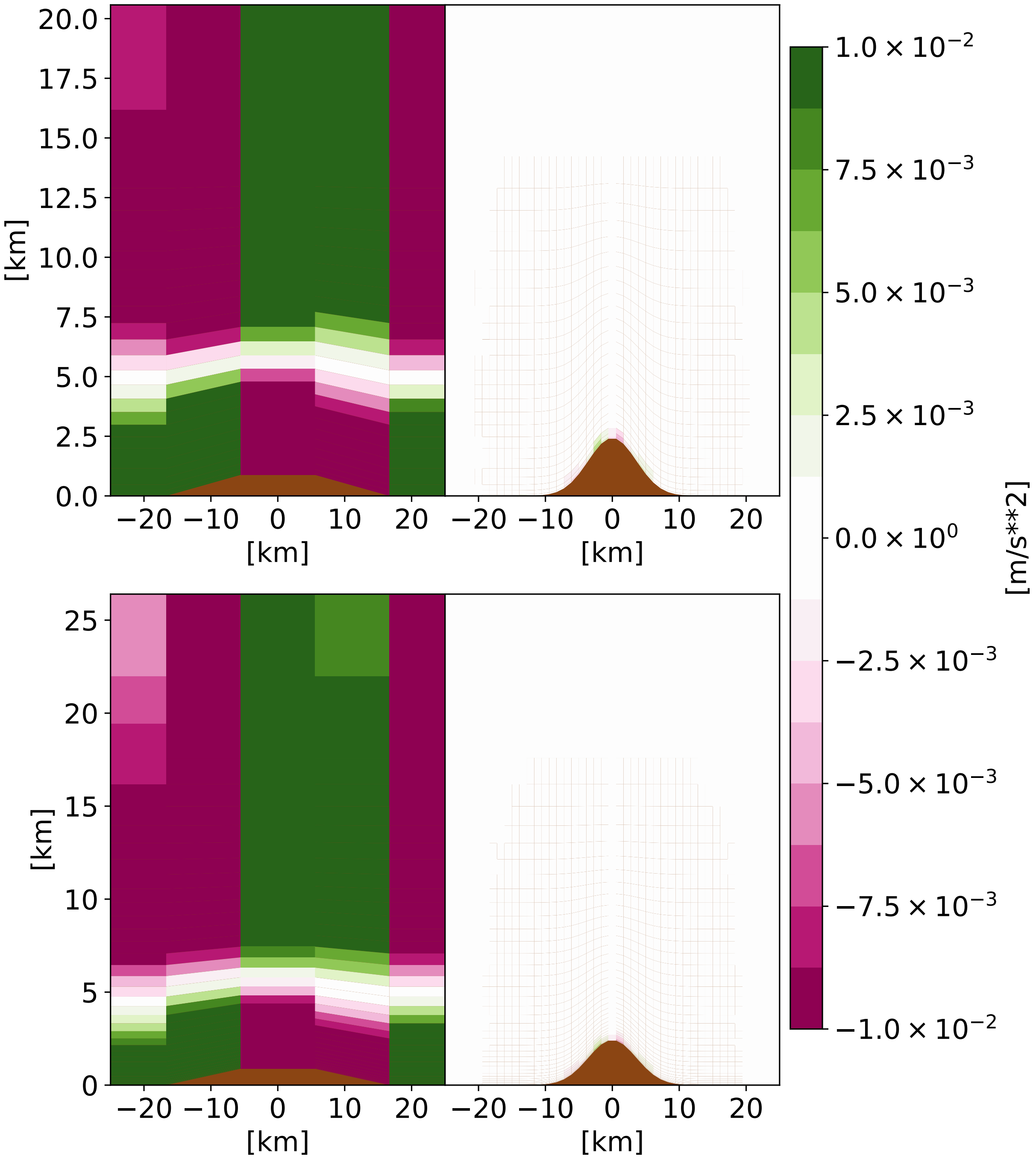

Figure 5.22: *Pressure gradient error at final time* $t = 3600\,\mathrm{s}$ *for the PGFCONST scheme and the bell-shaped mountain (standard atmosphere case). Shown are the results for 27 and 40 levels (top to bottom) and* 10 km *as well as* 1 km *(left to right) respectively. Orography is shown in brown.*

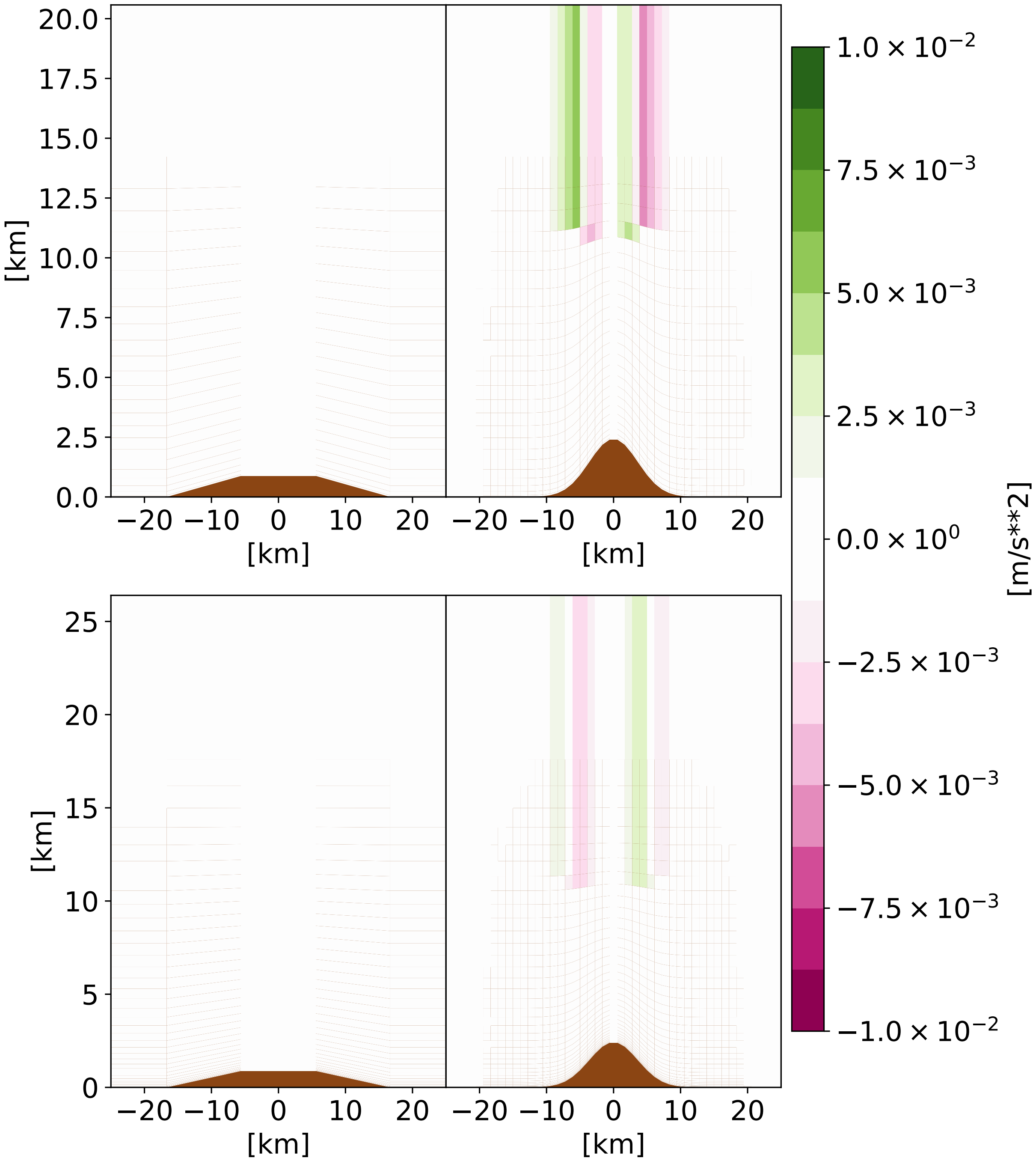

Figure 5.23: *Pressure gradient error at initial time $t = 0\,\mathrm{s}$ for the PGFLIN scheme and the bell-shaped mountain (standard atmosphere case). Shown are the results for 27 and 40 levels (top to bottom) and 10 km as well as 1 km (left to right) respectively. Orography is shown in brown.*

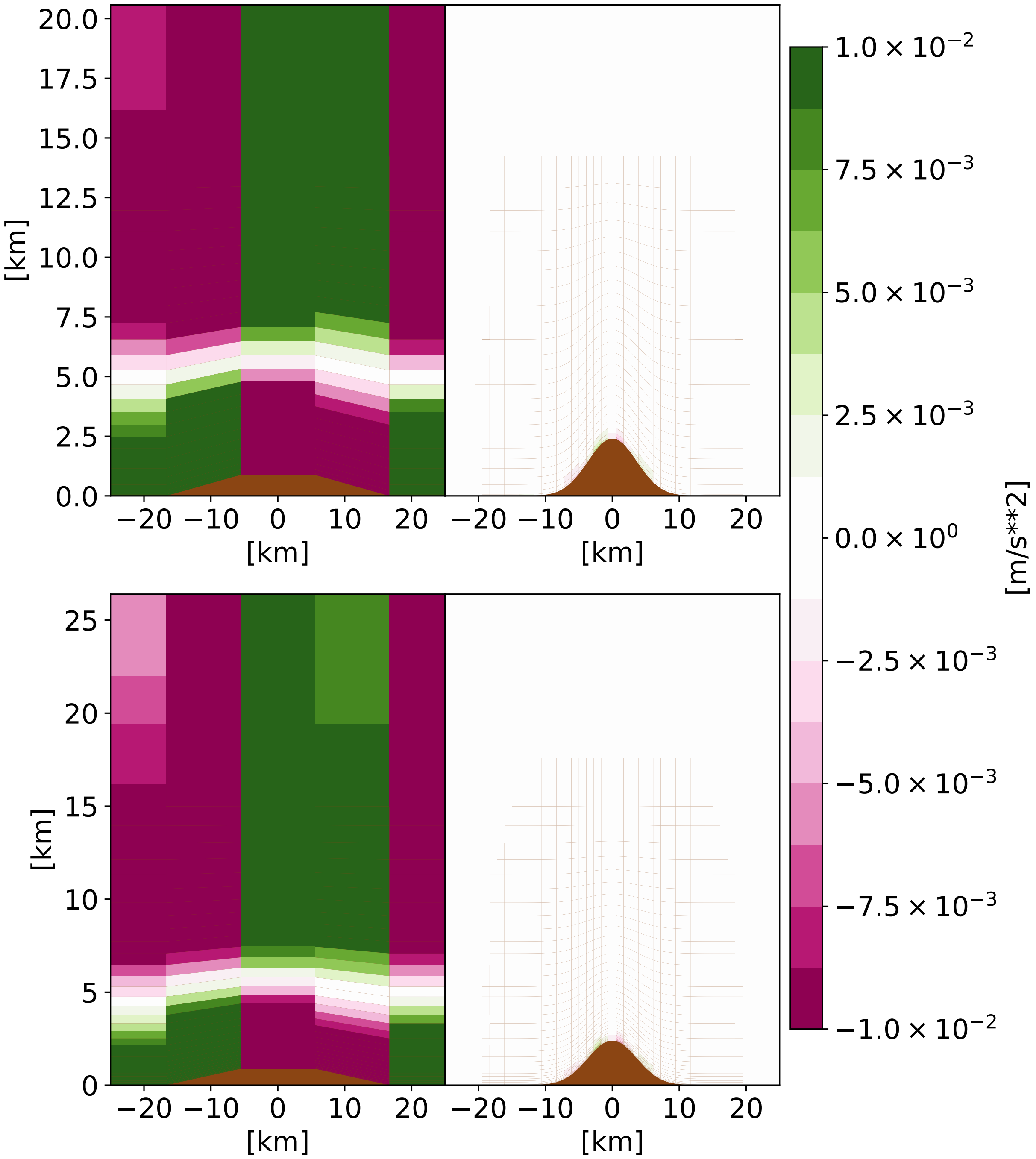

Figure 5.24: *Pressure gradient error at final time* $t = 3600\,\mathrm{s}$ *for the PGFLIN scheme and the bell-shaped mountain (standard atmosphere case). Shown are the results for 27 and 40 levels (top to bottom) and 10 km as well as 1 km (left to right) respectively. Orography is shown in brown.*

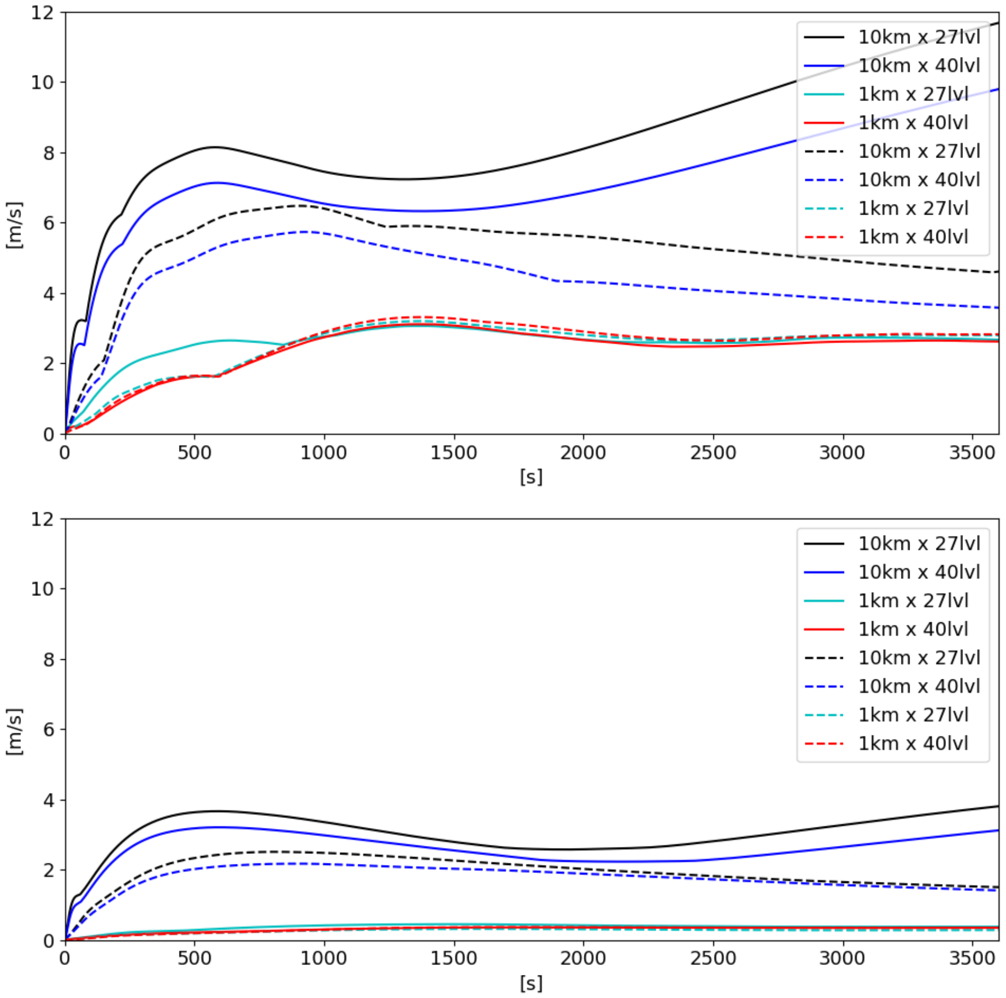

Figure 5.25: *Maximum (top) and mean (bottom) absolute u-error for the standard atmosphere case and the bell-shaped mountain. Values are shown for the classic scheme (solid) and the PGFCONST scheme (dashed). Colors indicate different resolutions.*

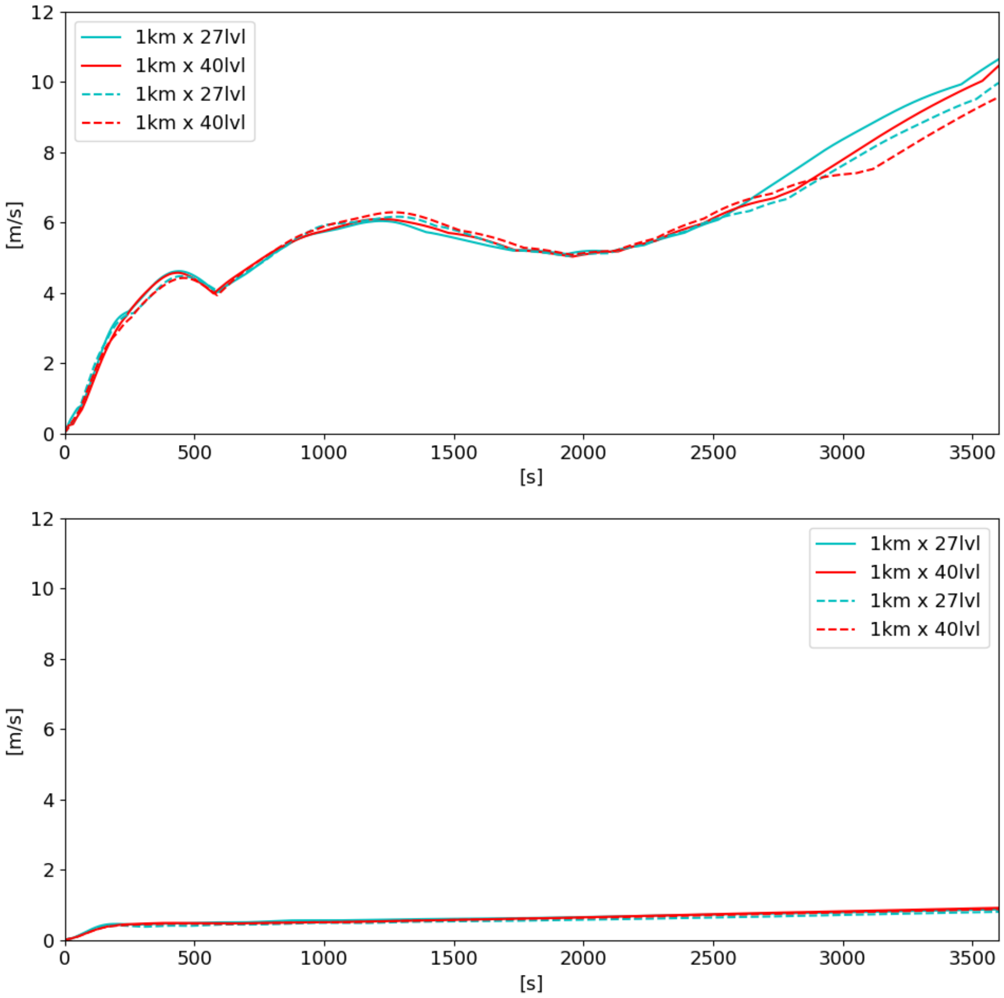

Figure 5.26: *Maximum (top) and mean (bottom) absolute u-error for the standard atmosphere case and the Schär-type mountain. Values are shown for the classic scheme (solid) and the PGFCONST scheme (dashed). Colors indicate different resolutions.*

In that case the error is once again equal to zero as in the isothermal case. This suggests that the current scheme may be a step in the right direction but in its current state will not yield well-balanced results for equilibria more complex than the isothermal one.

6 Conclusions and Future Perspectives

In this chapter a brief summary of the present work is given and the progress that has been made in terms of the guiding research questions is critically discussed. Furthermore, an outlook of possible future research trajectories is given.

6.1 Summary

In the present work the question whether existing numerical techniques developed under the umbrella term well-balancing can be transferred to the regional hydrostatic climate model REMO in order to reduce mountain-induced spurious circulation in the presence of complex orography was investigated. To that end, the state-of-the-art research pertaining to well-balancing different kinds of equation sets in climate and NWP modeling and related fields were reviewed. It was found that the framework developed in Botta et al. (2004) is most likely to be applicable to a hydrostatic finite difference (FD) model. The two key factors in this judgment were the similarities of the equation systems (non-hydrostatic vs. hydrostatic Euler-equations) and the relative ease of application to second-order centered differences as used in the REMO model. The main challenge in transferring the approach to the REMO model was the change from a Cartesian to a pressure-based hybrid vertical terrain-following coordinate system (TFCS) as commonly used in FD models of the atmosphere. Additionally, both the vertical and horizontal staggering used in the REMO model required further modification of the original method. In the course of development a novel characterization of equilibrium states in the η-coordinate system was found that provides additional geometric insight and was also used in transferring the reconstruction technique for hydrostatic background states to the REMO framework. It was proven mathematically that the newly developed scheme is well-balanced for isothermal equilibria for any given (smooth) orography irrespective of its complexity. That notion was validated by implementing the new scheme in a 2D-version of the REMO model and applying it to an isothermal resting atmosphere test case with two examples of steep orographic gradients. Furthermore, the scheme was tested on a more challenging standard atmosphere equilibrium.

6.2 Critical Discussion and Conclusions

In this section the research questions posed in the introduction are reviewed and the answers that can be given based on the findings in the present work are discussed.

- *Can existing well-balancing approaches be transferred to hydrostatic FDM climate models?*

It has been shown for the first time that at least one of the existing well-balancing approaches (Botta et al. 2004) can be successfully transferred to hydrostatic FD models such as REMO. As is the case with most well-balancing techniques this requires the reconstruction of local hydrostatic equilibria based on the available prognostic point values in a given cell and its vicinity. To some extent, this approach can be compared to the canonical method of subtracting constant hydrostatic reference states from the prognostic variables before computing the pressure gradient force (PGF) as commonly used in NWP (e.g., Gary 1973). However, the advantage of the method proposed here is that the reference states are reconstructed each time step and for each individual cell. Constant reference states on the other hand need to be constructed based on initial data and are therefore unable to adapt to long term changes in the underlying hydrostatic equilibrium. Such changes are to be expected in simulations of past and future climate with integration times of 50 years or more in contrast to NWP applications with just a few days. This is one of the reasons why advancements in well-balancing are particularly desirable for climate models. With its capacity to retain the isothermal equilibrium for arbitrarily complex terrain the method developed in the present work can be considered a first but important step in that direction.

- *Is this effective and efficient in reducing the pressure gradient error encountered in the presence of steep and complex orography?*

It has been shown both theoretically and in practical examples that at least for the most simple isothermal equilibrium the newly developed PGF discretization proves effective in treating rather complex orography such as Schär-type mountain ridges. The PGE is greatly reduced in comparison to the standard method and in some cases showed more favorable stability properties. In fact, for these specific equilibria the new scheme is fully well-balanced, i.e., is independent of grid resolution and produces non-zero errors purely due to the finite precision of floating point computations. On the other hand, the investigation shows that the method is inherently sensitive to round-off errors due to the high number of floating point operations expended in approximating the geopotential. As a result even the isothermal equilibrium produced errors much larger than machine epsilon. Moreover, when tested with the more complex standard atmosphere equilibrium the results of the new scheme were no better or worse than the standard method. It has been shown that if the exact geopotential is provided the method does yield well-balanced results for this case as well. This proves that the provision of accurate geopotential values is the key for this method to improve on the PGE. Unfortunately, the requirements in accuracy appear to be very demanding. On average the approximated geopotential in the standard atmosphere case only deviates from the true values by a few meters. Yet, all possible improvements in balancing compared to the standard method are lost. It is highly unlikely that geopotential approximations accurate enough to retain the benefits of the method are achievable for practical purposes. In terms of efficiency the new scheme has excellent properties as the additional cost of computing the PGF is essentially negligible. Moreover, the implementation is rather straightforward and requires no substantial refactoring of existing code. In light of this it has to be concluded that the proposed technique is efficient but unfortunately not very effective outside of very idealized situations.

- *How does this relate to the different types of TFCSs employed, e.g., pressure-based vs. height-based systems?*

The present work has exclusively dealt with a hybrid pressure-based TFCS. It has been found that at least for the approach followed here pressure based coordinates present a possibly incurable obstacle in achieving improved balancing properties. In such TFCS the geopotential is commonly computed by integrating the hydrostatic equation along the vertical. It has been seen that this can not only produce round-off errors but also substantial truncation errors stemming from the estimation of vertical pressure gradients as well as numerical quadrature. The current method however hinges on the mathematical consistency of temperature, pressure and geopotential values. The latter however is not given as initial data (such as the prognostic variables T and p_s) but instead diagnosed from the other two via discrete approximations. It appears outright inconceivable that the required grade of consistency could be achieved across different equilibria and atmospheric states. In the original method (Botta et al. 2004) this issue was not encountered because the consistent geopotential could simply be acquired from the vertical z-coordinate. In the η-system the vertical coordinate is required to compute the pressure instead (in conjunction with the given surface pressure) and no information pertaining to the geopotential is provided in this way. On the other hand, pressure-based systems allow the reduction of the full pressure equation to a surface pressure equation. Traditionally, this was seen as an advantage due to reduced computational load and improved memory management. In light of the recent advances in computing technology these features seem less relevant today. Consequently, it would appear promising to change to a height-based TFCS such as the Gal-Chen-coordinate. In this way, the geopotential could be acquired from the vertical coordinate which has been seen to be key to successful application of the method. However, this is where the picture gets a bit more complex. A hydrostatic model such as REMO needs a way of enforcing the hydrostatic consistency of its prognostic values. I.e., when pressure and temperature are given the geopotential must be chosen such that the hydrostatic equation holds at least approximatively. Therefore, changing to a height-based TFCS would offer no benefit at least for hydrostatic models. Suppose temperature is given as initial data and geopotential is derived from the alternative coordinate then the pressure must be chosen such that the hydrostatic equation holds. The only obvious way to achieve that would be to diagnose the pressure by vertical integration of the hydrostatic equation rather than solving a full prognostic pressure equation. The net result of such a change would hence be a reversal of the roles of pressure and geopotential in the current scheme. It can therefore be concluded that when a hydrostatic model is concerned neither pressure- nor height-based TFCS provide a favorable environment for the proposed scheme. One interpretation of this is that the enforcement of hydrostatic consistency in hydrostatic models is at least as much a cause of the PGE as the terrain-following coordinate transformation. To the author's knowledge most of the existing literature attributes the PGE to the use of TFCSs alone. The results of this thesis suggest that the canonical way of enforcing hydrostaticity exacerbates the issue substantially.

6.3 Outlook

In this section a brief outlook on possible future research directions based on the findings of the present work is given. As pointed out previously the proposed scheme has very high demands in terms of the accuracy required in approximating the geopotential. However, it is unlikely for any approximation technique to consistently achieve the needed precision outside of singular idealized cases. It has been shown that the sensitivity to errors in the geopotential is twofold. On the one hand round-off errors related to the number of floating point computations increase the PGE above machine epsilon even in technically well-balanced cases. This could possibly be addressed by employing quad precision, but only to the geopotential computations. In this way, the relevant round-off errors would be minimized without slowing down computations too much. On the other hand in more complex examples the geopotential is additionally afflicted with truncation error. Here, a Taylor analysis of the error terms may identify ways to apply appropriate corrections to the discrete approximation of the integrals used in computing the geopotential. This may at least reduce the impact of such truncation errors and thereby increase the practical applicability of the scheme.

It may also be fruitful to explore alternative ways of enforcing hydrostatic consistency. For instance, if a height-based TFCS is applied instead of a pressure-based one it may be possible to derive a prognostic pressure equation that produces results consistent with the geopotential derived from the vertical coordinate. In this way, the main obstacles to successful application of the method developed here would be removed.

Moreover, it may be promising to investigate whether the new discretization may be used in connection with a non-hydrostatic model. On the one hand, it appears counterintuitive that a method that fails to balance a hydrostatic model should work on a more complex non-hydrostatic model. On the other hand, non-hydrostatic models do not need to enforce hydrostatic consistency removing the main source of difficulty with this scheme. However, crucially the non-hydrostatic model would have to employ a height-based TFCS such that the geopotential can be derived from the vertical coordinate. Together with temperature and pressure from the prognostic equations the necessary ingredients for the application of the scheme would be given. Non-hydrostatic models formulated in hydrostatic terrain-following pressure coordinates (Laprise 1992; Janjić, Gerrity, and Ničković 2001) still diagnose the geopotential from an analogue of the hydrostatic equation sometimes referred to as the hypsometric equation. Hence, they will likely not benefit from the technique developed here.

Clearly, the suggested trajectories of future research may yield conflicting or negative results and unveil new challenges not encountered in the present work. Yet, they provide novel pathways in a longstanding research problem that is still waiting for a convincing solution decades into its conception.

Appendices

Vertical Coordinate Parameters for Test Cases

Here, the vertical coordinate parameters A and B (see subsection 2.2.2 and specifically (2.6)) used for the test cases in chapter 5 are given. Note that the parameters are defined at half layers. I.e., the experiments with 27 and 40 full layers yield 28 and 41 coordinate parameters respectively.

Table A1: Vertical Coordinate Parameters for 27 Full Layers

Level	A	B
1	0.0000000	0.0000000
2	5000.0000000	0.0000000
3	10000.0000000	0.0000000
4	13600.0000000	0.0000000
5	14736.3554688	0.0203192
6	15689.2070312	0.0369749
7	16266.6093750	0.0594876
8	16465.0039062	0.0878950
9	16297.6210938	0.1220036
10	15791.5976562	0.1614415
11	14985.2695312	0.2057033
12	13925.5195312	0.2541886
13	12665.2929688	0.3062354
14	11261.2304688	0.3611450
15	9771.4062500	0.4182023
16	8253.2109375	0.4766881
17	6761.3398438	0.5358866
18	5345.9140625	0.5950842
19	4050.7177734	0.6535646
20	2911.5693359	0.7105944
21	1954.8051758	0.7654052
22	1195.8898926	0.8171670
23	638.1489258	0.8649558
24	271.6264648	0.9077159
25	72.0635834	0.9442132
26	0.0000000	0.9729852
27	0.0000000	0.9922815
28	0.0000000	1.0000000

Table A2: Vertical Coordinate Parameters for 40 Full Layers

Level	A	B
1	0.0000000	0.0000000
2	2000.0000000	0.0000000
3	4000.0000000	0.0000000
4	6000.0000000	0.0000000
5	8000.0000000	0.0000000
6	9988.8828380	0.0001970
7	11914.5244690	0.0015110
8	13722.9429420	0.0048840
9	15369.7308560	0.0110760
10	16819.4762690	0.0206780
11	18045.1835870	0.0341210
12	19027.6944760	0.0516900
13	19755.1087570	0.0735340
14	20222.2053090	0.0996750
15	20429.8629670	0.1300230
16	20384.4814280	0.1643840
17	20097.4021470	0.2024760
18	19584.3292430	0.2439330
19	18864.7503930	0.2883230
20	17961.3577410	0.3351550
21	16899.4687940	0.3838920
22	15706.4473210	0.4339630
23	14411.1242610	0.4847720
24	13043.2186180	0.5357100
25	11632.7583640	0.5861680
26	10209.5013400	0.6355470
27	8802.3561550	0.6832690
28	7438.8030920	0.7287860
29	6144.3150030	0.7715970
30	4941.7782130	0.8112530
31	3850.9134220	0.8473750
32	2887.6966030	0.8796570
33	2063.7799050	0.9078840
34	1385.9125530	0.9319400
35	855.3617500	0.9518220
36	467.3335770	0.9676450
37	210.3938940	0.9796630
38	65.8892430	0.9882700
39	7.3677430	0.9940190
40	0.0000000	0.9976300
41	0.0000000	1.0000000

References

Adcroft, A., C. Hill, and J. Marshall (Sept. 1997). “Representation of Topography by Shaved Cells in a Height Coordinate Ocean Model”. In: *Monthly Weather Review* 125.9, pp. 2293–2315. DOI: `10.1175/1520-0493(1997)125%3C2293:ROTBSC%3E2.0.CO;2`.

Arakawa, A. and C. S. Konor (1996). “Vertical Differencing of the Primitive Equations Based on the Charney–Phillips Grid in Hybrid σ–p Vertical Coordinates”. In: *Monthly Weather Review* 124.3, pp. 511–528. DOI: `10.1175/1520-0493(1996)124%3C0511:VDOTPE%3E2.0.CO;2`.

Arakawa, A. and V. R. Lamb (1977). “Computational Design of the Basic Dynamical Processes of the UCLA General Circulation Model”. In: *General Circulation Models of the Atmosphere*. Ed. by J. Chang. Vol. 17. Methods in Computational Physics: Advances in Research and Applications. Elsevier, pp. 173–265. DOI: `10.1016/B978-0-12-460817-7.50009-4`.

Arakawa, A. and M. J. Suarez (1983). “Vertical Differencing of the Primitive Equations in Sigma Coordinates”. In: *Monthly Weather Review* 111.1, pp. 34–45. DOI: `10.1175/1520-0493(1983)111%3C0034:VDOTPE%3E2.0.CO;2`.

Audusse, E. et al. (2004). “A Fast and Stable Well-Balanced Scheme With Hydrostatic Reconstruction for Shallow Water Flows”. In: *SIAM Journal on Scientific Computation* 25.6, pp. 2050–2065. DOI: `10.1137/S1064827503431090`.

Beckmann, A. and D. B. Haidvogel (1993). “Numerical Simulation of Flow around a Tall Isolated Seamount. Part I: Problem Formulation and Model Accuracy”. In: *Journal of Physical Oceanography* 23.8, pp. 1736–1753. DOI: `10.1175/1520-0485(1993)023%3C1736:NSOFAA%3E2.0.CO;2`.

Beniston, M. (2012). “Impacts of climatic change on water and associated economic activities in the Swiss Alps”. In: *Journal of Hydrology* 412–413, pp. 291–296. DOI: `10.1016/j.jhydrol.2010.06.046`.

Bonaventura, L. (2000). “A Semi-implicit Semi-Lagrangian Scheme Using the Height Coordinate for a Nonhydrostatic and Fully Elastic Model of Atmospheric Flows”. In: *Journal of Computational Physics* 158.2, pp. 186–213. DOI: `10.1006/jcph.1999.6414`.

Botta, N. et al. (May 2004). “Well balanced finite volume methods for nearly hydrostatic flows”. In: *Journal of Computational Physics* 196.2, pp. 539–565. DOI: `10.1016/j.jcp.2003.11.008`.

Daley, R. (1988). “The normal modes of the spherical non-hydrostatic equations with applications to the filtering of acoustic modes”. In: *Tellus A: Dynamic Meteorology and Oceanography* 40.2, pp. 96–106. DOI: `10.3402/tellusa.v40i2.11785`.

Davies, H. C. (1976). “A lateral boundary formulation for multi-level prediction models”. In: *Quarterly Journal of the Royal Meteorological Society* 102.432, pp. 405–418. DOI: `10.1002/qj.49710243210`.

Delestre, O. and P.-Y. Lagrée (2013). “A 'well-balanced' finite volume scheme for blood flow simulation”. In: *International Journal for Numerical Methods in Fluids* 72.2, pp. 177–205. DOI: `10.1002/fld.3736`.

Dümenil, L. and E. Todini (1992). “Chapter 9 - A rainfall-runoff scheme for use in the Hamburg climate model”. In: *Advances in Theoretical Hydrology.* Ed. by J. P. O'Kane. European Geophysical Society Series on Hydrological Sciences. Amsterdam: Elsevier, pp. 129–157. DOI: `10.1016/B978-0-444-89831-9.50016-8`.

Duran, D. R. (2010). *Numerical Methods in Fluid Dynamics.* 2d ed. Texts in Applied Mathematics. New York: Springer. DOI: `10.1007/978-1-4419-6412-0`.

Elsasser, H. and R. Bürki (2002). “Climate change as a threat to tourism in the Alps”. In: *Climate Research* 20.3, pp. 253–257. DOI: `10.3354/cr020253`.

Fortunato, A. B. and A. M. Baptista (1996). “Evaluation of horizontal gradients in sigma-coordinate shallow water models”. In: *Atmosphere–Ocean* 34.3, pp. 489–514. DOI: `10.1080/07055900.1996.9649574`.

Gal-Chen, T. and R. C. J. Somerville (1975a). “On the use of a coordinate transformation for the solution of the Navier-Stokes equations”. In: *Journal of Computational Physics* 17.2, pp. 209–228. DOI: `10.1016/0021-9991(75)90037-6`.

– (Mar. 1975b). “Numerical solution of the navier-stokes equations with topography”. In: *Journal of Computational Physics* 17.3, pp. 276–310. DOI: `10.1016/0021-9991(75)90054-6`.

Gallus, W. A. and J. B. Klemp (2000). “Behavior of Flow over Step Orography”. In: *Monthly Weather Review* 128.4, pp. 1153–1164. DOI: `10.1175/1520-0493(2000)128%3C1153:BOFOSO%3E2.0.CO;2`.

Gary, J. M. (1973). “Estimate of Truncation Error in Transformed Coordinate, Primitive Equation Atmospheric Models”. In: *Journal of the Atmospheric Sciences* 30.2, pp. 223–233. DOI: `10.1175/1520-0469(1973)030%3C0223:EOTEIT%3E2.0.CO;2`.

Ghosh, D. and E. M. Constantinescu (2015). “Well-Balanced, Conservative Finite Difference Algorithm for Atmospheric Flows”. In: *American Institute of Aeronautics and Astronautics Journal* 54.4, pp. 1370–1385. DOI: `10.2514/1.J054580`.

Giorgetta, M. A. and M. Wild (1995). *The water vapour continuum and its representation in ECHAM4.* Tech. rep. 162. Hamburg: Max Planck Institute for Meteorology. URL:

`https://pure.mpg.de/pubman/faces/ViewItemOverviewPage.jsp?itemId=item_2032326`.

Good, B. et al. (2014). “Performance of the cut-cell method of representing orography in idealized simulations”. In: *Atmospheric Science Letters* 15.1, pp. 44–49. DOI: `10.1002/asl2.465`.

Göttel, H. (2009). “Einfluss der nichthydrostatischen Modellierung und der Niederschlagsverdriftung auf die Ergebnisse regionaler Klimamodellierung”. PhD thesis. Universität Hamburg. DOI: `10.17617/2.994076`.

Greenberg, J. and A. Leroux (1996). “A Well-Balanced Scheme for the Numerical Processing of Source Terms in Hyperbolic Equations”. In: *SIAM Journal on Numerical Analysis* 33.1, pp. 1–16. DOI: `10.1137/0733001`.

Haltiner, G. J. and R. T. Williams (1980). *Numerical prediction and dynamic meteorology*. English. 2d ed. First ed. (1971) published under title: Numerical weather prediction. New York : Wiley. ISBN: 0471059714.

IPCC (2014). *Climate Change 2013: The Physical Science Basis. Contribution of Working Group I to the Fifth Assessment Report of the Intergovernmental Panel on Climate Change*. Ed. by T. F. Stocker et al. Cambridge, United Kingdom and New York, NY, USA: Cambridge University Press. DOI: `10.1017/CBO9781107415324`.

Jacob, D. (June 2001). “A note to the simulation of the annual and inter-annual variability of the water budget over the Baltic Sea drainage basin”. In: *Meteorology and Atmospheric Physics* 77.1–4, pp. 61–73. DOI: `10.1007/s007030170017`.

Jacob, D., J. Petersen, et al. (2014). “EURO-CORDEX: New high-resolution climate change projections for European impact research”. In: *Regional Environmental Change* 14.2, pp. 563–578. DOI: `10.1007/s10113-013-0499-2`.

Jacob, D., B. J. J. M. Van den Hurk, et al. (June 2001). “A comprehensive model inter-comparison study investigating the water budget during the BALTEX-PIDCAP period”. In: *Meteorology and Atmospheric Physics* 77.1–4, pp. 19–43. DOI: `10.1007/s007030170015`.

Janjić, Z. I., J. P. Gerrity, and S. Ničković (2001). “An Alternative Approach to Nonhydrostatic Modeling”. In: *Monthly Weather Review* 129.5, pp. 1164–1178. DOI: `10.1175/1520-0493(2001)129%3C1164:AAATNM%3E2.0.CO;2`.

Käppeli, R. and S. Mishra (Mar. 2016). “A well-balanced finite volume scheme for the Euler equations with gravitation. The exact preservation of hydrostatic equilibrium with arbitrary entropy stratification.” In: *Astronomy and Astrophysics* 587, A94. DOI: `10.1051/0004-6361/201527815`.

Kasahara, A. (July 1974). “Various Vertical Coordinate Systems Used for Numerical Weather Prediction”. In: *Monthly Weather Review* 102.7, pp. 509–522. DOI: `10.1175/1520-0493(1974)102%3C0509:VVCSUF%3E2.0.CO;2`.

Klein, R., K. R. Bates, and N. Nikiforakis (2009). “Well-balanced compressible cut-cell simulation of atmospheric flow”. In: *Philosophical Transactions of the Royal Society A: Mathematical, Physical and Engineering Sciences* 367.1907, pp. 4559–4575. DOI: `10.1098/rsta.2009.0174`.

Klemp, J. B. and R. B. Wilhelmson (June 1978). “The Simulation of Three-Dimensional Convective Storm Dynamics”. In: *Journal of the Atmospheric Sciences* 35.6, pp. 1070–1096. DOI: `10.1175/1520-0469(1978)035<1070:TSOTDC>2.0.CO;2`.

Kurihara, Y. (1968). “Note on Finite Difference Expressions for the Hydrostatic Relation and Pressure Gradient Force”. In: *Monthly Weather Review* 96.9, pp. 654–656. DOI: `10.1175/1520-0493(1968)096%3C0654:nofdef%3E2.0.co;2`.

Laprise, R. (Jan. 1992). “The Euler Equations of Motion with Hydrostatic Pressure as an Independent Variable”. In: *Monthly Weather Review* 120.1, pp. 197–207. DOI: `10.1175/1520-0493(1992)120%3C0197:TEEOMW%3E2.0.CO;2`.

LeVeque, R. J. (1998). “Balancing Source Terms and Flux Gradients in High-Resolution Godunov Methods: The Quasi-Steady Wave-Propagation Algorithm”. In: *Journal of Computational Physics* 146.1, pp. 346–365. DOI: `10.1006/jcph.1998.6058`.

Lin, S.-J. (1997). “A finite-volume integration method for computing pressure gradient force in general vertical coordinates”. In: *Quarterly Journal of the Royal Meteorological Society* 123.542, pp. 1749–1762. DOI: `10.1002/qj.49712354214`.

Louis, J.-F. (Sept. 1979). “A parametric model of vertical eddy fluxes in the atmosphere”. In: *Boundary-Layer Meteorology* 17.2, pp. 187–202. DOI: `10.1007/BF00117978`.

Majewski, D. (1991). “The EUROPA-modell of the Deutscher Wetterdienst”. In: *Seminar on Numerical Methods in Atmospheric Models, 9-13 September 1991.* Vol. II. ECMWF. Shinfield Park, Reading: ECMWF, pp. 147–193. URL: `https://www.ecmwf.int/en/elibrary/10940-europa-modell-deutscher-wetterdienst`.

Majewski, D. and R. Schrodin (1995). *Documentation of the EM/DM-System.* Tech. rep. Offenbach: Deutscher Wetterdienst.

McCalpin, J. D. (1994). “A comparison of second-order and fourth-order pressure gradient algorithms in a σ-coordinate ocean model”. In: *International Journal for Numerical Methods in Fluids* 18.4, pp. 361–383. DOI: `10.1002/fld.1650180404`.

Mesinger, F. et al. (1988). “The Step-Mountain Coordinate: Model Description and Performance for Cases of Alpine Lee Cyclogenesis and for a Case of an Appalachian Redevelopment”. In: *Monthly Weather Review* 116.7, pp. 1493–1518. DOI: `10.1175/1520-0493(1988)116%3C1493:TSMCMD%3E2.0.CO;2`.

Morcrette, J.-J., L. Smith, and Y. Fouquart (Nov. 1986). “Pressure and temperature dependence of the absorption in long wave radiation parametrization”. In: *Beiträge zur Physik der Atmosphäre* 59, pp. 455–469.

Müller, L. O., C. Parés, and E. F. Toro (2013). “Well-balanced high-order numerical schemes for one-dimensional blood flow in vessels with varying mechanical properties”. In: *Journal of Computational Physics* 242, pp. 53–85. DOI: `10.1016/j.jcp.2013.01.050`.

NASA (1976). *U.S. Standard Atmosphere, 1976*. Tech. rep. Washington, DC: National Aeronautics and Space Administration. URL: `https://ntrs.nasa.gov/search.jsp?R=19770009539`.

Noelle, S. et al. (2006). “Well-balanced finite volume schemes of arbitrary order of accuracy for shallow water flows”. In: *Journal of Computational Physics* 213.2, pp. 474–499. DOI: `10.1016/j.jcp.2005.08.019`.

Nordeng, T-E. (Sept. 1994). “Extended versions of the convective parametrization scheme at ECMWF and their impact on the mean and transient activity of the model in the tropics”. In: *ECMWF Technical Memorandum* 206, p. 41. URL: `https://www.ecmwf.int/en/elibrary/11393-extended-versions-convective-parametrization-scheme-ecmwf-and-their-impact-mean`.

Orlanski, I. (1981). “The Quasi-Hydrostatic Approximation”. In: *Journal of the Atmospheric Sciences* 38.3, pp. 572–582. DOI: `10.1175/1520-0469(1981)038%3C0572:tqha%3E2.0.co;2`.

Phillips, N. A. (Apr. 1957). “A COORDINATE SYSTEM HAVING SOME SPECIAL ADVANTAGES FOR NUMERICAL FORECASTING”. In: *Journal of Meteorology* 14.2, pp. 184–185. DOI: `10.1175/1520-0469(1957)014%3C0184:ACSHSS%3E2.0.CO;2`.

Qian, H. et al. (2015). “Well-balanced numerical modelling of non-uniform sediment transport in alluvial rivers”. In: *International Journal of Sediment Research* 30.2, pp. 117–130. DOI: `10.1016/j.ijsrc.2015.03.002`.

Roeckner, E. et al. (1996). *The atmospheric general circulation model ECHAM-4: Model description and simulation of present day climate*. Tech. rep. 218. Hamburg: Max Planck Institute for Meteorology. URL: `https://pure.mpg.de/pubman/faces/ViewItemOverviewPage.jsp?itemId=item_1781494_8`.

Sangster, W. E. (1960). “A METHOD OF REPRESENTING THE HORIZONTAL PRESSURE FORCE WITHOUT REDUCTION OF STATION PRESSURES TO SEA LEVEL”. In: *Journal of Meteorology* 17.2, pp. 166–176. DOI: `10.1175/1520-0469(1960)017%3C0166:amorth%3E2.0.co;2`.

Schär, C. et al. (2002). “A New Terrain-Following Vertical Coordinate Formulation for Atmospheric Prediction Models”. In: *Monthly Weather Review* 130.10, pp. 2459–2480. DOI: `10.1175/1520-0493(2002)130%3C2459:ANTFVC%3E2.0.CO;2`.

Semmler, T. (2002). “Der Wasser- und Energiehaushalt der arktischen Atmosphäre”. PhD thesis. Universität Hamburg. URL: `https://pure.mpg.de/pubman/faces/ViewItemOverviewPage.jsp?itemId=item_995430`.

Shaw, J. and H. Weller (2016). “Comparison of Terrain-Following and Cut-Cell Grids Using a Nonhydrostatic Model”. In: *Monthly Weather Review* 144.6, pp. 2085–2099. DOI: `10.1175/MWR-D-15-0226.1`.

Simmons, A. J. and D. M. Burridge (Apr. 1981). “An Energy and Angular-Momentum Conserving Vertical Finite-Difference Scheme and Hybrid Vertical Coordinates”. In: *Monthly Weather Review* 109.4, pp. 758–766. DOI: `10.1175/1520-0493(1981)109%3C0758:AEAAMC%3E2.0.CO;2`.

Smagorinsky, J. et al. (1967). “Prediction Experiments With a General Circulation Model”. In: *Proceedings of the International Symposium on Dynamics of Large Scale Atmospheric Processes.* Moscow, USSR.

Song, Y. T. (1998). “A General Pressure Gradient Formulation for Ocean Models. Part I: Scheme Design and Diagnostic Analysis”. In: *Monthly Weather Review* 126.12, pp. 3213–3230. DOI: `10.1175/1520-0493(1998)126%3C3213:AGPGFF%3E2.0.CO;2`.

Song, Y. T. and D. G. Wright (1998). “A General Pressure Gradient Formulation for Ocean Models. Part II: Energy, Momentum, and Bottom Torque Consistency”. In: *Monthly Weather Review* 126.12, pp. 3231–3247. DOI: `10.1175/1520-0493(1998)126%3C3231:AGPGFF%3E2.0.CO;2`.

Steppeler, J., H.-W. Bitzer, Z. I. Janjić, et al. (2006). “Prediction of Clouds and Rain Using a z–Coordinate Nonhydrostatic Model”. In: *Monthly Weather Review* 134.12, pp. 3625–3643. DOI: `10.1175/MWR3331.1`.

Steppeler, J., H.-W. Bitzer, M. Minotte, et al. (2002). “Nonhydrostatic Atmospheric Modeling using a z–Coordinate Representation”. In: *Monthly Weather Review* 130.8, pp. 2143–2149. DOI: `10.1175/1520-0493(2002)130%3C2143:NAMUAZ%3E2.0.CO;2`.

Sundqvist, H. (1975). “On Truncation Errors in Sigma–System Models”. In: *Atmosphere* 13.3, pp. 81–95. DOI: `10.1080/00046973.1975.9648390`.

– (Mar. 1976). “On vertical interpolation and truncation in connexion with use of sigma system models”. In: *Atmosphere* 14.1, pp. 37–52. DOI: `10.1080/00046973.1976.9648400`.

– (1978). “A parameterization scheme for non-convective condensation including prediction of cloud water content”. In: *Quarterly Journal of the Royal Meteorological Society* 104.441, pp. 677–690. DOI: `10.1002/qj.49710444110`.

Taylor, K. E., R. J. Stouffer, and G. A. Meehl (2012). “An Overview of CMIP5 and the Experimental Design”. In: *Bulletin of the American Meteorological Society* 93.4, pp. 485–498. DOI: `10.1175/BAMS-D-11-00094.1`.

Tiedtke, M. (1989). “A Comprehensive Mass Flux Scheme for Cumulus Parameterization in Large–Scale Models”. In: *Monthly Weather Review* 117.8, pp. 1779–1800. DOI: `10.1175/1520-0493(1989)117%3C1779:ACMFSF%3E2.0.CO;2`.

Vater, S., N. Beisiegel, and J. Behrens (2015). “A limiter–based well-balanced discontinuous Galerkin method for shallow–water flows with wetting and drying: One–dimensional case”. In: *Advances in Water Resources* 85, pp. 1–13. DOI: `10.1016/j.advwatres.2015.08.008`.

Wang, W. et al. (2009). “High-order well-balanced schemes and applications to non-equilibrium flow”. In: *Journal of Computational Physics* 228.18, pp. 6682–6702. DOI: `10.1016/j.jcp.2009.05.028`.

White, A. A. et al. (2005). “Consistent approximate models of the global atmosphere: shallow, deep, hydrostatic, quasi-hydrostatic and non-hydrostatic”. In: *Quarterly Journal of the Royal Meteorological Society* 131.609, pp. 2081–2107. DOI: `10.1256/qj.04.49`.

Xing, Y. and C. W. Shu (2006). “High–order Well–balanced finite difference WENO schemes for a class of hyperbolic systems with source terms”. In: *Journal of Scientific Computing* 27.1-3, pp. 477–494. DOI: `10.1007/s10915-005-9027-y`.

Yamazaki, H., T. Satomura, and N. Nikiforakis (2016). “Three–dimensional cut–cell modelling for high–resolution atmospheric simulations”. In: *Quarterly Journal of the Royal Meteorological Society* 142.696, pp. 1335–1350. DOI: `10.1002/qj.2736`.

You, Q.-L. et al. (2017). “An overview of studies of observed climate change in the Hindu Kush Himalayan (HKH) region”. In: *Advances in Climate Change Research* 8.3, pp. 141–147. DOI: `10.1016/j.accre.2017.04.001`.

Zhu, Z. et al. (1992). “A Vertical Finite-Difference Scheme Based on a Hybrid σ-θ-p Coordinate”. In: *Monthly Weather Review* 120.5, pp. 851–862. DOI: `10.1175/1520-0493(1992)120%3C0851:AVFDSB%3E2.0.CO;2`.

Acknowledgement

I would like to express my deepest gratitude towards my supervisor Prof. Jörn Behrens for the continued support throughout my time as a PhD candidate. I am especially thankful for providing a topic that was both fruitful and aligned with my personal interests in a way that exceeded my expectations. His door was always open to me be it for the discussion of scientific or personal matters. Moreover, he unreservedly welcomed me into his working group which led to crucial scientific and personal interactions supporting my work even further. Without his enormous patience, constructive guidance and uplifting attitude the present work would not have been possible.

I would also like to express my deepest gratitude towards my second supervisor Prof. Daniela Jacob. She introduced me to the scientific world and sparked my interest in geophysical problems when I worked as her student assistant setting me up for the path that led me to this point. She gave me the utmost freedom in pursuing my research interests making my scientific and personal growth during the PhD work the priority. I am especially grateful for providing a great working environment at GERICS and for unconditionally supporting me throughout the unforeseen complications and delays of my work.

I would also like to especially thank Dr. Stefan Vater who supported my work through uncounted hours of in-depth discussion of the mathematical developments and their implementation. Not once did I leave his office without new ideas to pursue and new motivation to invest into my work.

I am very grateful to my fellow (former) PhD candidate Dr. Bastian Eggert for providing a fun and inspiring office atmosphere as well as for always having an open ear. I would also like to thank Dr. Kevin Sieck for his proofreading and helpful encouragement and the whole GERICS team for providing an environment both fun and productive. Moreover, I would like to extend my gratitude to the NUMGEO working group at University of Hamburg for being able to toss around ideas, receive constructive criticism and for just having good times.

I also thank those who I could not mention by name for reasons of brevity but who supported and encouraged me over the years. Finally, I thank my parents and especially my mother Christina for supporting me through all the hold-ups and difficult times. I also thank my sister Jana for proofreading and encouragement.

Eidesstattliche Erklärung

Hiermit versichere ich an Eides statt, dass ich die vorliegende Dissertation mit dem Titel: „Towards well-balancing the regional hydrostatic climate model REMO“ selbstständig verfasst und keine anderen als die angegebenen Hilfsmittel – insbesondere keine im Quellenverzeichnis nicht benannten Internet-Quellen – benutzt habe. Alle Stellen, die wörtlich oder sinngemäß aus Veröffentlichungen entnommen wurden, sind als solche kenntlich gemacht. Ich versichere weiterhin, dass ich die Dissertation oder Teile davon vorher weder im In- noch im Ausland in einem anderen Prüfungsverfahren eingereicht habe und die eingereichte schriftliche Fassung der auf dem elektronischen Speichermedium entspricht.

Ort und Datum

Unterschrift